MICRO PLASMA ARC WELDING OF SIMILAR AND DISSIMILAR MATERIALS AND FORMABILITY STUDY OF WELDED JOINT

Vivekananda Haldar

Department of Mechanical Engineering

Indian Institute of Technology Guwahati

January 2025

MICRO PLASMA ARC WELDING OF SIMILAR AND DISSIMILAR MATERIALS AND FORMABILITY STUDY OF WELDED JOINT

Thesis submitted to

Indian Institute of Technology Guwahati

For the award of the degree of

Doctor of Philosophy

By

VIVEKANANDA HALDAR

(Reg. No. 176103115)

Under the supervision

of

Prof. Sukhomay Pal

Department of Mechanical Engineering

Indian Institute of Technology Guwahati

January 2025

Department of Mechanical Engineering
Indian Institute of Technology Guwahati
Guwahati-781039
INDIA

CERTIFICATE

It is certified that the work contained in the thesis entitled "**MICRO PLASMA ARC WELDING OF SIMILAR AND DISSIMILAR MATERIALS AND FORMABILITY STUDY OF WELDED JOINT**" submitted by **Mr. Vivekananda Haldar** (Reg. No. 176103115) to the Indian Institute of Technology Guwahati for the award of degree of Doctor of Philosophy has been carried out under my supervision in the Department of Mechanical Engineering, Indian Institute of Technology Guwahati. This work has not been submitted elsewhere for the award of any degree or diploma.

The thesis, in my opinion, has reached the standard fulfilling the requirements for the award of degree of Doctor of Philosophy in accordance with the regulations of the institute.

Dr. Sukhomay Pal
Professor
Department of Mechanical Engineering
Indian Institute of Technology Guwahati
Guwahati-781039
Assam, INDIA

THESIS APPROVAL SHEET

The thesis titled

Micro Plasma Arc Welding of Similar and Dissimilar Materials and Formability Study of Welded Joint

by

Vivekananda Haldar

is approved for the **Doctor of Philosophy.**

Examiners

____

____

Supervisor

____

Chairman

____

Date: 2nd January 2025

Place: IIT Guwahati, Guwahati

DECLARATION

I declare that,

a. The work contained in this thesis is original and has been done by me under the guidance of my supervisor.
b. The work has not been submitted to any other institute for any degree or diploma.
c. I have followed the guidelines provided by the institute in preparing the thesis.
d. I have confirmed to the norms and guidelines given in the Ethical code of Conduct of the Institute.
e. Whenever I have used materials (data, theoretical analysis, figures and text) from other sources I have given due credit to them by citing them in the text of the thesis and giving their details in the references. Further, I have taken permission from the copyright owners of the sources, whenever necessary.

Date:

VIVEKANANDA HALDAR

(176103115)

Department of Mechanical Engineering

Indian Institute of Technology Guwahati

Guwahati – 781039

Assam, India

Acknowledgement

I commence by extending my gratitude to the Almighty for preserving my health and granting me the patience essential for the duration of my thesis work. I would like to convey my profound appreciation to everyone who, in diverse capacities, has assisted me both directly and indirectly during my doctoral journey at IIT Guwahati. At every juncture of my PhD, numerous individuals provided invaluable support, with each playing a pivotal role. I am indebted to each and every one of them.

I express my sincere gratitude and appreciation to my supervisor, **Dr. Sukhomay Pal, Professor, Department of Mechanical Engineering, IIT Guwahati**, for his valuable advices, expert guidance, patience and encouragement, and for all support he has given me from the day one to throughout the PhD work. Without his support, advice, and motivation, it would have been an impossible task for me to carry over this research work. Regardless of his workload, he always found time to discuss with me for the PhD work and many suggestions for betterment of my personal life. I really fill privileged for having the opportunity to work under him and as my PhD supervisor.

I sincerely appreciate **Prof. Shyamanta M. Hazarika**, **Prof. K. S. R. Krishna Murthy, Prof. S. Sentthilvelan** and **Prof. Santosha K. Dwivedy,** the present and former Head of the department, for extending all necessary facilities of the department. I would like to thank my doctoral committee chairman **Prof. R. Ganesh Narayanan,** Professor, Department of Mechanical Engineering for his valuable suggestion and encouragement during the PhD work. Also, I would like to extend my appreciation to my doctoral committee members **Dr. Pankaj Biswas,** Professor, Department of Mechanical Engineering, and **Dr. S. K. Majumder,** Professor, Department of Chemical Engineering for their constructive criticisms and helpful suggestions which make research work improvement. I want to give specially thank to **Dr. Swarup Bag**, Professor, Department of Mechanical Engineering, for providing the experimental facility. Thanks to all the faculty members of the department for not only their technical suggestions at times but also their friendly interactions that create an enjoyable working environment in the department.

I wish to express my sincere thanks to Mr. S. Ahmed, Mr. J. Basumatary, Mr. P. Paul and Mr. S. Sharma for their assistant whenever needed during experimentation. Also, thanks to CIF HOC, Dr. A Malakar, staff and TA of SEM, TEM and FESEM for their helping hand for the analysis of the specimen. I am very much thankful to superintendent of Central Workshop, **Mr. N. K. Das** and amazing helping staffs *Mr. C. Banikya, Mr. Dilip Chetri, Mr. Gakul Das, Mr. D. Khaklary, Mr. M. Sharma, Mr. M. Medhi, Mr. M. Baishya, Mr. N. Saikia, Mr. J. Saikia, Mr. U. Gohain, Mr. G. Das, Mr. Dulumoni Das, and Mr. S. Gogoi* for their helping hand for the experimentation. Sincere thanks to my seniors and friends Dr. Uttam Kumar Tarai, Dr. Ajit Kumar Sahu, Dr. Bikash Kumar, Dr. Debtanay Das, Dr. Viwek Kumar, Dr. Monjusha Sharma, Dr. Subhra Paul, Mr. Akshay Namdeo, Mr. Ankan Mishra, Mr. Sunil Kumar Biswal, Mr. Dipankar Saha, Mr. Akshay kumar Soni, Mr. Swagat Dwibedi, Mr. Hritaban Acharya, Mr. Amritesh Kumar, Mr. Gaurav Prakash, Mr. Alok Trivedi, Mr. Anil Sah, Mr. Sukanta Das, Mr. Priyobrata Nath, Mr. Utla Chandra Sekhar and Mr. Avadh Kishore Prasad for their help, support and advice in different occasions of my PhD work.

I shall always be grateful to my parents and my friend **Dr. Bidesh Sengupta,** Mr. Mrinmoy Roy, Mr. Biswajit Saha for their great encouragement, guidance, love, affection, motivation and warm blessings. The blessing got from my parents and my siblings, Bidyasagar, Bikramadity, and Sarada.

I will always grateful to my teachers who have shown me a path to move on in my life. Especially, I would like to thank my teacher Dr. G. Ganguly for continuous guidance and mental support in my life for that I am here from the grass root level.

I may have missed out a few names in the above list; my sincere apologies are due for any such inadvertent oversight.

Vivekananda Haldar

This Thesis Dedicated

To

My loving parents

My brothers and sister

Abstract

This work is focused on the similar and dissimilar joining of austenitic 316L stainless steel (ASS 316L) and Inconel 625 (IN 625) by using micro plasma arc welding (MPAW). The various aspects of joint metallurgy are evaluated and their effect on the formability of the welded blanks are investigated. The welding experiments are performed with different combination of process parameters to determine best parameter setting for superior strength and formability. A post weld solution heat treatment is proposed to improve the formability of Inconel 625 welded blanks. Dissimilar MPAW of 316L stainless steel and Inconel 625 are also conducted to study the metallurgical characterization of fusion zone and its effect on the overall strength, and formability of the welded blanks with cause and location of failure.

316L stainless steel is highly demanded in various industries due to good mechanical strength, weldability, formability and high corrosion resistance properties. Hence, the formability of thin austenitic 316L stainless steel welded blanks is studied in this thesis. In this context, a small-scale stretch forming setup is designed and fabricated with a 30 mm punch diameter. Three different types of welded blank are prepared by using different welding process parameters settings namely, welding current, welding speed, stand-off distance and nozzle diameter. The welded joint microstructure of various zones is evaluated using metallographic procedure. X-ray diffraction and transmission electron microscopy are used to determine phases present in the base material and fusion zone. Tensile, microhardness and stretch forming tests are carried out to determine the mechanical properties of the welded joints. The forming limit diagram and strain distribution are calculated experimentally from the stretch forming tests. The fusion zone is found with skeletal and columnar δ-ferrite. Few secondary phases are also observed at the transition zone through TEM analysis. The presence of the welded zones reduces the formability as compared with the base material. However, good joint formability is achieved by using MPAW. A uniform strain distribution is found on both sides of the pole in biaxial and uniaxial strain path specimens.

The Inconel 625 is a solid solution strengthened alloy of nickel, which is mainly used in gas turbines, aircraft engines, marine industries and chemical power plants due to its superior properties. This thesis work also aims to comprehensively understand the mechanical properties and deformation response of Inconel 625 micro plasma arc welded

blanks (MPAWB), with specific attention to their formability. The welded blanks are solution treated for potential alterations in their forming behavior. The joint metallurgy is assessed through advanced techniques such as FESEM, TEM, XRD. The analysis reveals that the fusion zone of the MPAWB predominantly comprises of nickel γ-matrix along with diverse dendritic structures, alongside some secondary phases like Laves phase, NbC, and TiC. Following the solution treatment of the welded blanks, the dendritic structures undergo melting and subsequent recrystallization, resulting in a more uniform microstructure. The dissolution of secondary phases in the solution treated welded blank (STWB) leads to a reduction in dislocation density compared to the MPAWB. Furthermore, the hardness of the STWB decreases from 268.9 ± 9 HV to 252.16 ± 6.75 HV, and a notable increase in elongation by 12.39 %, compared to the MPAWB. The forming limit diagrams of as-received Inconel 625, MPAWB and STWB exhibit similar strain and thickness distributions along the uniaxial-to-biaxial strain path. Notably, symmetric strain and thickness distribution are detected on both sides of the pole for all the cases.

The dissimilar joint of Inconel 625 and 316L stainless steel is mainly used for the fabrication of sub-scale boilers and oil-refinery converters where, the temperature can reach more than thousand and the ambient is highly contaminated with oxygen and carbon dioxide. Thus, this study focuses the effect of joint metallurgy on the mechanical properties and formability of dissimilar 316L stainless steel and Inconel 625 weldments. The welded blanks are stretched from uniaxial to biaxial by tensile test and limiting dome height test (LDH) in order to measure the joint efficiency and formability, respectively. The metallurgical investigation indicates that the fusion zone consists of a homogeneous mixture of Nickel (γ_{Ni}) and iron-based austenite (γ_{Fe}) with different types of dendritic structure interconnected with brittle Laves phase network and some secondary phases like MC, M_6C, and NbC. Due to the presence of such phases, the weld hardness is increased and affected the formability of the welded blanks. The measured maximum elongation of the welded blank is 30.50%, which is 100.4% of Inconel 625 and 52.58% of 316L stainless steel. Moreover, the achieved joint strength of the welded blank is 643.7 MPa, which is 67% of Inconel 625 and 94% of 316L stainless steel base materials. The maximum LDHs of the welded blank, 316L stainless steel and Inconel 625 are 6.7 mm, 12.3 mm and 9.7 mm, respectively, in dry condition. During the tensile and LDH tests the failure of the welded blank is taken place from the week partially melted zone. The thickness distribution profile of the welded blank reports that the thickness reduction of 316L stainless steel side is higher than the Inconel 625 side.

Keywords: Micro plasma arc welding, Limiting dome height test, FLD, Inconel 625, stainless steel, AISI 316L, Formability, TEM, FESEM, Laves phase.

Contents

ASS 316L	Austenitic stainless steel 316L
A-TIG	Activated flux tungsten inert gas welding
BZ	Base zone
BM	Base material
BB	Bottom bead
EDX	Energy dispersive X-ray
EDS	Energy dispersive spectroscopy
EBW	Electron beam welding
FCAW	Flux-cored arc welding
FZ	Fusion zone
FLD	Forming limit diagram
FLC	Forming limit curve
FGM	Functionally graded material
GMAW	Gas metal arc welding
GTAW	Gas tungsten arc welding
HAZ	Heat affected zone
HT	Heat treatment
HSLA	High strength low alloy
IN 625	Inconel 625
LBW	Laser beam welding
LDH	Limiting dome height test
LD	Load-displacement
MIG	Metal inert gas
MGB	Migrated grain boundary
MPAW	Micro plasma arc welding
MPAWB	Micro plasma arc welded blank
MMAW	Manual metal arc welding
PAW	Plasma arc welding
PAWB	Plasma arc welded blank
RD	Rolling direction
ST	Solution treatment
SOD	Stand-off distance

STWB	Solution treated welded blank
SGB	Sub grain boundary
SSGB	Solidification sub grain boundary
SAED	Selected area diffraction
TIG	Tungsten inert gas welding
TTT	Time-temperature-transformation
TLP	Transient liquid phase bonding
TWB	Tailored welded blank
TEM	Transmitted electron microscopy
TZ	Transition zone
TB	Top bead
UTM	Universal testing machine
WB	Welded blank
XRD	X-ray diffraction

Nomenclature

K	Strain hardening coefficient
n	Strain hardening index
R	Anisotropy
γ'	Ni_3(Ti, Nb, Al)
γ''	Ni_3Nb
γ	Austenite
δ/α	Ferrite
d	Arithmetic mean of the two diagonals
β	Strain ratio
ε_1	Major strain
ε_2	Minor strain
ε_t	True strain
d_o	Initial grid diameter
d_f	Final grid diameter
σ_t	True stress
ε_{ls}	Major limiting strain
ε_r	Strain ratio
2θ	Bragg's diffraction angle
δ	Dislocation density
ε	Lattice strain
λ	Wavelength
D	The size of micro crystalline
G	Temperature gradient
R	Solidification rate
γ_{Ni}	Nickel austenite matrix
γ_{Fe}	Iron austenite matrix
δ_{Fe}	δ-ferrite

List of figures

List of tables

Chapter 1
Introduction

1.1 General backgrounds

Welding is one of the most efficient joining technique to fabricate complex components. Some welding processes can be accomplished by the application of heat only like conventional fusion welding processes. Certain welding processes use both heat and pressure for joining of metallic plates like diffusion welding. However, among all welding processes, arc welding is the most versatile and widely used welding technique that joins materials through the application of heat generated by an electric arc. This method involves creating an electrical circuit between the workpiece and an electrode, forming an arc that produces intense heat, which is more than the melting temperature of the material. The heat generated melts the material and, if used, a consumable filler material, allowing them to fuse and form a strong joint after welding. Different types of arc welding techniques are available which encompasses various methods such as gas metal arc welding (GMAW), submerged arc welding (SAW), manual metal arc welding (MMAW), tungsten inert gas welding (TIG), flux-cored arc welding (FCAW), and plasma arc welding (PAW). Each method has its specific applications, advantages, and limitations. These welding techniques have extensive use in industries like construction, manufacturing, automotive, aerospace etc. During arc welding, due to concentrated high heat input, localized melting and solidification take place at the weld interface. This leads to development of three distinct zones in the welding area namely, fusion zone (FZ), heat affected zone (HAZ) and the non-affected base zone (BZ). Generally, mechanical failure is taken place from the HAZ due to the variation of microstructure like grain growth. The arc power density refers to the amount of heat input per unit area is an important factor in welding. When the power density is high and when the others parameters like travel speed, material thickness, and the dimensional nature of heat transfer are fixed, it leads to constricted arc, resulting in a smaller HAZ. A reduced HAZ is often considered a highly desirable characteristic in welding process. Thus, for any welding process heat input is an important criterion. Figure 1.1 describes the relationship between the heat input and power density of different types of welding.

Micro welding is used to fabricate delicate products such as surgical instrument, microelectronics parts, while it can also be used to joint thin mechanical components such as small size mechanical bellows, load cells, mechanical seals, etc. Among all the welding processes laser beam welding (LBW), electron beam welding (EBW) and micro plasma arc welding (MPAW) are widely acceptable for their superior welding quality for such applications. MPAW has greater arc stability and power density, which can augment in the production of deeper and narrower penetration with minimal residual stresses and distortion of the weld joints. MPAW is an advancement of the TIG process with current ranging from 0.1 to 15 A, which is suitable for thin sheet of titanium alloy, stainless steel, copper-nickel superalloys etc. Figure 1.2 describes different applications of MPAW process.

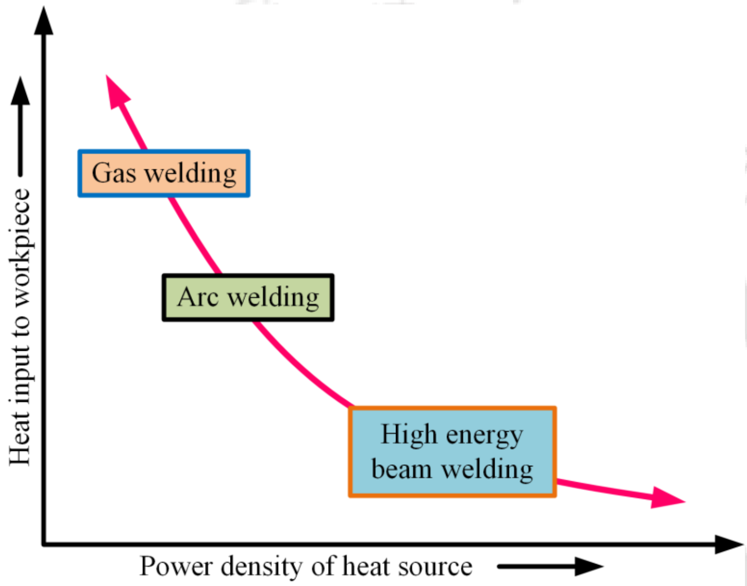

Fig. 1.1 Relationship between heat input to power density of various welding processes (Kou, 2003)

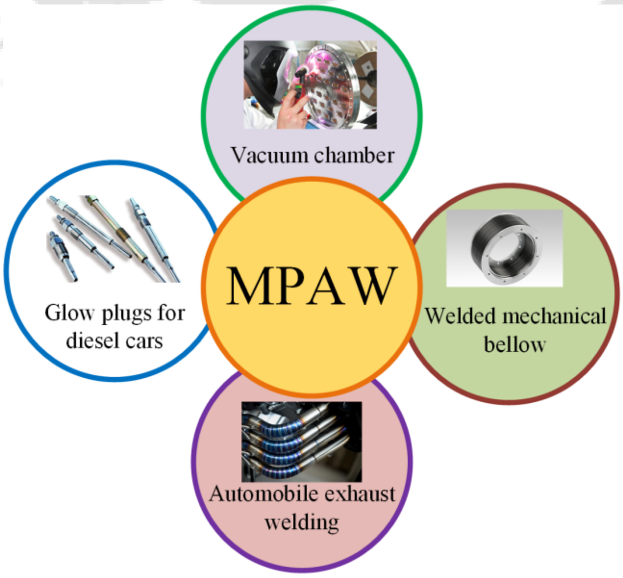

Fig. 1.2 Applications of micro plasma arc welding

The similar and dissimilar joining of austenitic stainless steel 316L and Inconel 625 sheets have huge demand in different industries due to their superior mechanical properties, corrosion resistivity form room temperature to elevated temperature. However, joining these thin sheets is very difficult due to the formation of welding defects like distortion, porosity, burn through, etc. MPAW is a good choice for the joining of such thin sheets due to its precise controllable heat input and low setup cost. However, after welding loss of ductility is an important concern for those fields where deformable similar and dissimilar joint of 316L stainless steel and Inconel 625 are used.

The formability of sheet metal can be defined as the ability of a sheet metal to undergo plastic deformation in a given shape without defects. The forming process gains attention due to the large-scale production and with attractive quality of final product. Deformable similar and dissimilar welded blanks of thin sheets are extensively used in automobile, aviation, spacecraft and petrochemical industries. The formability of welded blanks can be achieved by different types of formability tests like deep drawing, Erichsen cupping test stretch forming, etc. Among the all formability tests, limiting dome height (LDH) test is most popular technique. In LDH test, dome height, surface strain and thickness variation are measured to predict formability. Mechanical properties like strain hardening index (*n*-value), strain hardening coefficient (*K*-value), strain rate sensitivity and anisotropy (*R*-value) of the blanks are the main influencing parameters for the formability of the material. The values of these quality parameters are measured by doing uniaxial tensile test. In conventional stretch forming test, the formability of the blanks can be achieved by measuring the LDH, plotting forming limit diagram (FLD), strain distribution profile and the thickness distribution profile.

1.2 Motivation

Thin sheets are used as a substitute for thick materials to enhance fuel efficiency, reduce the detrimental emissions from the vehicle exhaust and cost. Hence, thin sheet materials gained huge significance in the manufacturing industry. The welding of thin sheet is one of the important research areas in these industries. The LBW and EBW are mainly used for joining thin sheets. These welding techniques offer less weld distortion with high energy efficiency. However, the higher operating cost of these welding methods is a major obstacle for the manufacturing industry. Alternatively, MPAW can be used as a substitute for minimizing the overall production costs. Moreover, MPAW can able to joint ultra-thin sheet up to 0.1 mm without leaving any defect due to high concentrated power density and stable arc at a lower current of up to 0.1 A. Thus, MPAW is chosen in the present thesis.

The 316L stainless steel represent a group of stainless steel, which has higher tonnages than any other group of steels (Lippold & Kotecki, 2005). The service temperature of this austenitic stainless steel is from cryogenic to 760 ºC. They are strengthened by cold working process. The present work is motivated to investigate the weldability of austenitic 316L stainless steel due to its rigorous interest in various welding applications. The principal composition of conventional austenitic stainless steel are 18% chromium and 8% nickel, but it also contains some other alloying elements like molybdenum, titanium, copper, and nitrogen. As they have excellent corrosion resistance, better creep rupture strength at elevated temperature, and high toughness at low temperatures, austenitic stainless steels are mostly used in structural material, petrochemical, and power engineering and, sometimes in automobile and aircraft industries. However, welding of thin 316L stainless steel sheets is a difficult task due to complication by different types of welding defects, loss of ductility due to formation of secondary phases. Hence, this research work is motivated to exploring the parameters range for good strength and formability of the welded blanks (WBs).

Similarly, Inconel 625 is a solid solution strengthened super alloy, has excellent corrosion resistivity and strength from room temperature to elevated temperature. In this alloy, Cr and Mo are act as the main solid solution strengthening elements, which are generally dissolve into the Ni-austenitic (γ) matrix and provide solid solution strength and resistance against the oxidation and corrosion from the attack of various corrosive environments. Nb, Ti and Al are the precipitate-strengthened elements that combined with Ni and produced distributed γ' [Ni_3(Ti, Nb, Al)] and γ'' (Ni_3Nb) precipitates and increased strength of the Inconel 625. Some carbides like Nb or Ti-based blocky MC carbide, Si, Ni, and Cr-based M_6C carbide and only Cr-based carbide $M_{23}C_6$ are also responsible for their excellent mechanical strength. Because of such good properties, it has enormous applications in petrochemical, power generation and aerospace. However, the main challenging tasks encounter in welding of Inconel 625 are thermal cracking, loss of ductility due to the formation of brittle Laves phase and carbide precipitation. Thus, the current study is inspired to determine the microstructural changes after welding and tried to improve the formability by doing solution treatment.

The dissimilar joint of austenitic stainless steel and nickel-based super alloy has extensive applications in the field of nuclear industry, sub-size boilers, liquid rocket components in association with gas turbines, and cryogenic engines. The dissimilar joining of sheets is an important aspect. With the comparison of Inconel 625, 316L stainless steel is less expensive with almost similar material properties. Thus, by doing dissimilar joining of these two materials not only meets the operational requirements but also leads to significant cost savings in different industries by reducing the overall materials cost. However, welding of two dissimilar materials with different thermal properties like thermal conductivity and melting temperatures is a difficult task. Moreover, dissimilar materials may form some intermetallic compounds and secondary phases which have detrimental effect on weld quality in the form of weld metallurgy and mechanical properties.

Therefore, the present research is motivated to dissimilar welding of Inconel 625 and 316L stainless steel by studying the effect joint metallurgy on the mechanical behavior of the welded blanks.

1.3 Research objectives

Considering the gaps identified in prior research, the current study aims to achieve the following objectives:

- Weldability and formability study of micro plasma arc welded austenitic 316L stainless steel thin sheet joint.
- Improve the mechanical properties of plasma arc welded Inconel 625 blanks using solution heat treatment.
- Study the influence of fusion zone metallurgy on the mechanical behavior of dissimilar Inconel 625 and 316L stainless steel joint.

1.4 Contribution of the thesis

- In this work a detailed experimental investigation is carried out to measure the formability of 316L stainless steel micro plasma arc welded blank by using laboratory developed small scale LDH test setup. The metallurgical analysis is carried out thoroughly to evaluate their effect on the mechanical properties of MPAWB.
- This is the first attempt on the study of formability improvement for micro plasma arc welded Inconel 625 welded blanks by solution treatment.
- This is the first investigation focusing on the study of formability of Inconel 625 and 316L stainless steel dissimilar welded blank joint by MPAW.

1.5 Outline of the thesis

The thesis work focusses on the study of similar and dissimilar welding joint of Inconel 625 and 316L stainless steel thin sheets. The effect of weld metallurgy on mechanical properties like ultimate tensile strength, formability and the cause of failure are evaluated thoroughly. This thesis also represents the formability improvement of Inconel 625 by solution treatment after welding. The thesis is splitted into total seven chapters as follows:

Chapter 1: represents the general background and motivation of the thesis. It also contains short description about 316L stainless steel, Inconel 625 and requirement of formability study.

Chapter 2: provides literature studies on similar and dissimilar joining of 316L stainless steel and Inconel 625 by MPAW. It also describes the effect weld metallurgy on the formability of welded blanks.

Chapter 3: describes the methods adopted for successful welding of similar and dissimilar joint by using MPAW. It also describes a details experimental procedure for measuring formability using the developed portable LDH test setup.

Chapter 4: presents the formability study of micro plasma arc welded 316L stainless steel thin sheet joint.

Chapter 5: represents the characterization of mechanical behavior in solution treated micro plasma arc welded blanks of Inconel 625.

Chapter 6: deals with the influence of fusion zone metallurgy on the mechanical behavior of Ni based super alloy and austenitic stainless steel dissimilar joint.

Chapter 7: constitute with conclusions of the research work with future scope of the present research work.

Finally, the thesis is ended with a comprehensive list of references.

Chapter 2
Literature Review

2.1 Introduction

The arc welding process is the most popular joining technique which can weld similar or dissimilar materials together by fusing them above their melting temperature. Which make it differs from the other welding techniques like solid state welding, where two parent materials are joint together with the help of mechanical pressure and heat (Mishra & Ma, 2005). The solid state welding process is limited to join of softer materials such as aluminium and copper. With high strength materials like steel and Inconel, the operational expenses escalate due to tool wear during solid state welding (Raj & Biswas, 2023). Consequently, fusion welding methods are extensively used in fabrication industries for joining various combinations of materials, both similar and dissimilar, because of their high efficiency in production and cost-effectiveness. The Plasma arc welding (PAW) process is a type of arc welding process in which the plasma is used for welding. Plasma is the fourth phase of matter where a portion of the gas becomes ionized, which has ability to conduct electric current (Bittencourt, 2013). The PAW is an advancement of TIG welding process wherein the materials coalescence together with the help of constricted arc developed between non-consumable tungsten electrode and the workpiece. The PAW differs from TIG welding in the fact that it uses both orifice and shielding gases. In TIG welding, the electrode protrudes from the nozzle, whereas in PAW, it retracts into the nozzle. Therefore, the chances of tungsten contamination or melting of electrode is very less.

In PAW machine, the plasma torch, shielding gas, plasma gas, cooling water, and power supply are connected to a single unit *i.e.* plasma control console (Fig. 2.1). A distinct property of the PAW is pilot arc in PAW system. During the PAW the pilot arc is initiated with the help of a HF generator between the tungsten electrode and the copper nozzle. Hence during starting of the pilot arc it retains inside the nozzle. When the circuit is closed the plasma start to jump to the workpiece and produces enormous heat and reaches temperature above the melting point of the material. The PAW can be classified into two basic categories i.e. transferred and non-transferred arc. In the transferred PAW the arc is formed between the electrode (-ve) and the work piece (+ve). In other words, arc is transferred from the electrode to the work piece. The transferred arc produces high power density and plasma jet velocity. Due to this reason it can be employed for cutting and melting of metals as plasma cutter.

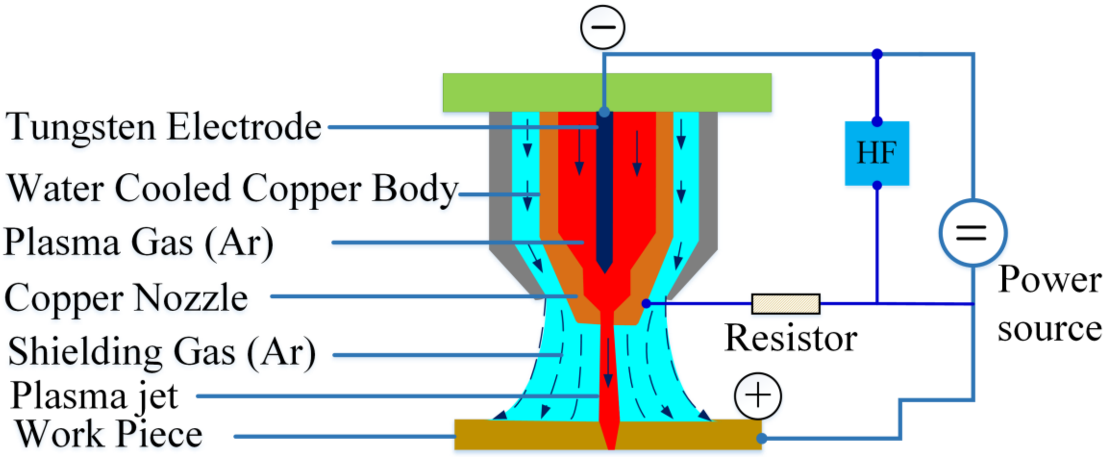

Fig. 2.1 Schematic of MPAW torch

Alternatively, for the case of non-transferred type PAW, the arc is formed between the electrode (-ve) and the nozzle (+ve). The plasma arc comes out through the nozzle as a flame. At the initial the arc is independent of the work piece and the work piece does not form a part of the electrical circuit. The arc can be moved easily from one place to another and can be better controlled. The non-transferred type of PAW possesses relatively less power density as compared to a transferred PAW process, thus it is employed for welding applications. The PAW is also categorized into three distinct types based on current ranges i.e., MPAW: 0.1-15 A, medium current PAW: 15-100 A and keyhole PAW: >100 A (Lucas, 1990). The term MPAW has been coined due to its capability to sustain an exceptionally stable arc, even when operating at welding currents as minimal as 0.1 A (Tseng et al., 2003).

The main problem in any arc welding is abrupt metallurgical changes, particularly at the fusion zone (FZ), represented in Fig. 2.2. Besides, the microstructure of heat affected zone (HAZ) is also affected due to intense heat input during the welding. Because of these metallurgical variations, weld bead exhibits varying mechanical characteristics, including hardness, ductility, and residual stresses, which can affect the formability of welded blank (Xia et al., 2008). More specifically loss of ductility, brittle behaviour of the FZ and less joint strength are the major drawbacks that should be considered in an arc welding process. Thus, the comprehensive aim of this literature study is to understand the details behaviour of MPAW and its consequences on the weld metallurgy and mechanical properties in the form of tensile strength, hardness and formability of similar and dissimilar welded blanks.

This literature review has been divided into five sections such as, Section 2.2 describes about overview of micro plasma arc welding, Section 2.3 discusses the weldability of 316L stainless steel, Section 2.4 reviews the weldability of Inconel 625, Section 2.5 discusses the fusibility of dissimilar joining of Inconel 625 and 316L stainless steel, Section 2.6 reviews the formability of the welded blanks.

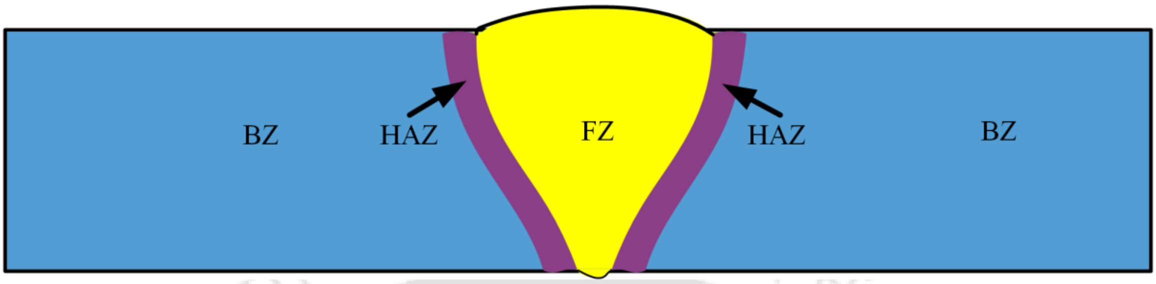

Fig. 2.2 Schematic view of the cross section of welded joint

2.2 Overview of micro plasma arc welding technique

MPAW is a non-consumable arc welding process, it can weld ferrous and non-ferrous sheet materials without having any defects, because of stable heat input at very low current range. It can also able to weld ultra-thin sheets by using narrow and needle like arc, which can minimize weld distortion. Considering this feature of the MPAW, Wang et al. (Wang et al., 2012) had successfully join thin 0.05 mm titanium foil, which is generally used in thin-walled titanium tubes, automobile parts by using MPAW. The MPAW system was developed at Shanghai University of Engineering Science independently. They successfully accomplished welding on one side, achieving formation on both sides and attaining a well-executed welding formation. Due to such characteristics of MPAW, it is used frequently in the field of automobile sector, food processing industries, aerospace, filter assemblies, bellows manufacturing, etc. Many welding techniques are available for the joining of thin sheets like electron beam welding (EBW) (Tomashchuk et al., 2011) and LBW (Kumar et al., 2020). However, these welding techniques are limited by overall setup cost and large working space. With the comparison of such sophisticated welding techniques, MPAW is less expensive and it has ability to weld thin sheets without any defects (Liu, 2015).

2.2.1 Process parameters

The major MPAW parameters are welding current, welding speed, stand-off distance, plasma and shielding gas flow rate and type, electrode material and geometry and nozzle geometry. The proper selection of these process parameters enables best joint quality

(Prasada et al., 2012). The process parameters should be carefully adjusted to maintain appropriate arc stability and weld pool. Otherwise, various welding defects like distortion, excessive or less penetration may encounter during the welding process.

2.2.1.1 Welding current

The welding current in MPAW plays a crucial role to maintain the weld quality by providing proper arc temperature and pressure (Liu et al., 2014). It is observed that excessive current is mainly responsible for wide weld bead both on the top and bottom sides (Prasad et al., 2011). On the other hand, inadequate supply of current creates lack of penetration. In contrast, high current input may undercut or burn through the target material. It is also observed that too high current level damages the electrode during the welding (Liu, 2015). Prasad et al. (Prasad et al., 2012b) optimized the FZ grain size and hardness property in pulsed current MPAW by using Hooke and Jeeves algorithm. It was found that the welding peak current and pulse current are the most important parameters for the FZ grain size and hardness of the micro plasma arc welded joint.

2.2.1.2 Welding speed

Welding speed is another important process parameter that also control the weld bead geometry (Ali et al., 2018). An improper selection of welding speed, may create different types of welding defects like undercut, porosity, arc blow, uneven bead shape and cracking (Rao et al., 2015). Figure 2.3 represents the variation of welding speed with respect to welding current for 0.5 mm 316L stainless steel.

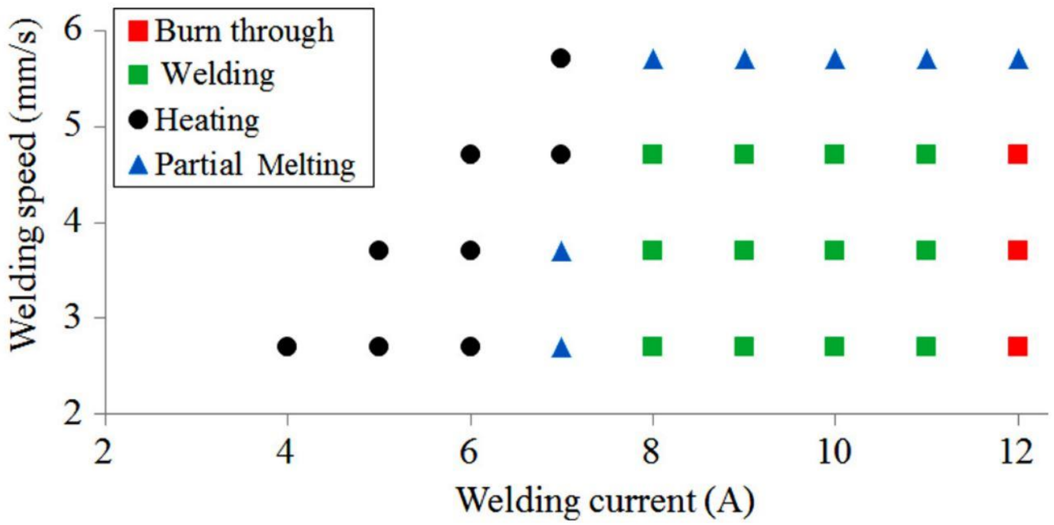

Fig. 2.3 Influence of welding speed and current for 0.5 mm 316L stainless steel (Prasad et al., 2020)

Which predicts that the welding speed has wide range of variation if the welding current is in acceptable range. It is obvious that if the welding speed is too high burn through of the workpiece will occur at high current level (Baruah & Bag, 2017; S. Prasad et al., 2020). On the other hand, if the welding speed is in adequate may burn through the workpiece at higher current level. The depth of penetration is also controlled by welding speed, with increasing welding speed the depth of penetration decreases and it increases when the welding speed is low (Bharathi et al., 2018). However, this phenomenon directly depends on the welding current.

2.2.1.3 Stand-off distance

The gap between the copper nozzle and workpiece is known as stand-off distance (SOD). The SOD is generally considered as the most sensible parameter for the arc stiffness. Jones et al. (Sam Infant Jones et al., 2022) observed that lower SOD created too narrow weld bead and undercuts. Besides, higher SOD, above some optimum range, might create incomplete weld penetration. As the MPAW operates in very low current range (<15 A), in this regard, the SOD plays a crucial role for achieving proper arc penetration. However, some other researcher (Tseng et al., 2003) found that the SOD is less sensitive in controlling weld bead width and penetration (Fig. 2.4.) Nevertheless, too small SOD may lead to undercut and narrow weld. Thus, it is important to maintain a proper SOD for a sound welded joint.

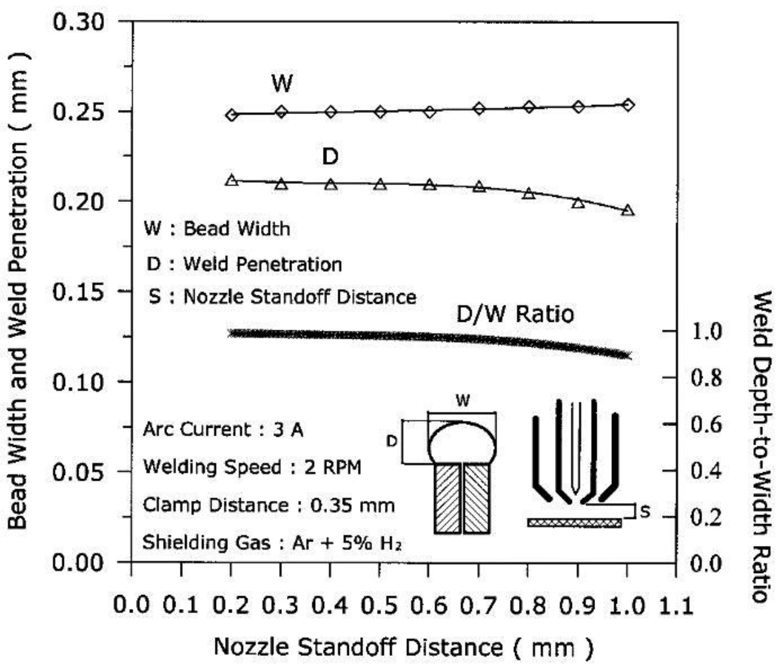

Fig. 2.4 Effect of nozzle standoff distance on weld bead geometry (Tseng et al., 2003)

2.2.1.4 Plasma and shielding gas

Commercially available argon or helium gas (99.8% pure) is generally used for the plasma generation as well as for the shielding purpose. Sometimes, 2-5% H_2 gas is mixed with the argon for welding of specific materials (Lucas, 1990). The composition and rate of flow of the plasma gas has direct effect on the characteristics of the weld pool and appearance of the weld (Martikainen & Moisio, 1993). The life of the nozzle used in MPAW also depends on the flow rate of the plasma gas. The plasma gas flows through the copper nozzle and creates an arc pressure, which mainly helps the arc for more deeper penetration. Besides, the shielding gas passes through the space between outer surface of the copper nozzle and inside of ceramic shielding cap and its main purpose is to protect the molten weld pool from the oxidation.

2.2.1.5 Micro plasma nozzle and geometry

In MPAW the nozzle plays an important role for the formation of columnar shaped arc by constricting the plasma. A copper nozzle is generally used due to its excellent thermal conductivity. It is designed to constrict and focus the plasma arc to achieve high power density. The power density mainly depends on the nozzle orifice diameter and thermal pinched effect of the plasma gas passed through the copper nozzle. The power density can be improved by reducing the copper nozzle bore diameter. However, there is some limitation, when the orifice diameter is reduced the distance between the nozzle inner wall and the hot plasma get reduced. As a result of this the nozzle may damage or the arc becomes branched. Park et al. (Park & Hirata, 2017) conducted an experiment on the micro plasma arc generation and power intensity by constricting the arc by high heat resistant boron nitride submillimeter nozzle. They observed that with the reduction of nozzle diameter the plasma became more constricted and produced high power density. They also observed that with the nozzle diameter of 0.3 mm and discharge time of 5 ms melt spot, ranging from 200 to 300 µm, was formed at 1 A current.

2.2.1.6 Electrode material and geometry

Tungsten is generally used as the electrode material in MPAW. As tungsten has higher melting temperature with comparison of others material, hence during the welding process a less percentage of electrode melting or erosion takes place. Sometimes, 2% thoria is added with tungsten to produce electrode. Due to the addition of thoria, the electron emission capacity of the electrode gets improve. Thus, the electrode can emit electrons at very low temperature (Wang et al., 2003). Depends on the electrode tip condition and shape the formation of arc shape is varied. The contaminated or improper shape tip affect directly to weld bead profile. Hence, most of the time, the geometry of tip of the electrode is maintained as vertex angle.

2.2.2 MPAW of thin sheets

The application of thin sheet materials gained huge significance in different manufacturing industries to reduce overall weight of a system (Basak et al., 2019; Prasad et al., 2020). The welding of thin sheet is one of the important research areas in these industries. For the joining of thin sheets, MPAW is widely accepted welding technique. However, for proper welding, the process parameters optimization is very crucial. Viewing of such importance many research works had been carried out on the optimization of process parameters of MPAW and their effects on the joint qualities like joint strength, ductility and others mechanical properties. Some research works were also conducted on the comparison study between the MPAW and others welding techniques to draw a remarks on the exceptionality of MPAW from others.

Rahimi et al. (Rahimi et al., 2018) studied on the comparative study of pulsed and direct current MPAW of alloy Ti–6Al–4V. The main motive of the work was to evaluate the maximum tensile strength by doing parameters optimization. They observed that by employing an optimal ratio of current and pulsed mode leads to a reduction in the FZ grain size, thereby enhancing the hardness and tensile strength of the weldment. Baruah et al. (Baruah & Bag, 2017) studied the joining of 304 stainless steel and low carbon steel separately by using MPAW. They proposed a process window based on most influencing parameters i.e., welding current and speed for a defect free join for both the steels. It was observed that after welding 304 stainless steel produced a narrow HAZ due to slower heat diffusion rate. On the other hand, the low carbon steel formed a wider HAZ because of high thermal diffusion rate. Javidrad et al. (Javidrad et al., 2014) experimented on the MPAW of thin (0.8 mm) Ti-3Al-2.5V sheets and explained the effect of MPAW on the mechanical and microstructural properties. They concluded that the MPAW was more preferable welding techniques for joining of this alloy within the optimised parameters ranges. Baruah et al. (Baruah & Bag, 2016) performed MPAW of Ti6Al4V alloy sheet of 0.5 mm thickness and evaluated the temperature distribution and weld distortion experimentally and numerically. They observed that when the welding speed was 2–7 mm/s and current 8–13 A, produced a high-quality weld joint. It was also found that the residual stress was mainly developed because of the longitudinal stress instead of transverse stress. Batool et al. (Batool et al., 2016) conducted a comparison study between the MPAW and TIG welding of SS 304. They found that the blanks joint by MPAW had more strength, higher ductility and narrow HAZ with the comparison of TIG welding due to low heat input in case of MPAW.

The MPAW is mainly used for the joining of sophisticated and fine joining work like mechanical below. The MPAW produces narrow welding seam which is very difficult to control in real time welding for complicated shapes. In this regard Zhang (Zhang, 2005) designed a special optical sensor. The application of that system enhanced both the welding quality of the inner circle of metal bellows and the working conditions of the welder. More precise and controllable heat input is the speciality of the MPAW, which help it to join ultra-thin sheets of ferrous and nonferrous alloys without having any defects. Wang et al. (Wang et al., 2012) tried to join thin 0.05 mm Titanium foil, which generally thin-walled titanium tubes, automobile parts by MPAW system developed by Shanghai University of Engineering Science independently. They had achieved one side welding both sides formation and got good welding joint. They successfully accomplished welding on one side, achieving formation on both sides and attaining a well-executed welding formation.

2.3 Weldability of austenitic stainless steel 316L

316L stainless steel is a low-cost structural material, and it is well known for its excellent corrosion resistivity, weldability, and excellent mechanical properties (Sánchez-Tovar et al., 2013). It is generally used in various industries like petrochemical, chemical, offshore structure, etc. (Soares et al., 2019; Soltani & Tayebi, 2018). It has two major phases, namely, austenite (γ) and ferrite (δ/α), which makes it unique from others austenitic stainless steel. It contains less than 0.03 wt.% carbon, which minimizes sensitization at grain boundaries and reduces the risk of intergranular corrosion. Additionally, the dominant austenitic phase in this material prevents embrittlement, thereby eliminating the need for post-weld annealing in most applications (Reza Tabrizi et al., 2021). Chromium, nickel, and molybdenum are the three major elements, which improve its corrosion resistivity, weldability (Landowski et al., 2020), fatigue strength (Saha & Pal, 2021), and formability (Kannan et al., 2021). Similar and dissimilar joins of 316L stainless steel has huge applications in different industries. Different types of welding techniques like LBW, TIG, EBM, MMAW, MIG, etc. are frequently used for the joining of this steel. Depending upon the welding technique microstructure of the FZ and HAZ varies. There are four different mechanism of FZ solidification of 316L stainless steel, they are described in Table 2.1, which is related to Fe-Cr-Ni phase diagram (Fig. 2.5).

The main problem during welding of austenitic stainless steel is the formation of precipitated carbides which are generally deposited at grain boundaries and subsequently reduce its corrosion resistivity (Gooch & Honeycombe, 1980). By providing a regulated heat input, the complications arise during austenitic stainless steel welding can be minimized. Thus, it is important to select proper welding technique for the joining of this steel.

Table 2.1 Solidification types, reaction and resultant microstructure of 316L stainless steel (Lippold & Kotecki, 2005)

Solidification types	Reaction	Microstructure
A	L→L + A→A	Fully austenitic, well-defined solidification structure
AF	L→L+A→L + A + $(A + F)_{eut}$ → A + F_{eut}	Ferrite at cell and dendrite boundaries
FA	L→L+ F→ L+ F+ $(F + A)_{per/eut}$ →F + A	Skeletal and/or lathy ferrite resulting from ferrite-to-austenite transformation
F	L→L+ F→F→F + A	Acicular ferrite or ferrite matrix with grain boundary austenite and Widmanstatten side plates

A: Austenite; AF: Austenite-ferrite; F: Ferrite and FA: Ferrite-austenite

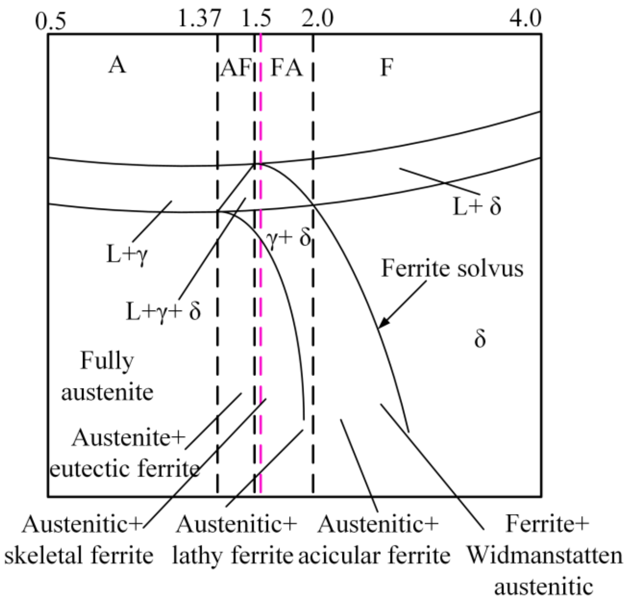

Fig. 2.5 Relationship of solidification type to the pseudobinary phase diagram (Feng et al., 2015)

TIG welding is generally used for the joining of 316L stainless steel. Dadfar et al. (Dadfar et al., 2007) studied the corrosion behaviour of TIG welded 316L stainless steel sheet (2 mm) joint. It was found that the corrosion behaviour of the welded blank was improved with the comparison of base material (BM). As the secondary phases present in the BM got dissolved during the welding process, the corrosion resistivity was improved. Ramkumar et al. (T. Ramkumar et al., 2017) studied the mechanical relationship, corrosion and structural behaviour of similar and dissimilar TIG welded joint of 316L stainless steel and Inconel 718 with 4 mm sheet thickness. At the preliminary study they observed that full penetration only possible by multi-pass welding. The corrosion test performed in NaCl atmosphere, exhibited that the dissimilar joint of these two materials and similar joint of Inconel 718 are having lower corrosion resistivity with the comparison 316L stainless steel similar joint. The main limitation of TIG welding process is that it is limited to welding of lower thickness materials.

Different types of activated flux like SiO_2, TiO_2, Cr_2O_2 etc. are implemented in the TIG welding to overcome this barrier, which is known as activated flux TIG welding (A-TIG). The A-TIG welding works based on the reversed Marangoni convection effect, in which the molten metal flows inward of the weld pool instead of outward. As result of this a high penetration is achieved by using A-TIG welding (Heiple & Roper, 1981) process. Tseng and Hsu (Kuang-hung Tseng & Hsu, 2011) evaluated the performance of A-TIG welding of 316L stainless steel 6 mm plate. Total five types of activated flux i.e., MnO_2, TiO_2, MoO_3, SiO_2, and Al_2O_3 were used to determine their effect on the weld morphology, weld hardness, amount of delta ferrite formation in the FZ and angular distortion of the welded blank. It was observed that by using SiO_2 and MoO_3 flux a high weld penetration was achieved. They also observed that the ferrite percentage at the FZ increased after A-TIG welding and this was happened due to the higher heat input per unit length. Kulkarni et al. (Kulkarni et al., 2020) investigated the mechanical and microstructural behaviour of A-TIG welded dissimilar joint of 316L stainless steel and stainless steel -alloy 800. It was found that the metallurgical heterogeneity at the FZ affects the mechanical properties. Besides, they observed that during the tensile testing a micro crack was developed at the grain boundary of the FZ, which propagated form the HAZ of alloy 800. Sakthivel et al. (Sakthivel et al., 2011) conducted a comparison study on creep rupture behaviour of single pass A-TIG and multi pass TIG welded joint of 316L stainless steel. They observed that welded joints had lower creep rupture behaviour than the as received BM. However, with the comparison of multi pass TIG welded joint, A-TIG welded joint exhibited higher creep rupture resistance. It was also observed that the δ-phase transformed in σ and Laves phase due to the creep exposure. Nevertheless, by using Keyhole gas tungsten arc welding (K-TIG) process, a deeper penetration can be achieved without using any activated flux. Feng et al. (Feng et al., 2015) studied on the joining of 10 mm thick 316L stainless steel plate by K-TIG welding technique. It was observed that the FZ had mainly two phases i.e., austenite and δ-ferrite. They also observed that the corrosion resistivity of the weld better than the BM due to presence of higher percentage of Cr content ferrite.

Laser welding is another advanced welding technique which has ability to weld thin to thick material with good weld quality but it is constrained in the reflectivity of laser due to the polish surface of the workpiece (Cao et al., 2003). Soltani et al. (Soltani & Tayebi, 2018) performed a comparison study between TIG and Nd: YAG laser welding of 316L stainless steel and 304L stainless steel sheets of 1 mm thickness. It was observed that the tensile strength of the TIG welded sample with purging gas was higher than that of the laser welded specimen. Moreover, the fusion zone of the laser welded blank became more brittle due to rapid cooling. Zoeram et al. (Shojaei Zoeram et al., 2017) investigated the laser welded dissimilar joint of Nitinol and 316L stainless steel of 1 mm sheets by implemented a copper interlayer. It was observed that the thickness of the interlayer had great effect on the metallurgical as well as mechanical behaviour of the FZ. However, due to the use of copper interlayer some Cu-rich globules formation took place and their boundaries provided the region of nucleation and propagation of cracks. Ragavendran and Vasudevan (Ragavendran & Vasudevan, 2021) evaluated the effect of laser, TIG-laser and MIG- laser hybrid welding processes on the residual stress and distortion behaviour of 316L stainless steel plates of 5.6 mm thickness. They found marginal differences in residual stress among these three types of welding processes. It was also found that the distortion levels within the welded joint were typically minimal and demonstrate a direct relationship with the volume of weld metal.

Thick 316L stainless steel blank has various applications in nuclear and petrochemical industries but it is difficult to weld thicker material by using conventional arc welding process. However, blessed for EBM which has ability to weld thick materials in a single pass. Alali et al. (Alali et al., 2017) studied the microstructural and mechanical behaviour of 20 mm thick 316L stainless steel plate. It was found the FZ consisted of equiaxed dendritic ferrite and γ-matrix. They observed that the hardness value at the HAZ was higher than the FZ and BZ. This was attributed due to the higher temperature gradient at the HAZ during the EBW, resulted in higher residual stress at the HAZ and increased the HAZ hardness. All tensile samples were failed from the FZ due to the week grain orientation at the FZ. Both thick or thin sheets of 316L stainless steel can be joined with the help of EBW, however, this welding technique has limited use due to its higher setup cost, more workspace requirement, non-transferable and more precise sample preparation is required (Huang, 2010). On the other hand, PAW is a low-cost welding technique which can able to weld thin or thick materials with good joint quality. Chaudhary et al. (Chaudhary et al., 2019) investigated the joining of 0.4 mm 316L stainless steel sheets by using transferred type MPAW in pulsed mode. They found maximum yield strength of 553 MPa with the help of optimum process parameters setting i.e., pulse-on time of 0.05 s, pulse-off time of 0.05 s, peak current of 3.5 A, and welding speed of 250 mm/min. It was also found that due to the using of pulsed mode MPAW, less distortion and no porosity were occurred after welding. Dwibedi et al. (Dwibedi et al., 2018) investigated MPAW of 316L stainless steel sheets of different thicknesses TWB by different types of welding parameters. They reported that a significant reduction in the width of HAZ was achieved by using MPAW. It was also observed that the hardness of the FZ was highest with comparison of HAZ and BM. Saha and Pal (Saha & Pal, 2021) investigated the metallurgical variation and fatigue behaviour of MPAWB of 316L stainless steel thin (0.5 mm) sheet. It was found that the presence of δ-ferrite in the FZ was mainly responsible for the failure of welded blank during the fatigue test. However, more than 90% joint efficiency was achieved by using MPAW. Sánchez-Tovar et al. (Sánchez-Tovar et al., 2011) studied the microstructural and pitting corrosion behaviour of 316L stainless steel micro plasma arc welded blank in LiBr atmosphere. They used in their study 316L stainless steel wire as filler material. A recrystallisation and grain growth was observed at the HAZ. As a result of this the HAZ exhibited highest corrosion rate and lower ability to repassivation with the comparison of BZ and FZ. Sahu and bag (Sahu & Bag, 2020) investigated dissimilar joining of 316L stainless steel and Inconel 718 by using pulse mode micro plasma arc welding process. They observed that due to the formation of intermetallic, weld quality reduced and promoted to solidification cracking in the FZ. It was also observed that the FZ consisted mainly two types of microstructures i.e., columnar and equiaxed dendritic structures, in which the equiaxed dendritic structures contained less percentage of intermetallic. This was attributed due to the using of pulse mode plasma arc welding, which reduced the solidification parameter (G/R) where ‘G’ and ‘R’ stand for the temperature gradient and solidification growth rate.

2.4 Weldability of Inconel 625

Nickel based Inconel 625 is a super alloy, which is strengthened by molybdenum, chromium, and niobium substitutional solid solution (DuPont et al., 2011), which provides its high strength, creep, and corrosion resistivity from room temperature to elevated temperature. In this alloy generally, higher percentage of Cr and Mo are used to provide higher corrosion resistance as well as strength. Besides, Fe and Nb are added to enhance the solid solution strengthening of the alloy. It is also known for its good weldability and fabricability. Hence, it is used in aerospace, chemical, marine, and petrochemical industries in a large scale (Li et al., 2011). This alloy is also used for the fabrication of heat-exchanger tubes in ammonia plant (Shankar et al., 2001). The similar and dissimilar joining of this alloy is a challenging task due to the segregation of alloying elements, formation of Cr-rich carbide at the grain boundaries and different types of intermetallic phases like σ, Laves and P (Ogborn et al., 1995). Which, adversely effects mechanical properties of the welded blank (L. Y. Xu et al., 2018). Hence, the study of weldability of Inconel 625 is important. Different types of welding process are applied for the joining of this alloy, few of them are laser welding, TIG welding, PAW. Caiazzo et al. (Caiazzo et al., 2017) studied the edge joint of Inconel 625 sheets by using laser welding technique. This type of edge joint has broad application in aerospace industries. It was observed that heat input was the main parameter, which could control the formation of porosity. The chance of porosity formation was increased with the increasing heat input. Niaraki et al. (Jelokhani-Niaraki et al., 2016) optimized the process parameters of Nd: YAG LBW of Inconel 625 (0.5 mm thick) sheet. They found that the weld strength was mainly influenced by the heat input. It was also found that due to the higher heat input, the hardness value also increased because of the formation of higher amount of Laves phase. Tlili et al. (Tlili et al., 2022) studied experimental and numerical the flow of molten weld-pool and distribution of temperature of fiber laser welded Inconel 625. They evaluated the effect of fiber laser welding parameters on the temperature distribution, bead dimensions, microstructural changes. It was found that the flow of liquid occurred due to the Marangoni stress and buoyancy force. Besides, due to the intense heat input in LBW, coarse-grain formation was taken place at the HAZ.

Sivakumar et al. (Sivakumar et al., 2021) evaluated the relationship between the mechanical and microstructural properties of TIG and A-TIG welded joint of Inconel 625 (6.5 mm) plate. It was detected that due to the segregation of alloying elements like Nb and

Mo, created microfissure. As a result of this the tensile strength of welded blanks got reduced and this was more pronounced for the case of A-TIG welded blank. Because of the similar reason, the solidification cracking in Inconel 625 welded blank is common phenomena. However, due to the use of A-TIG welding, the chance of solidification cracking was reduced drastically. As discussed earlier that the Inconel 625 has the ability to resist extreme corrosive environment from room temperature to the elevated temperature. Guo et al. (Guo et al., 2021) conducted an experiment on the microstructural variation and corrosion resistance of pulse TIG deposited Inconel 625 on AISI 4130 stainless steel plate. It was observed that the sample positioned near and below the middle surface of the second overlay exhibited significantly superior resistance to comprehensive pitting corrosion compared to others. Moreover, extensive uniform corrosion was observed on the specimen with a single layer of Inconel 625 overlay. No instances of pitting corrosion were detected on the specimens situated within the second layer of the Inconel 625 overlay. Rao et al. (Rao et al., 2015) evaluated the effect of welding speed on the microstructural behavior of pulse current micro plasma arc welded joint of Inconel 625 sheet. They observed that the weld hardness was increased with the increasing of certain level welding speed and thereafter the hardness value started to decreased with the further increase of welding speed. Prasad et al. (Prasad et al., 2012a) evaluated the effect of pulse current on the ultimate tensile strength (UTS) and FZ grain size of MPAWB of Inconel 625. A central composite rotatable design matrix comprising four factors and five levels was employed to streamline the number of experiments and a mathematical model were constructed using response surface method. They observed that the peak current is the most influencing parameter for the UTS and the FZ grain size. It was also observed that with the increasing of peak current the FZ grain started to coarse. Due to the higher peak current the heat input was increased, which reduced the cooling rate and coarsening the grains.

The welding of Inconel 625 is always a challenging task due to thermal cracking (Burger et al., 2021), loss of ductility owing to the formation of laves phase and carbide precipitation (Badiger et al., 2019; Su et al., 2021). Many researchers around the world are concentrating their research work for improving the weld metallurgy of Inconel 625 by exploring weld parameter optimization, post-weld heat treatment, choosing suitable filler material, and venturing different welding techniques (Wang et al., 2022; Xing et al., 2014). Aging and solution treatment (ST) are the important post welding heat treatment process, which is generally designed for the restoration of weld strength by the modification of precipitation and reduction of residual stress generated after the welding process. Figure 2.6 represents time-temperature-transformation (TTT) diagram of Inconel 625.

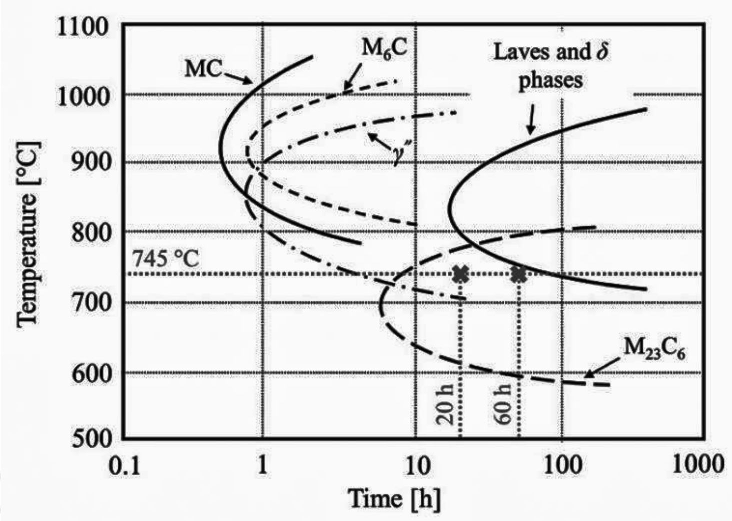

Fig. 2.6 TTT diagram of alloy Inconel 625 (Mostafaei et al., 2016)

The TTT diagram describes the formation of different type of carbides, precipitates and intermetallic, which are depend on the elemental variations, time and temperature in different types of heat treatment process. Zhang et al. (Zhang et al., 2022) studied the effect of solid solution temperature on the mechanical and microstructural properties of plasma arc welded blank (PAWB) of Inconel 625. The heat treatment was carried out by following the temperature ranges from 950-1150 ºC with 50 ºC interval and 1 h holding time. Thereafter, the heat-treated sample was cooled by air up to room temperature. It was observed that when the heat treatment (HT) temperature was 950ºC, the carbide presents in the BM started to precipitated at the γ boundary and when the heat treatment temperature was 1050ºC, the carbides completely melted and found distributed over the matrix. Besides, the dendritic structures and Laves phases in the FZ were completely melted and formed cellular crystal structures. As a result of this the failure of tensile specimen was taken place from the BM as well as good tensile strength and percentage elongation were achieved at this temperature. Hu et al. (Y. L. Hu et al., 2020) studied the effect of ST on the laser deposited Inconel 625 powder and it was found that due to the ST, the dislocation density and the size of Laves phase were reduced. The material elongation was also improved drastically. Mostafaei et al. (Mostafaei et al., 2016) measured the effect of solutioning and ageing on the mechanical and microstructural properties of binder jet printed Inconel 625. They observed that due to the ageing treatment different types of intermetallic phases like Ni_3Nb, $Ni_2(Cr, Mo)$ and carbides like NbC, $Cr_{23}C_6$ were formed. Due to the presence of such phases the joint strength and hardness were increased. Inversely, the overall ductility of the solution treated specimen was reduced. Yang et al. (Yang et al., 2020) investigated the effect of ST of hot rolled Inconel 625 plate in three different temperatures. They observed that when the temperature range reached above the 1150 ºC the carbide particle started to dissolve near the grain boundaries and grain growth started rapidly. It was also observed that the hardness and strength of the solution treated sample were reduced and percentage of elongation was increased. Zhong et al. (Zhong et al., 2023) investigated the effect of thermal ageing on the mechanical and micro structural properties of high-speed laser deposited blanks. It was observed that when the ageing temperature was above 700 ºC, the dendritic microstructure started to disappear gradually and formed MC type carbides. It was also observed that with the increasing of ageing temperature (900 ºC >) elongation was increased but overall strength of the blank was reduced due to the formation of carbides. Liu et al. (Liu et al., 2023) conducted an experiment on partially recrystallized cold-rolled Inconel 625, subjecting to ST at various holding temperatures for 10 minutes. The ST resulted in the attainment of favorable mechanical properties. The full recrystallization of grains led to the formation of elongated equiaxed grains. These elongated grains hindered the flow of dislocations, while the equiaxed grains facilitated dislocation flow. Because of the combination of these two phenomena, mechanical properties of the solution treated specimen was improved.

2.5 Feasibility of dissimilar joining of Inconel 625 and 316L stainless steel

The joining of dissimilar materials is essential for cost reduction and enhancing system flexibility across various industries. This research area holds significant importance, which has high demand in different industries. However, welding of two dissimilar materials with different thermal properties like thermal conductivity and melting temperatures is a difficult task (Kou, 2003). Nickel based Inconel 625 is used in aerospace, chemical, marine, and petrochemical industries on a large scale (Guo et al., 2011). This alloy is also used for the fabrication of heat-exchanger tubes in ammonia plant (Li et al., 2017). On the other hand, 316L stainless steel is an inexpensive structural material. It has high corrosion resistivity and superior mechanical properties. The 316L stainless steel is used in offshore plants, chemical and food processing industry, automobile exhaust systems, nuclear power plants and biomedical application (Kale et al., 2021; Masoud Sabzi & Dezfuli, 2018a). It contains less carbon percentage, which helps to control the formation of metal-carbides in welding. The solidification cracking of the weld bead can also be improved by the presence of δ-ferrite during welding of 316L stainless steel. The ductility and fracture toughness of this steel are also improved by fine dendritic structure of the weld (T. Ramkumar et al., 2017). The combination of these two materials offers a wide range of applications. Some components that are fabricated from Inconel 625 can be joined together with parts made of 316L stainless steel, which possess similar properties. This approach can effectively reduce both weight and cost.

The dissimilar joint of austenitic stainless steel and nickel-based super alloy has extensive applications in the field of nuclear industry, sub-size boilers (Dreshfield et al., 1992), etc. Thus, lots of researchers emphasizing their research work to fabricate these two dissimilar materials using different type of welding techniques.

Dokme et al. (Dokme et al., 2018) experimented dissimilar joining of 316L stainless steel and Inconel 625 by pulsed and continuous TIG process with two different types of filler wire i.e., ERNiCr-3, TIG 316L. It was observed that no grain growth was taken place for the case of pulse TIG. With the using of pulse TIG the mechanical properties were improved sharply. Kourdani et al. (Kourdani & Derakhshandeh-Haghighi, 2018) performed a comparison study between the SMAW and TIG welded dissimilar joint of Inconel 625 and 316L stainless steel. They had two types of filler wire i.e., ERNiCrMo-3 and ERSS316L and ENiCrMo-3 electrode. Table 2.2 represents the different of electrodes and their composition. It was observed that during the solidification of ERNiCrMo-3 filler metal, the Nb and Mo got segregated and deposited into the inter-dendritic grains. On the other hand, with the using of ERSS316L filler metal, less elemental segregation was observed. Hence, the chance of transformation from cellular to dendritic or equiaxed structure of the FZ was reduced. It was also observed that a fine FZ microstructure and less Nb segregation was observed for the case of TIG welding process. This phenomenon mainly occurred due to the less heat input during the TIG welding process. Kumar et al. (Kumar et al., 2015) investigated the metallurgical and mechanical characterization of dissimilar TIG welded blank of Inconel 625 and 316L stainless steel with a thickness of 5 mm. Two distinct filler materials i.e., ER2209 and ER-NiCr-3 were used for the joining purpose and the welding was carried out by continuous and pulse current mode. It was found that the pulse current TIG was superior than the continuous current TIG in the formation of HAZ. The bimetallic tensile sample was predominantly failed from the weak 316L stainless steel parent material side.

Table 2.2 Chemical compositions of filler or electrode materials

Filler/Electrode	C	Cr	Si	Ni	P	Mn	Nb	Mo	Fe	Others
ERNiCr-3	0.04	20.0	0.09	73.0	0.003	2.8	2.4	-	1.5	<0.5
ERNiCrMo-3	0.03	20.9	0.05	65.9	0.019	0.05	3.5	8.5	0.9	<0.15
ENiCrMo-3	0.05	21.6	0.46	63.4	0.002	0.01	3.21	9.4	1.6	<0.26
ERSS316L	0.02	18.8	0.44	11.4	0.017	1.71	-	2.2	65	<0.41

Ajabshiri et al. (Ajabshiri et al., 2022) studied the dissimilar transient liquid phase bonding (TLP) of Inconel 625 and 316L stainless steel by using a Cu interlayer. The TLP bonded samples were prepared by holding the specimen at 1100ºC for 15, 20 and 30 minutes. The microstructural analysis showed that the interphase between the Cu interlayer and Inconel 625 contained Mo and Nb rich MC types carbide. The bonded specimen prepared for 30 minutes was exhibited maximum UTS value and the failure of the tensile specimen was ductile in nature. Sasikumar et al. (Sasikumar et al., 2022) prepared a functionally graded material (FGM) of 316L stainless steel and Inconel 625 by GMAW which was based on arc additive manufacturing. The microstructural result reported that the 316L stainless steel consisted of columnar and equiaxed dendritic structures and a regular grain growth was observed in the interface between the 316L stainless steel and Inconel 625. Besides, for the case of Inconel 625, Laves phase was found in the inter dendritic region. The tensile sample prepared from interface of these two alloys, was failed from the 316L stainless steel side due to lower strength with comparison of Inconel 625. Liu et al. (Liu et al., 2023) fabricated a bimetallic structure of alloy 316L stainless steel and Inconel 625 by cold metal arc additive manufacturing. The microstructural results reported that the microstructure after multilayer deposition, the 316L stainless steel consist of two major phases like austenite and ferrite. Besides, Inconel 625 consisted of primarily austenite matrix and different types of precipitates at the interphase due to the segregation of alloying elements like Nb and Mo.

2.6 Formability of similar and dissimilar welded blanks

Two similar thickness but dissimilar materials or two dissimilar thickness but similar materials when welded together they are known as tailored welded blank (TWB). It is frequently used to reduce the weight of the whole setup, and overall cost without scarifying the performance. These WBs are pressed or stamped into the necessary three-dimensional forms, generating structural elements utilized in automotive, aerospace, marine, defence, and various other industries. Figure 2.7 represents typical application of TWB. In conventional practice, to make different types of sheet metal assembly, the sheets are formed individually and thereafter they are joined together with the help of welding technology. Alternatively, the similar and dissimilar sheets are seam welded together and subsequently formed them. However, joining of dissimilar materials like steel with others alloy is always a challenging task due to the dissimilarities in their mechanical and thermophysical properties. Because of welding, a huge metallurgical variation is taken place at the FZ, which affect the formability of welded blanks (Guzman-Aguilera et al., 2018). The LBW, TIG, MIG, EBW, PAW, friction stir welding are the most popular joining technology which are generally assigned for the preparation of different types of welded blank in different industries. However, LBW and EBW are most popular welding technology used for the production of welded blanks, which have the ability to produce fine HAZ.

Narayanan et al. (Narayanan & Narasimhan, 2008) investigated the formability of laser TWB blank of steel by considering the parameters such as welding conditions, weld orientation, weld region and location of weld. They performed LDH test to measure the formability of the welded blank. It was observed that the weld region had negligible effect on the FLC when the weld region was kept in middle. Besides, when the weld region was kept offset location from the center of the die, the limiting strain decreased with the comparison of as received BM. Katiyar et al. (Katiyar et al., 2021) studied the crushing behaviour of laser welded stretched dome. They used EDD steel sheets with three different thicknesses i.e., 1 mm, 1.2 mm and 1.6 mm to fabricate similar and dissimilar welded blanks. As in biaxial stretching condition the LDH can be improved by placing a lubricant in the interphase of the punch and the blank, they stretched all specimens in lubricated condition by maintaining 14.10 ± 0.15 mm LDH. Thereafter, the fabricated stretched domes were crushed by pressing them between two flat plates. According to the energy absorption result they observed that laser welded blank and laser TWB were more efficient than the EDD steel.

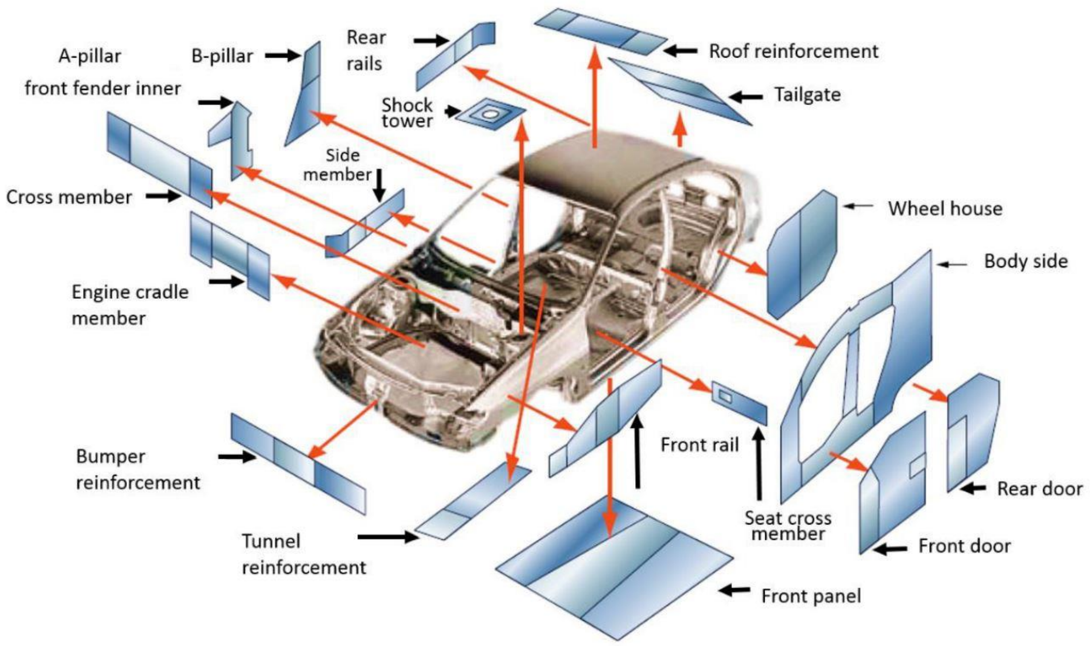

Fig. 2.7 Application of TWB blank in car body (Kashani et al., 2015)

Bandyopadhyay et al. (Bandyopadhyay et al.) also conducted formability study on the laser TWBs of dual phase steels (DP600, DP980) and interstitial free (IF) steel of 1.2 mm sheets. The formability of the TWBs was measured by conducting Erichsen cupping, deep drawing and double-stage forming tests. It was observed that the formability of DP600 laser welded blank decreased by 28% with the comparison of BM due to the presence of weld line. A weld line movement was observed due to dissimilar deformation behaviour of materials. However, failure of the TWBs were taken place from the weaker side. Wu et al. (Wu et al., 2022) evaluated the microstructural variation and dynamic mechanical behaviour of laser welded dissimilar joint of QP1180 (1.2 mm) and TRIP780 (1.4 mm) steels. They performed Erichsen cupping test to measure the formability of welded blank. It was found that the formability of the dissimilar welded blank was mainly influenced by the location of the weld line. The weld line at punch center, exhibited minimum Erichsen value. On the other hand, when the line was offset from the punch center, maximum Erichsen value was observed. This was happened due to the presence of martensite at the FZ, which made it harder with comparison of two BM. Li et al. (Li et al., 2013) studied the effect of weld line position and geometry on forming behaviour of high strength low alloy steel (HSLA) and dual phase steel (DP600 and DP980) laser welded blank. They prepared two types welded blanks i.e., linear and curve linear and performed the LDH test by keeping the weld center 0 mm, 15 mm and 30 mm offset distance which is represented in Fig. 2.8. It was found that the weld line position and geometry and HAZ softening were the more dominating parameters in the formability of the welded blank. It was also observed that when the weld line located far from the blank center, maximum LDH was achieved. Besides, when the weld geometry transformed linear to curve linear, increased the HAZ and it had direct effect on the formability of the welded blank and this was more pronounced for the case of DP600 steel.

Wei et al. (Wei et al., 2015) tried to improve the formability of dual phase DP780 and DP980 steels laser welded blank by local cooling. In this regard they prepared a setup to cool the softened HAZ to enhance the formability of the welded blank, the details of the setup is described in Fig. 2.9. It was observed that due to local cooling the martensite tempering was reduced. As a result of this the HAZ softening was reduced drastically up to 50% for both the materials. Besides, due to the local cooling, the chance of failure from the soft HAZ was reduced and good mechanical properties were achieved specially the ductility of the welded blank. Hamada et al. (Hamada et al., 2022) performed a study on the mechanical and forming behaviour of laser welded AISI 201 and Docol S355 blanks. The laser welding was performed by varying the laser power, welding speed, focal position level, specific point energy as welding parameters with four different values. Besides, the formability was achieved by performing the Erichsen cupping test. It was observed that the FZ mainly consist of martensitic microstructure. The stretch forming results reported that the Erichsen cupping depth value of the welded blanks were lower with the comparison of BM and during the cupping test the failure of the welded blanks were taken place from the high strength Docol S355 side. Xia et al. (Xia et al., 2007) conducted a comparative study on formability of DP980 and HSLA steels bead, welded by diode laser. It was observed that the formability of the DP980 welded blank showed a significant reduction when compared to the BM. The welding speed also had some impact on this decrease. In contrast, the formability of the HSLA welded blank remained consistent with that of the BM formability.

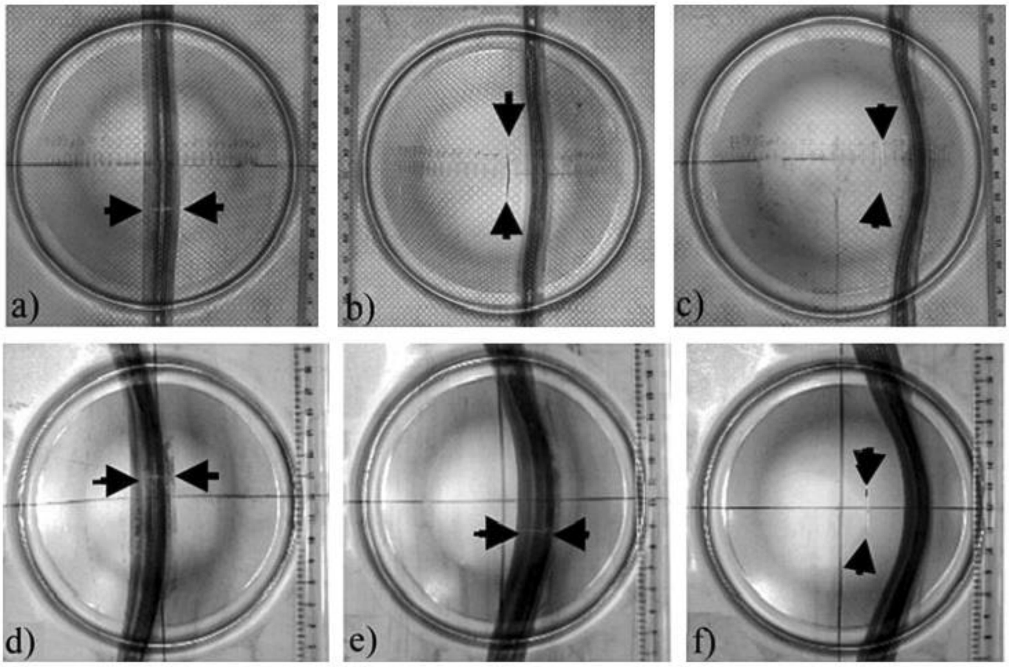

Fig. 2.8 Failure locations in formed (a–c) linear and (d–f) curvilinear HSLA welded blanks with weld line positions of 0 mm, 15 mm, and 30 mm from center. (Li et al., 2013)

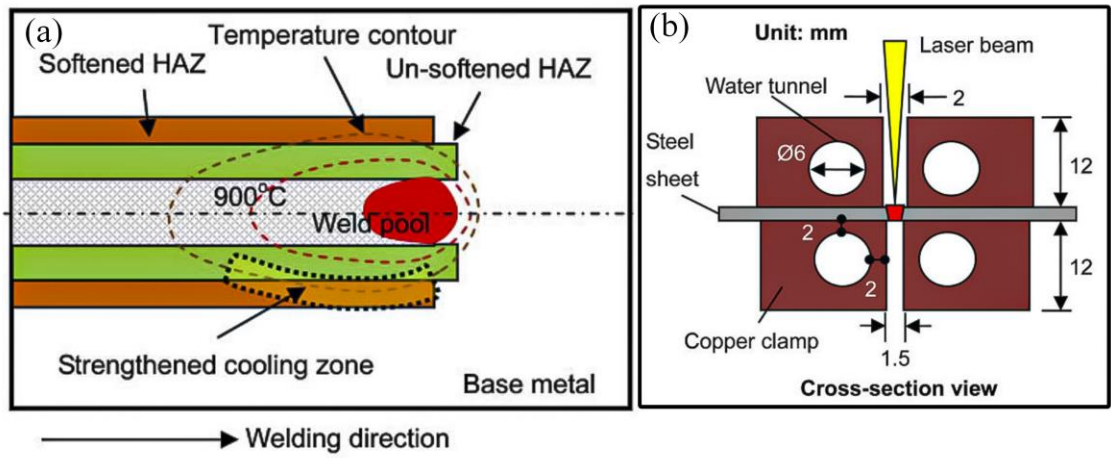

Fig. 2.9 (a) Schematic of laser welding and (b) cross section of LBW setup (Wei et al., 2015)

A complex shape can be achieved easily by using hydraulic or pneumatic bulging system. Which has high demand in different industries where high precession is required. Wang et al. (Wang et al., 2016) evaluated the formability and microstructural behaviour of laser welded TA15 (2 mm thick) tube by hot (800 ºC) gas forming process. Before the bulging test they heated the die and the pipe up to 800 ºC by using an inductive coil. Thereafter, the bulging process was taken place by providing pressure by pressurized gas.

After the completion of bulging the bulged pipe was cooled by water into room temperature. They obtained maximum 73.9% bulging ratio without failure. They also observed that the weld seam hindered the deformation due to its higher strength and due to this similar reason weld seam deformed little. Kumar et al. (Kumar et al., 2018) studied the weld line displacement and maximum bulge height of laser TWB of interstitial free steel with different thickness. A hydraulic bulging test had been carried out to measure the maximum dome height and weld line movement. These effects were also analysed by using fine element analysis. It was observed that with the increasing of thickness ratio the maximum bulge height was reduced and the weld line shifted towards the thicker material side. They also concluded that by using hydroforming process, a uniform bulge profile was achieved. However, a small LDH variation was observed from the BM due to the presence of FZ in TWBs.

The EBW is generally used for those materials which are affected by atmospheric contaminations because this welding process is performed in vacuum. Thus, it gains huge demand in different industries where such types of materials joining is required. Prakash et al. (Lin Prakash et al., 2018) investigated the effect of weld line orientation on the formability of electron beam welded different thickness (1 mm and 2 mm) TWB of CP-TI grad 2. The TWBs were prepared by maintaining weld line parallel and perpendicular to the rolling direction (RD). It was reported that lower ductility, UTS and LDH were observed for the case of TWB, which had the weld line parallel to the RD. This indicated that the weld line orientation to the rolling direction had significant effect on the mechanical behaviour of the TWBs. Dinda et al. (Dinda et al., 2016) studied the microstructural and mechanical behaviour of EB welded dissimilar joint of Fe–Al alloy and plain C-Steel. Based on two distinct welding parameters i.e., with or without beam oscillation and higher welding speed, three different types of TWBs were prepared. It was observed that the welded blank prepared by using beam oscillation, had uniform FZ microstructure with the comparison of without beam oscillation and higher speed welded blank. As a result of this the Ericson cupping value of the welded blank prepared with beam oscillation had maximum value. However, the EBW is limited in use due to its huge setup cost and complexity in the fabrication of welded blank. Hence, many researchers chosen alternative option such as TIG and PAW.

Attique et al. (Attique et al., 2024) performed single point incremental forming of AISI 201 and DC06 steels TWB, joined by TIG welding process. It was observed that due to huge strength and hardness differences between these two steels reduced the forming depth. Wan et al. (Z. Wang et al., 2023) investigated the microstructural and deformation behaviour of TIG welded joint of 7075-T6 aluminium alloy by partial hot rolling. A partial hot rolling process was implemented in which the excess weld bead was hot rolled up to the thickness of the BM and entire process is describe in Fig. 2.10. Because of this thermomechanical heat treatment process, improved the inhomogeneity of the microstructure at the FZ, HAZ, BZ and increased the Erichsen cupping value. Not only the strength of the thermomechanical heat-treated welded blank had more than the solely post weld heat treated specimen. Pramod et al. (Pramod et al., 2020) studied the formability of duplex stainless steel 2205 thin sheet plasma arc welded blank by measuring the Erichsen cupping value. It was observed that the ferrite percentage of the FZ was 55% which was more than that of the BM (52%). As a result of this the Erichsen cupping value of the welded blank was reduced.

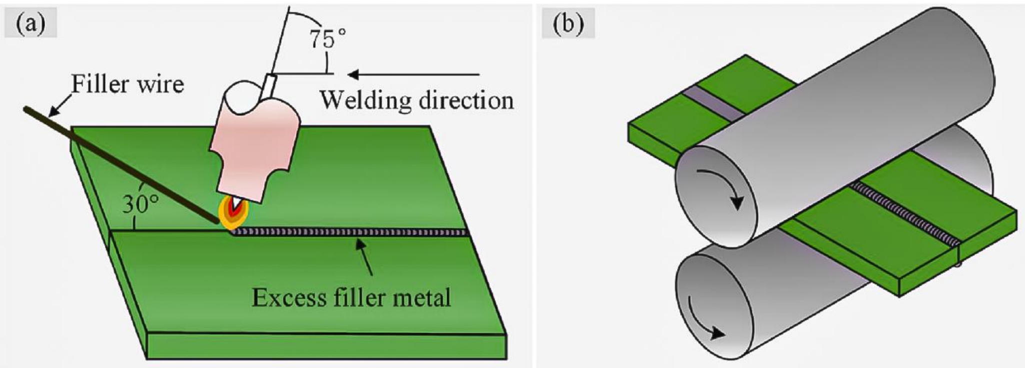

Fig. 2.10 Schematic diagram (a) welding process; (b) rolling process (Z. Wang et al., 2023)

Friction stir welding is comparatively new joining technique which was developed mainly to weld aluminium, magnesium and its alloys. This welding technique is a solid-state joining process in which soft HAZ zone is not present. Thus, the demand of this joining technique is increased where the HAZ behaviour is more crucial. Moayedi et al. (Moayedi et al., 2020) investigated the effect weld orientation on the formability of similar material and dissimilar thickness St14 friction stir TWB. In this regard they prepared three friction stir welded blank, which had 0°, 45° and 90° weld orientation against the principal stress direction. The different strain path specimens were prepared by following the Nakazima stretch forming test. It was observed that the transverse weld orientation displays the highest formability uniaxial tension condition, whereas the longitudinal weld orientation exhibits superior formability in the in-plane strain condition. However, for the case of biaxial specimen had no effect of the weld orientation. Lee et al. (Lee et al., 2009) conducted experimental and numerical study on the formability of friction TWB of 6111-T4, 5083-H18, 5083-O aluminium alloy, dual-phase steel (DP590) and AZ31 magnesium alloy because of their high demand in automobile sector. To depict the mechanical characteristics in the numerical examination, the Yld2000-2d non-quadratic orthotropic yield model was employed for the aluminium alloy and DP590 sheets. Simultaneously, the AZ31 sheet utilized the Cazacu anisotropic/asymmetric yield model, considering distinct hardening behaviours in tension and compression. They found that AA5083-H18, AA5083-O and AZ31 TWB sheets welded blank had good formability with the comparison of BM. However, all TWBs except AA5083-O were found with lower strength. They also concluded that if the primary direction of major principal loading coincided with the weld zone line, the ductility of the weld zone held greater significance. Contrarily, when the major principal loading direction was perpendicular to the weld zone line, the strength of the weld zone became more crucial. Karami et al. (Karami et al., 2021) made comparison study between the TIG and friction stir TWBs of 316L stainless steel and St37 in their formability. It was found that due to the grain growth at the HAZ of St37 steel in TIG welding process, reduced the formability of the TWB blank. Besides, the friction stir TWB exhibited 38% more formability with the comparison of TIG welding process due to the absence of abrupt metallurgical variations. Similarly, Kannan et al. (Kannan et al., 2021) evaluated the effect of weld line orientation on the formability of 316L stainless steel cold metal transfer TWB. Two different types of TWBs were prepared i.e., weld line parallel and another one was transverse to the rolling direction. It was found that The Erichsen cup height of TWBs was lesser in comparison to BM. In all TWBs, the fracture location commenced and extended away from the FZ, running parallel to the weld line. Xiaoyan et al. (Yu et al., 2023) fabricated a FGM of 316L stainless steel and Inconel 625 by using dual wire plasma arc welding. They observed that the interface region between the two metals exhibited strong bonding and a microstructure devoid of any defects.

2.7 Major gaps in the literature

After an extensive review of the existing literature, several research gaps are emerged, paving the way for a focused and comprehensive investigation. The gaps found from the literature are stated as follows.

- A number of researchers had conducted their investigations on the mechanical and microstructure behaviour by optimizing process the parameters of micro plasma arc welded 316L stainless steel joint. However, there is no literatures are found on the formability of 316L stainless steel micro plasma arc welded joint.
- Lots of literature have found on the Inconel 625 welding and 3D printed deposition. Most of them had performed solution and ageing post weld heat treatment to improve either joint strength or ductility. However, no open literature has been found on the impact of ST on the formability of MPAWB of Inconel 625.
- Different types of welding technologies were used for the bimetallic join of alloy 316L stainless steel and Inconel 625. However, no open literature has been found that investigates the relationship between metallurgical variances and formability of 316L stainless steel-Inconel 625 micro plasma arc welded bimetallic joints.

2.8 Objectives of the current work

In light of the existing research landscape, this study identifies certain gaps and unexplored areas that prompt a more comprehensive investigation. the objectives of the present work are delineated as follows.

- Evaluate the formability of the micro plasma arc welded blank of 316L stainless steel sheets and its relation with metallurgical behaviour of the FZ.
- Determine the effect of solution treatment on the formability of nickel based super alloy Inconel 625 welded blank, joined by MPAW.
- Analyse the influence of FZ metallurgy on the mechanical properties and formability of 316L stainless steel-Inconel 625 dissimilar micro plasma arc welded joint.

The experimental procedure adopted to fulfil the described objectives, observations and summary of the present work are discussed in detail in the subsequent chapter of the thesis.

Chapter 3
Experimental Procedure

3.1 Introduction

This chapter outlines a comprehensive exploration of the methodologies, techniques, and procedures opted for the execution of welding experiments. It also presents the intricate details of setup development and procedural intricacies involved in testing and analysing the test specimens. Furthermore, it expounds upon the comprehensive pre-weld and post-weld treatment procedures, encompassing the detailed preparations before and after welding for different types of characterization. Additionally, the chapter outlines specifications and details of instruments employed for varies metallurgical and mechanical characterization purposes.

3.2 Sample preparation

The BM received from the vendor, is prepared by cutting into proper dimension using a mechanical shearing machine. Thereafter, the edges to be joint are polished to maintain a zero gap between them. Before the welding, oil, grease, dust particles and others contamination, present on the surface of the workpiece are removed properly by using acetone. The nozzle and the tungsten electrode are also cleaned to remove the oxides for proper functioning.

3.3 Micro plasma arc welding

In the current study MPAW is adopted for similar and dissimilar joining of 316L stainless steel and Inconel 625 sheet materials. The EWM-50 plasma welding machine is used for welding, which has current and voltage ranges from 0.1 to 50 A and 25 to 27 V, respectively, other specification are mentioned in Table 3.1. The mode of welding and polarity of the electrode are melt-in-mode and direct current electrode negative (DCEN), respectively. It can able to weld thin sheets without having any defects. Figure 3.1 represents the schematic view of the MPAW system and photograph of the experimental setup is shown in Fig. 3.2. Plasma console is the main operating unit of the MPAW machine. It also controls water supply for cooling of nozzle and shielding and plasma gas flow rate. A copper fixture is prepared for holding the work piece.

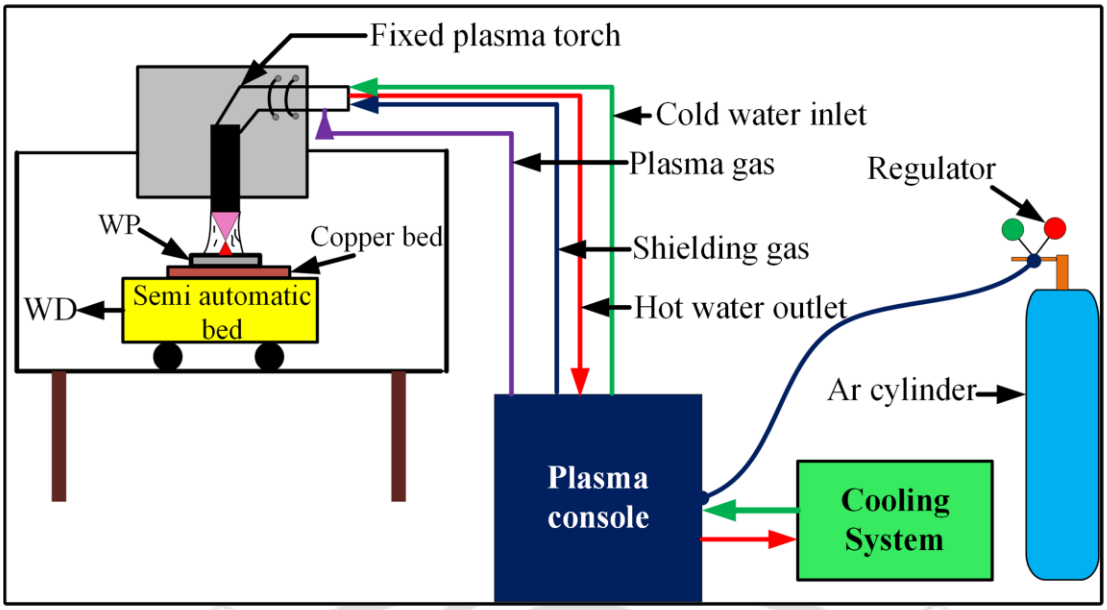

Fig. 3.1 Schematic of micro plasma arc welding setup

Table 3.1 The specification of EWM-50 micro plasma arc welding machine

Specifications	Value
Machine type	Micro plasma 50
Setting range for welding current	0.1 A to 50 A
Setting range for welding voltage	25.0 V to 27 V
Pilot arc current	5 A
Duty cycle 40 °C	50 A (100% DC)
Open circuit voltage Frequency	95 V 50/60 Hz
Ambient temperature	–25 °C to +40 °C
Machine cooling	Fan (AF)
Torch cooling	Coolant

The blanks to be welded are fixed tightly on the copper fixer to reduce the chances of weld distortion, which may occur due to heat accumulation at the time of welding. During the experiment the plasma torch is kept above the workpiece and the workpiece is moved with specific speed, operated by a semiautomatic bed. Before the welding operation, the weld line between the two adjacent sheets is maintained at the center of the nozzle by running the pilot arc. The major influencing parameters for sound weld quality are plasma current, welding speed, stand-off distance, plasma and shielding gas flow rate, nozzle and tungsten electrode diameter. The maximum strength without any defect are the main criterion to decide the optimize value of weld parameters. These optimum level of parameters for all experiments are decided by conducting several bead-on-plate welding and existing literature. A pure tungsten electrode with a 1.3 mm diameter is used in this work. Commercially available pure argon gas is used as the plasma and shielding purpose.

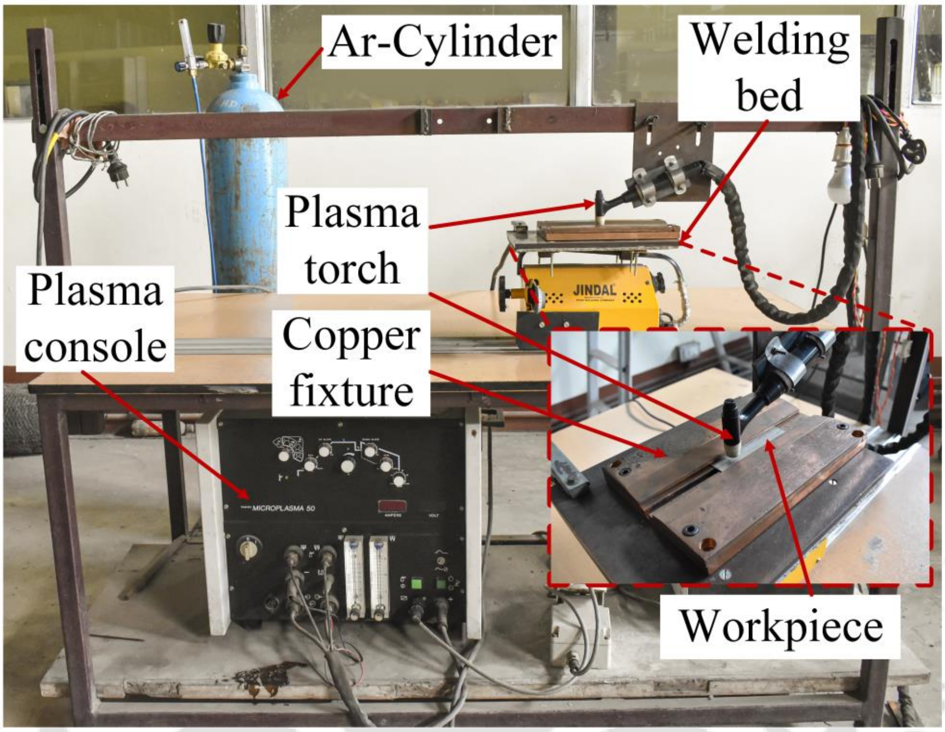

Fig. 3.2 Micro plasma arc welding setup used in this research work

3.4 Experimentation

Two different alloys i.e., 316L stainless steel and Inconel 625 are used in this research work. Combination of these two materials are used to achieve similar and dissimilar welding using MPAW. The experimental procedure of the current research work is divided into three subgroups based on the material combination and processes adopted during the welding. The following paragraphs discusses the details of these subgroups.

Case I represent the similar joining of 316L stainless steel, in which the formability of the welded joint is evaluated by LDH test. In this case, three different types of MPAWBs are prepared with the combination of three groups of process parameters.

Case II in this study similar Inconel 625 sheets are joint together. After welding solution treatment (ST) is carried out to study the effect of ST on the formability of the MPAWB. In this case details metallurgical study is conducted to make a correlation between the metallurgical variations with the mechanical properties.

Case III demonstrates the dissimilar joining of Inconel 625 and 316L stainless steel. The formability of this dissimilar MPAWB is evaluated and compared with the parent materials. The cause and location of failure and relationship between the formability of welded blank and FZ metallurgy is also evaluated in details.

3.4.1 Case-I: Formability study of micro plasma arc welded AISI 316L stainless steel thin sheet joint

Thin 316L stainless steel welded blanks are prepared by using a medium current MPAW machine. The BM is received in rolled and annealed condition. The chemical composition of the sheet is analysed by energy-dispersive X-ray (EDX) technique and is shown in Table 3.2. The sheets are prepared into pieces with a dimension of 100 mm × 60 mm × 0.5 mm (length × breadth × thickness). Before welding, the oil and foreign particles are cleaned from the sheet's surfaces using acetone. Subsequently, the joining faces of the pieces are prepared to obtain a square-butt joint. The welding is carried out along the rolling direction of the sheets.

Table 3.2 Chemical composition of AISI 316L stainless steel (Wt. %)

Element	Cr	Ni	Mn	Mo	Si	Nb	Co	W	S	P	Al	Fe
Wt.%	17.2	9.9	2.0	1.8	0.4	0.4	0.3	0.3	0.2	0.1	0.1	67.3

Four welding parameters, namely, welding current, welding speed, stand-off distance (SOD), and nozzle diameter, are varied. Three different types of MPAWBs are prepared, i.e., Type 1 (T1), Type 2 (T2), and Type 3 (T3), in this study. The parameter settings used for joining the MPAWBs are shown in Table 3.3. The plasma and the shielding gas flow rates are kept constant at 0.4 LPM and 6 LPM, respectively. The distance between the workpiece and the nozzle opening, i.e., the SOD, is maintained using a filler gauge. Before the welding, the weld line between the two sheets is maintained at the center of the nozzle by running the pilot arc. At least three repeat tests have been carried out for each parameter set to check the repeatability of the experimental results.

Six rectangular samples with 80 mm length and various widths viz; S1 (80 mm × 80 mm), S2 (80 mm × 64 mm), S3 (80 mm × 48 mm), S4 (80 mm × 32 mm), S5 (80 mm × 16 mm) and S6 (80 mm × 8 mm) are cut parallel to the weld line to study the limiting strain for different strain paths. Similarly, six samples are cut parallel to the rolling direction to study the limiting strain of BM also. The dimension details of the LDH test specimens are represented in Fig. 3.3.

Table 3.3 Welding parameter settings for different types of MPAWBs

Types of welded blanks	Current (Amp)	Speed (mm/s)	Stand-off distance (mm)	Nozzle diameter (mm)
T1	9.5	3.5	1.5	1.0
T2	10	4	1.7	1.2
T3	10.5	4.5	1.9	1.4

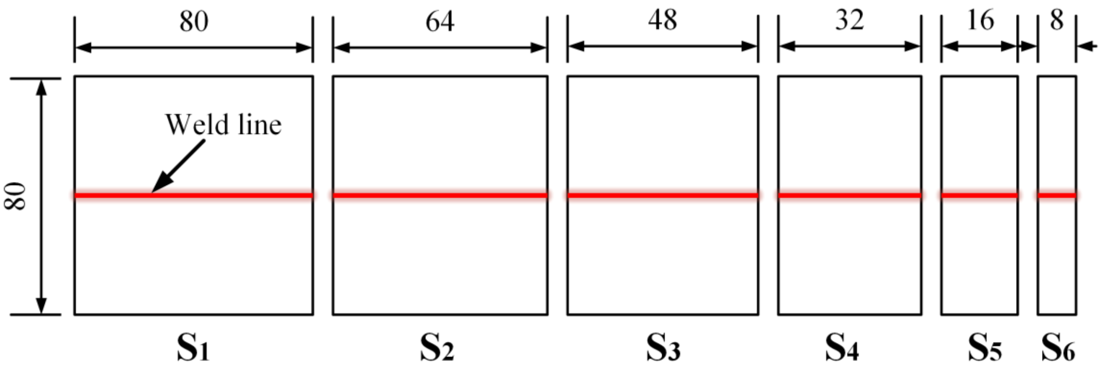

Fig. 3.3 Schematic of LDH test specimens

3.4.2 Case-II Characterization of mechanical behaviour in solution-treated MPAWBs of Inconel 625

Thin 0.5 mm sheets of Inconel 625 are used in this case. The composition of the as-received Inconel 625 sheets is assessed through EDX analysis and presented in Table 3.4. The 0.5 mm Inconel 625 sheets are prepared with a dimension of 110 mm length and 60 mm width and subsequently they are butt joint together with the help of MPAW. The welding parameters are decided by conducting several numbers of trials, the selected welding parameters are: welding current – 11.5 amp; plasma gas flow rate – 0.5 LPM; shielding gas flow rate – 6 LPM; welding speed – 3.5 mm/s; stand-off distance – 1.7 mm; nozzle diameter – 1.2 mm; electrode diameter – 1.3 mm.

Table 3.4 Chemical composition of the as received Inconel 625 sheet (Wt. %)

Element	Cr	Nb	Mo	Ni	Fe	C	Ti	Al	Si	S
Wt. %	24.7	3.4	7.7	57.9	5.2	0.05	0.3	0.2	0.2	0.2

To assess the impact of ST on the mechanical and microstructural properties of the MPAWB, the welded blanks are solution heat treated at a temperature of 1100 ºC for a duration of 60 minutes, followed by quenching in water. The duration of holding time for the ST process is determined based on a preliminary study and relevant findings from prior literature (Y. L. Hu et al., 2018; Mostafaei et al., 2016). In this regard, the MPAWBs are solution treated in three different holding times: 30 min, 60 min, and 120 min. It is observed from the preliminary study that with 60 min holding time, the solution treated welded blank (STWB) exhibits better percentage of elongation with the comparison of other holding times, which is represented in Fig. 3.4. Hence, the entire ST study is conducted at 1100 ºC temperature with holding time of 60 minutes. A schematic representation of the ST procedure, used in this investigation, is illustrated in Fig. 3.5. Thereafter, the metallurgical variation of the MPAWB and STWB are evaluated by different types metallurgical studies.

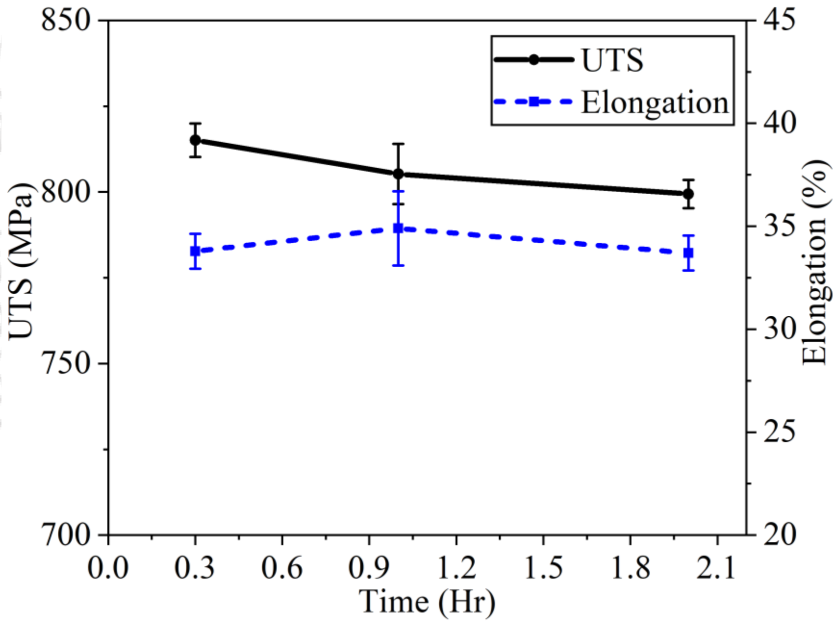

Fig. 3.4 Elongation and UTS variation of STWBs at different holding times

The joint quality and forming behaviour of the MPAWB and STWB are measured by performing micro hardness, tensile and LDH tests and compared with the as-received BM. Six different width specimens are prepared to study the forming behavior of welded blanks, STWB and BM from the biaxial to uniaxial strain path. Three strain path specimens S1, S2, and S3 are prepared according to Nakazima, and remain three S4, S5, and S6 specimens are prepared by following the Hasek standard to avoid premature failure of blanks at the punch and die interface due to width reduction. The Fig. 3.6 represents the geometry and dimension details of different strain path specimens. Finally, the cause of strength and formability variations for different specimens are evaluated systematically by doing a corelative study between the mechanical and metallurgical behaviour.

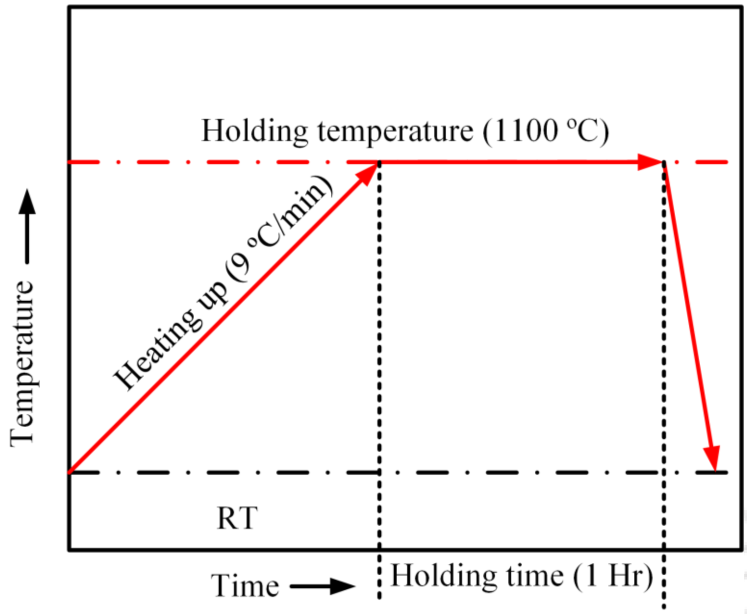

Fig. 3.5 Schematic of solution treatment procedure

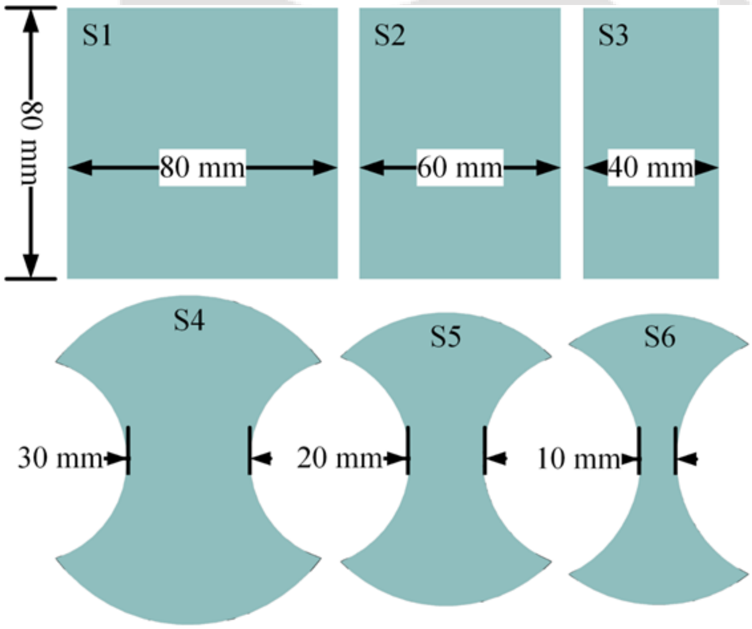

Fig. 3.6 Dimension details of different strain path specimens

3.4.3 Case-III Influence of fusion zone metallurgy on the mechanical behaviour of Inconel 625 and 316L stainless steel dissimilar joint

Nickel based super alloy Inconel 625 and 316L stainless steel of 0.5 mm sheets are used for this case. In which the sheets are prepared with a dimension of 110 mm length, 60 mm width and 0.5 mm thickness. Thereafter, the sheets are butt welded together by MPAW for the preparation of dissimilar welded blank. Similar to previous case the blanks to be welded are fixed tightly on the copper fixer before the welding. The workpiece is moved at a constant travel speed, powered by a semi-automatic bed, while the plasma torch is kept stationary during the welding process. A welding current of 11 A, 3.5 mm/s travel speed, and 1.5 mm stand-off distance are used. Pure (99.8%) argon gas is used as shielding purpose and plasma generation with a flow rate of 6 LPM and 0.5 LPM, respectively. The microstructural variation at FZ of this dissimilar welded blank is evaluated to characterized metallurgical changes in details.

The formability tests are carried out similar to *Case II*, in which six specimens with different widths coded as S1, S2, S3, S4, S5, and S6 are prepared to study biaxial to uniaxial strain paths. The maximum width specimens are stretched both in dry and lubricated condition. The FLD is plotted by measuring the major and minor strains. The surface strain is measured for the S1 and S6 specimens. Besides, the thickness distribution is measured for S1 specimens of BM and MPAWBs to study the variation of thickness after the LDH test.

3.5 Metallurgical investigation

3.5.1 Microstructural study

A small rectangular specimen is cut precisely using wire-cut EDM (WEDM), keeping the weld line at the center for microstructural analysis of various weld zones. Figure 3.7 illustrates the extraction of different specimens for various characterization tests. The specimens cut for microstructural study are mounted into a hot mold for further polishing and examination. Subsequently, the samples are polished with different grades of emery paper to remove scratches and finally the specimens are mirror polished by using a velvet cloth with fine alumina powder (0.3 µm). The polished samples are etched by a chemical etchant for the metallography study. The chemical etchants are selected based on the materials used for different cases. For the case of 316L stainless steel similar welded joint, samples are etched by using glyceregia (1:3:2: HNO_3: HCl:$C_3H_8O_3$). For Case II, the Inconel 625 similar welded joints are etched by an acid mixture of nitric acid, hydrochloric acid, and acetic acid with a ratio of 1:3:2. However, for the dissimilar joint of 316L stainless steel and Inconel 625 a special precaution are taken, the 316L stainless steel side is etched by glyceregia, the FZ and Inconel 625 BM side are etched by an acid mixture of 15 ml HCl, 10 ml CH_3COOH and 5 ml HNO_3. After etching successfully, the grain morphology and composition analysis are carried out by an optical microscope (OM) (Make: Leica; Model: LEICA ICC50 W) and field emission scanning electron microscope (FESEM) (Make: Zeiss; Model: Sigma with integrated energy dispersive spectroscopy (EDS) (Make: Oxford) which are mentioned in Fig. 3.8.

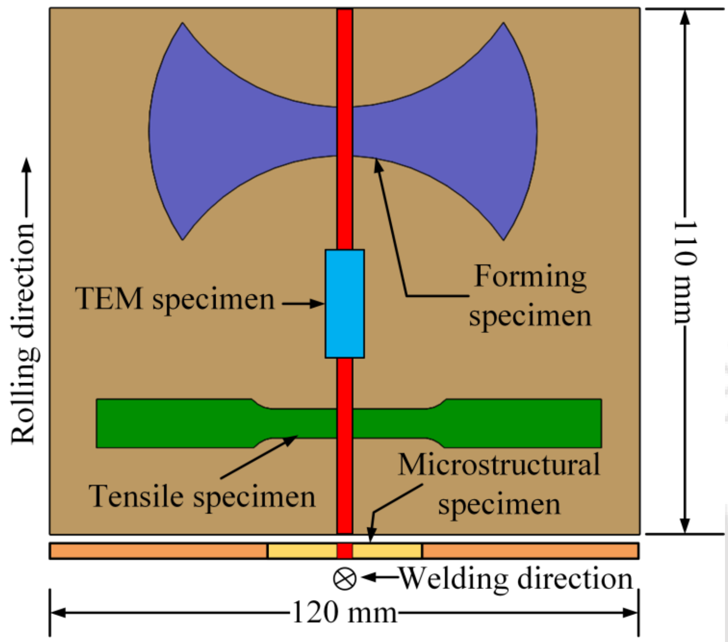

Fig. 3.7 Schematic representation of the MPAW blank with different samples extraction

3.5.2 Transmitted electron microscopy (TEM) analysis

Transmitted electron microscopy (TEM) analysis is a powerful technique widely used in various scientific and industrial fields due to its ability to provide detailed information about the structure and composition of materials at the nanoscale. Hence, to fully understand the microstructural changes of MPAWBs and to find out the different types of intermetallic and secondary phases, the TEM analysis is performed. The TEM microscope (Make: JEOL; Model: 2100F) is operated at 200 kV, which is equipped with Oxford EDS machine and the TEM microscope details is shown in Fig. 3.9 (a). The TEM specimens are prepared by reducing the thickness of the specimen as 60 µm foil by using emery paper and velvet cloth. Thereafter, a small 3 mm disc is punched out from the foil and finally, the samples are electropolished with the help of a twinjet polisher (Make: Fischione; Model: 110), represented in Fig. 3.9 (b). A mixture of ethanol and perchloric acid with a ratio of 9:1 is used for the electro polishing and during the process the ambient temperature is maintained at -20 ºC by using liquid nitrogen.

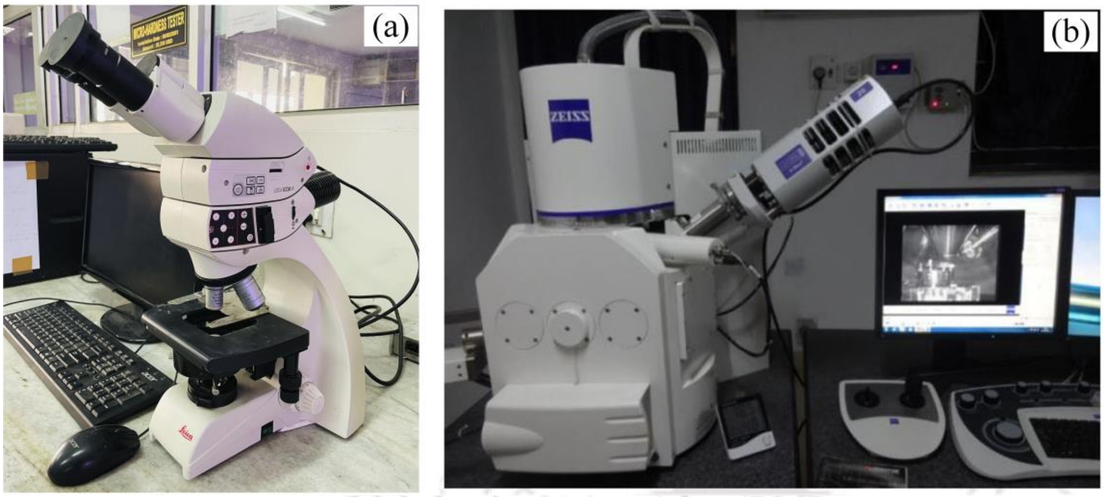

Fig. 3.8 Photographs of (a) optical microscope and (b) FESEM with EDS setup

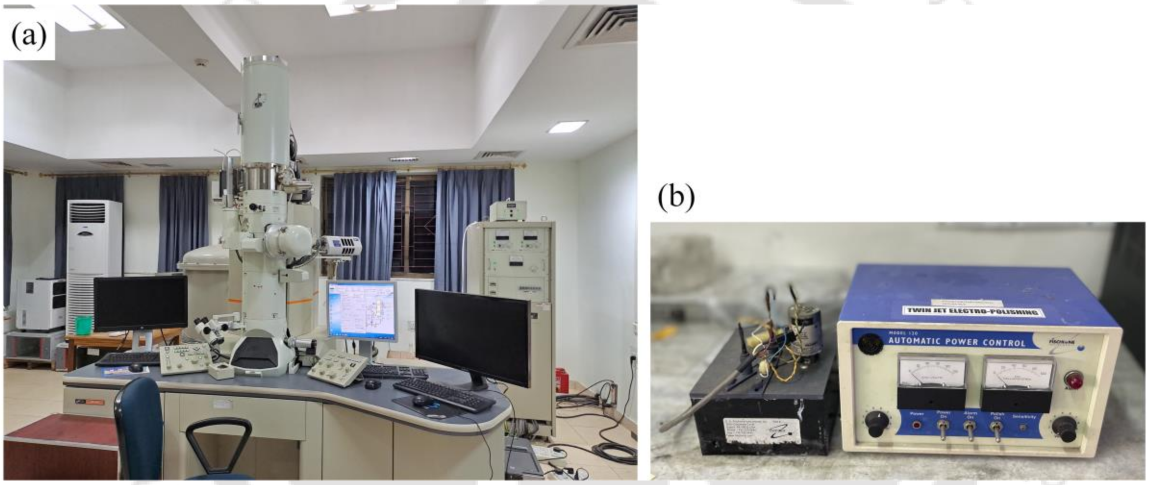

Fig. 3.9 Photographs of (a) Transmission electron microscope and (b) Twin jet polisher

3.5.3 X-ray diffraction (XRD) analysis

The phases present at the FZ and BZ plays a crucial role for the joint metallurgy and mechanical properties. X-ray diffraction (XRD) is a unique method for measuring compound’s crystallinity. XRD is based on the principle of X-ray diffraction by crystals. When X-rays are directed at a crystalline material, the X-rays are diffracted at specific angles determined by the crystal lattice structure. The resulting diffraction pattern provides information about the crystallographic structure of the material. Through XRD analysis, one can identify and quantify various phases exists within a specimen. The intensity of peaks within the XRD pattern serves to indicate the different phases and their compositions. These peak intensities directly correlate with the atomic distribution within the lattice structure. By comparing experimental XRD data with reference JCPDS files (01-082-8282, 00-002-1031 and 00-1999, 023-0298 and 054-0331), one can determine the specific types of phases present in the specimen. It's essential for the experimental results to encompass all major peaks listed within the reference pattern. Detailed specifications of the XRD instrument (Make: Rigaku; Model: Smartlab) depicted in Fig. 3.10 and more specification details are mentioned in Table 3.6. The XRD analysis is carried out for both the BM and FZ. As the MPAW produces a narrow width FZ, thus a small strip of the FZ is cut and polished the surface properly before the XRD analysis.

Fig. 3.10 X-ray diffraction analysis machine

3.6 Micro hardness test

The hardness value always plays a crucial role for the characterization of the FZ. Vickers micro hardness is generally used for thin sample. In this test a diamond indenter is used to make an impression in the form of a right pyramid with a square base and an angle of 136°. Thereafter, the size of the impression left by the indenter is measured by an optical microscope which are used in Equation 3.1 to calculate micro hardness (HV) value.

$$HV = \frac{2F sin\frac{136^0}{2}}{d^2} \tag{3.1}$$

Where, HV is Vickers hardness, F is applied load in kgf and d is arithmetic mean of the two diagonals, *d1* and *d2* in mm. The hardness values are measured at the cross section of the welded blank by using Vickers micro hardness tester (Make: Omnitech) represented in Fig. 3.11. The measurement is taken at 0.2 mm gap between the two indentations to avoid any possible effects of localised strain hardening because of nearby indentations. Figure 3.12 represents the schematic view of hardness impression with different locations. The hardness variation is observed from BM to BM keeping the FZ at the center. For all the cases the hardness is measured at 300 g load with 16 s dwell time.

Fig. 3.11 Photograph of Vickers micro hardness tester

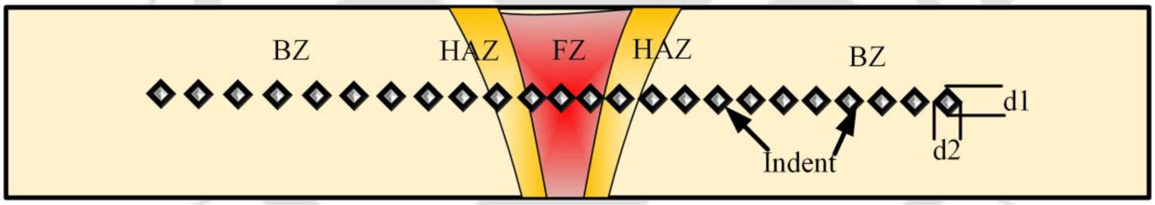

Fig. 3.12 Schematic view of the micro hardness measurement of a welded sample

3.7 Tensile test

Tensile testing is a fundamental method in material science used to assess the mechanical properties of materials under uniaxial loading condition. This test is crucial for understanding how materials respond to forces and predicting their behaviour in various applications. Industries use tensile tests to ensure the quality and consistency of materials, especially in manufacturing processes. Hence, tensile testing is worldwide accepted test method that provides the information about mechanical properties like ultimate tensile strength (UTS), 0.2% yield strength, strain hardening exponent (n-value), strain hardening coefficient (K-value) and percentage of elongation up to fracture. Besides, in welding process, the tensile test plays an important role to make a comparison between the BM and welded blank in their mechanical properties. A hydraulic control universal tensile testing machine (Make: Biss; MEDIAN 250) is used to perform the tensile test which is shown in Fig. 3.13.

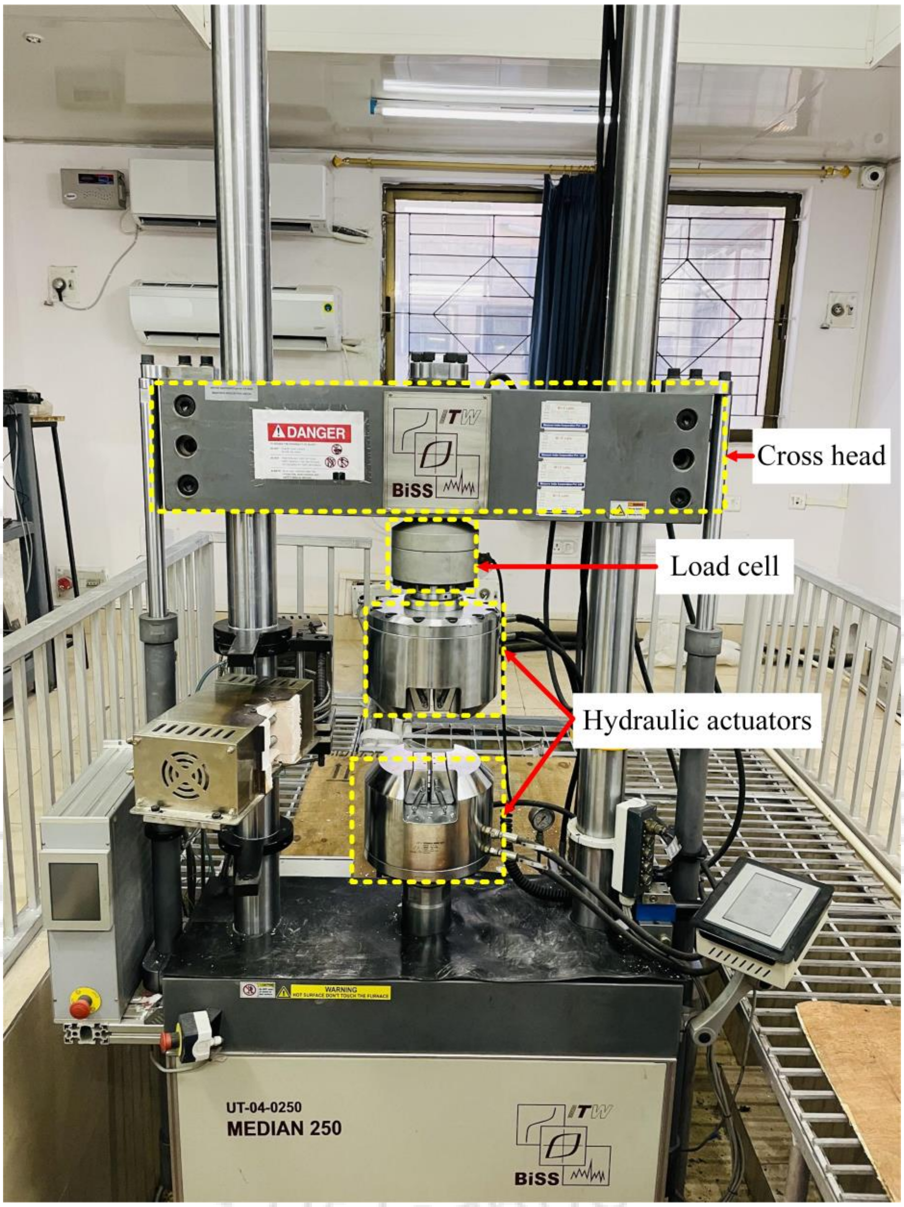

Fig. 3.13 Universal tensile testing machine

A sub size tensile specimen is prepared by following the ASTM E8 (ASTM Committee on Mechanical Testing, 2013) standard, which has 25 mm gauge length and 6 mm width. All dimension details of the tensile specimen are shown in Fig. 3.14. A 25 mm gauge length extensometer is also mounted to measure accurate displacement data within the gauge section. During the tensile test the cross head moves with a constant travel speed of 1 mm/min. The obtained load displacement data from the tensile test is converted into true and engineering stress-strain data to evaluate various mechanical properties.

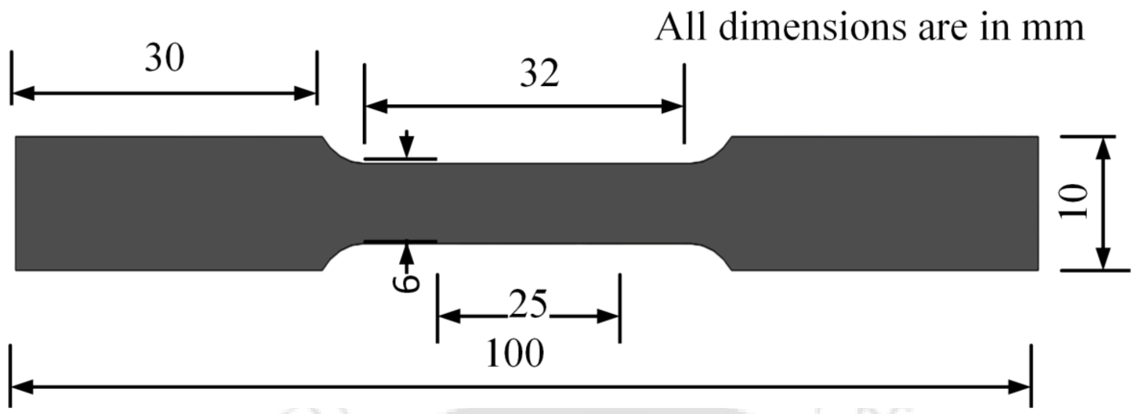

Fig. 3.14 Dimension details of tensile specimen (ASTM E8)

3.8 Formability test

Formability is an important sheet material property use by many industries like automobiles where bulk sheet deformation is required without undergoing any failure. Forming of complex welded parts in various applications are associated with a combination of drawing and stretching operations. Limiting dome height test (LDH) is a well-accepted forming experimental procedure, through which one can understand the formability of sheet material and limit of failure. The FLD is most popular useful tool for the measurement of formability of thin sheet materials. Figure 3.15 represents the schematic of FLD. The primary characteristics of FLD is forming limit curve (FLC). The FLC is the boundary between the uniform deformation and the start of plastic instability or diffuse necking, ultimately leading to failure (Shen et al., 2022). Keeler and Backofen (Keeler, 1961) first gave the concept of right side of FLD and Godwin (Goodwin, 1968) provided the extended FLD i.e., left side of FLD in the year of 1960. The diagram consists of major strain, ε_1, and minor strain, ε_2, obtained from the necking and the fracture point. The regions above and below the FLC are considered as the failure and safe regions, respectively. The higher value of FLC generally refers as higher formability of the blank.

In the current research work a sub-size laboratory scale forming setup is designed and fabricated. The developed setup consists of a hemispherical punch of 30 mm diameter and a 32 mm diameter die opening. A 64 mm diameter draw bead is used to restrict the slip of the blank between the upper die and lower die. The design details of the different parts of the forming setup are represented in Fig. 3.16, 3.17 and 3.18 for the top die, lower die and punch, respectively. The whole setup is attached with a universal tensile testing machine, in which the punch is attached with the stationary cross-head and the die with the blank is mounted with the moveable part of the machine (Fig. 3.19). The LDH test is conducted both in dry and lubricated condition for maximum width specimen.

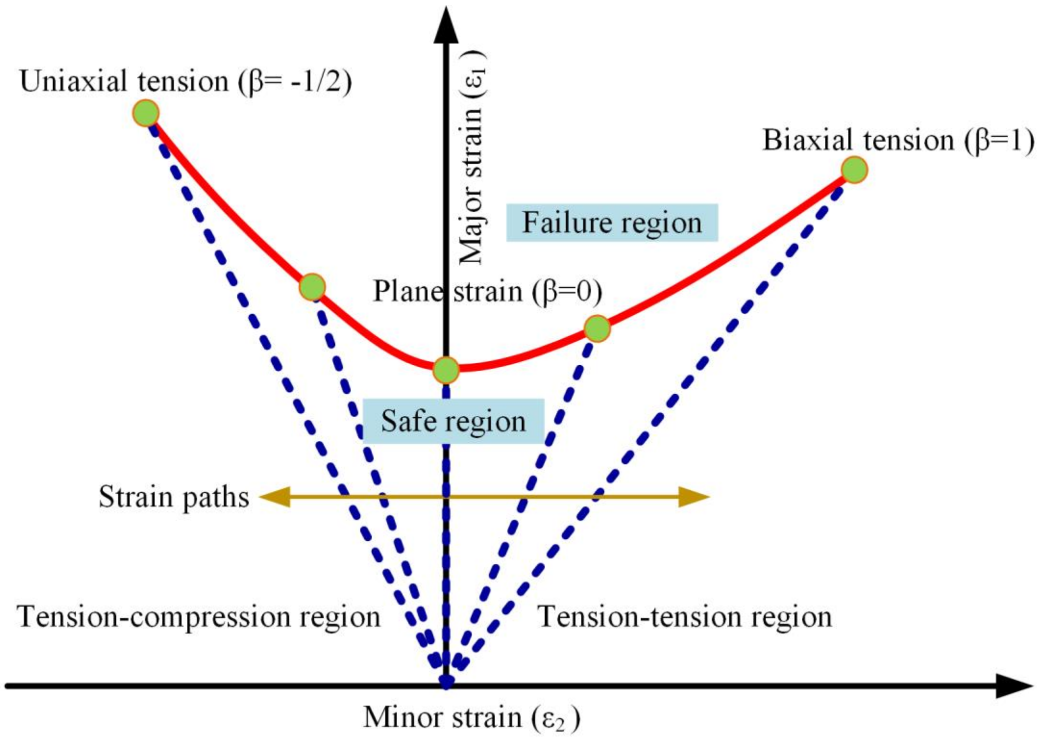

Fig. 3.15 Schematic representation of forming limit diagram

A total of six samples with different width are considered to study the formability from biaxial to uniaxial strain path. Three strain path specimens S1, S2, and S3 are prepared according to Nakazima, and remain three S4, S5, and S6 specimens are prepared by following the Hasek standard to avoid premature failure of blanks at the punch and die interface due to width reduction. Before the test, the specimens are marked with a circular grid of 1.5 mm diameter (d_0) by electro chemical etching technique. Next, the marked specimen is clamped between the upper and lower dies with proper blank holding force by using a nut and bolt fastening system. The workpiece in the die moves upward at a constant cross-head speed against the punch to deform the specimen. The specimen is being deformed till the onset of necking/fracture, which is observed by falling of load monitored by computer control system.

After stretching the specimen, the circular grids deform into ellipses (Fig.3.20). The major (d_1) and minor (d_2) diameters of the ellipse are measured by using a stereo zoom microscope (Make: Nikon; Model: SMZ25) in mm, represented in Fig. 3.21. Thereafter, the true major (ε_1) and minor (ε_2) strains are calculated from the d_1 and d_2 value. These ε_1 and ε_2 values for all strain path specimens in safe and fracture locations are measured and plotted in FLD. The LDH in forming represents the sretchability of the blank, higher LDH implies that the specimen has more formability. The LDH value is measured by using a height gauge (Make: Mitutoyo), represented in Fig. 3.22. The experimental load-displacement (LD) data is plotted for the maximum and minimum width specimens and compared them with the BM for different cases.

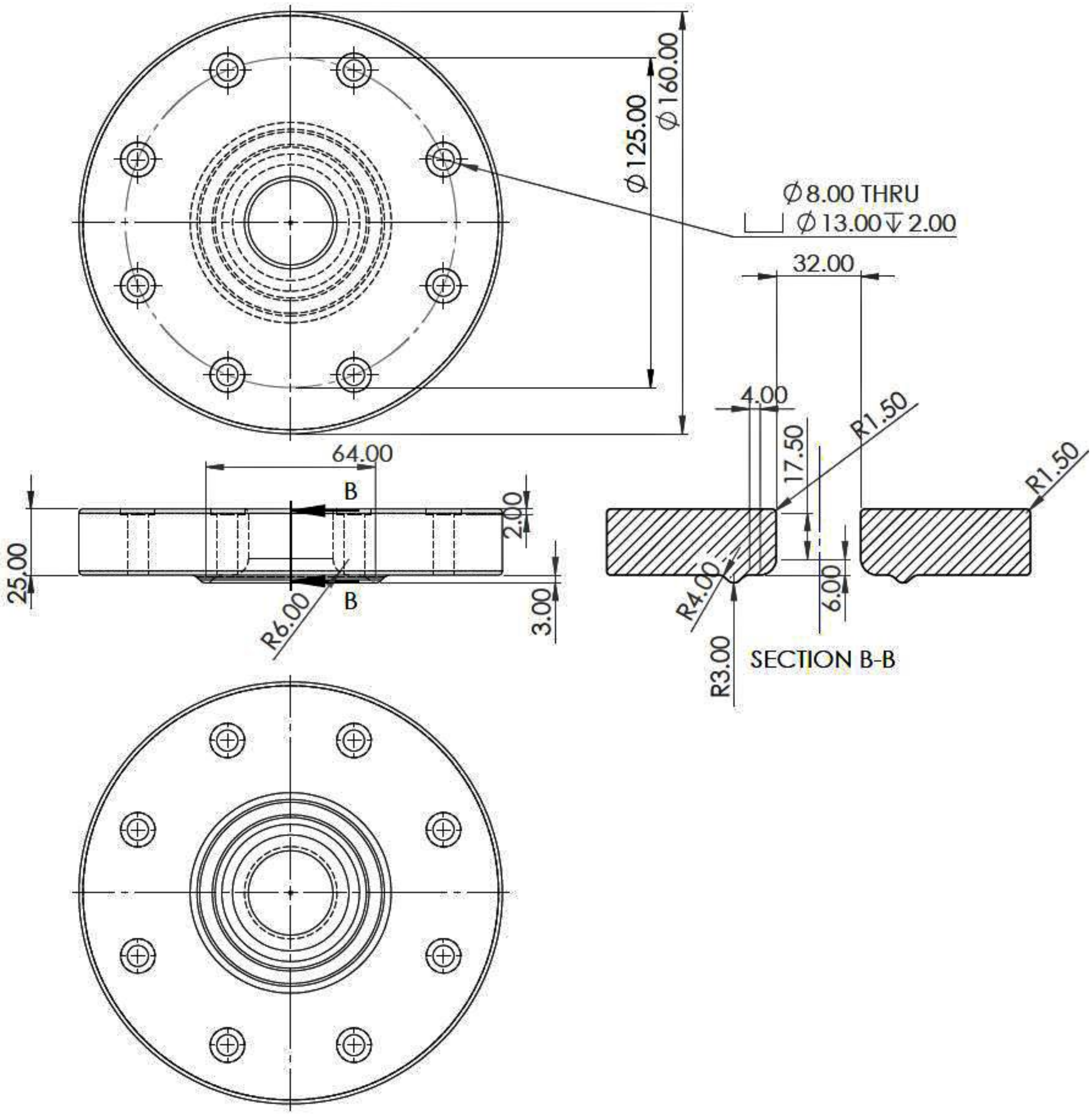

Fig. 3.16 Dimension of the top die (all units are in mm)

The strain distribution profile signifies the distribution of strain on both sides of the maximum height (pole) of the stretched dome. Hence, the variation of strains on both sides of the pole are measured to evaluate the deformation characteristics of the material. The thickness distribution profile is plotted only for the maximum and minimum width specimen.

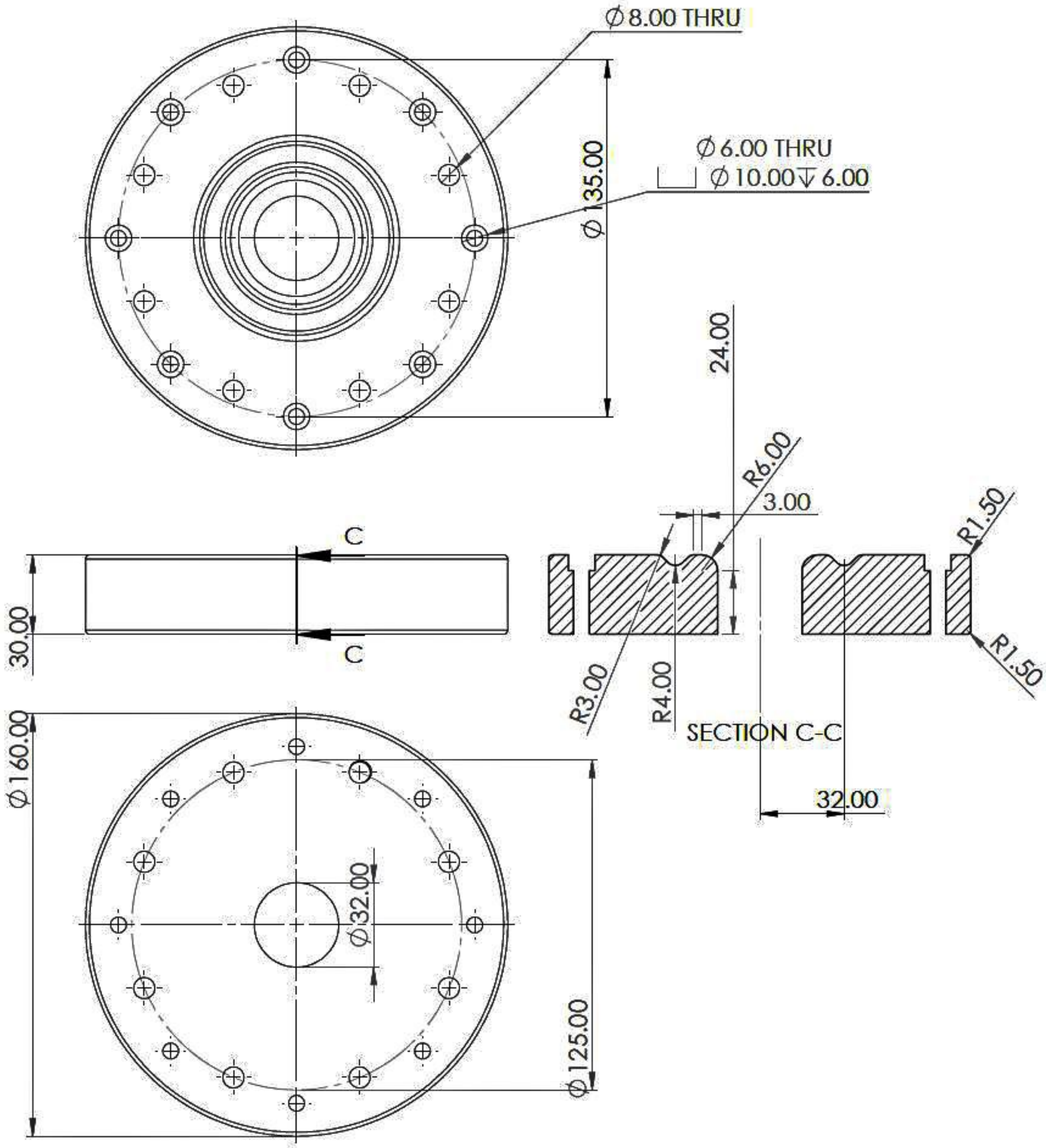

Fig. 3.17 Dimension of the bottom die (all units are in mm)

The thinning behaviour of the stretched dome has significant effect on material utilization, minimizing waste and contributing to cost-effectiveness in large-scale production. Maintaining a uniform thickness distribution contributes to structural integrity, improves product functionality, and promises the production of high-quality components. Thus, the thickness variation on both sides of the pole is measured by stereo zoom microscope. In this regard, the stretched dome spacemen is cut into two symmetric sections transverse to the weld line for the case of welded blanks. However, for the case of BM, the sample are cut along the pole. The thickness distribution profile is studied only for maximum width specimen. A fractography analysis is carried on the fracture surface of the stretched dome to evaluate the mode of failure at the LDH test. A small sample is cut from the fracture location and put in the FESEM to detect different types of morphologies present on the fracture surface.

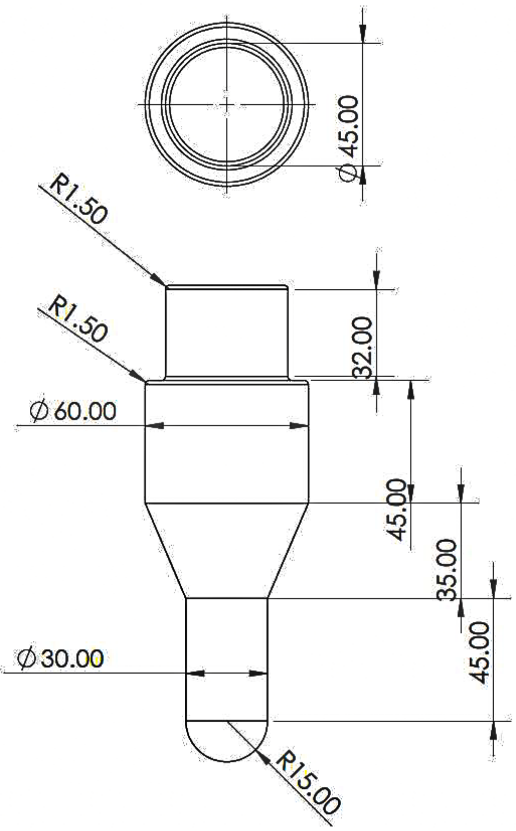

Fig. 3.18 Dimension of the punch (all units are in mm)

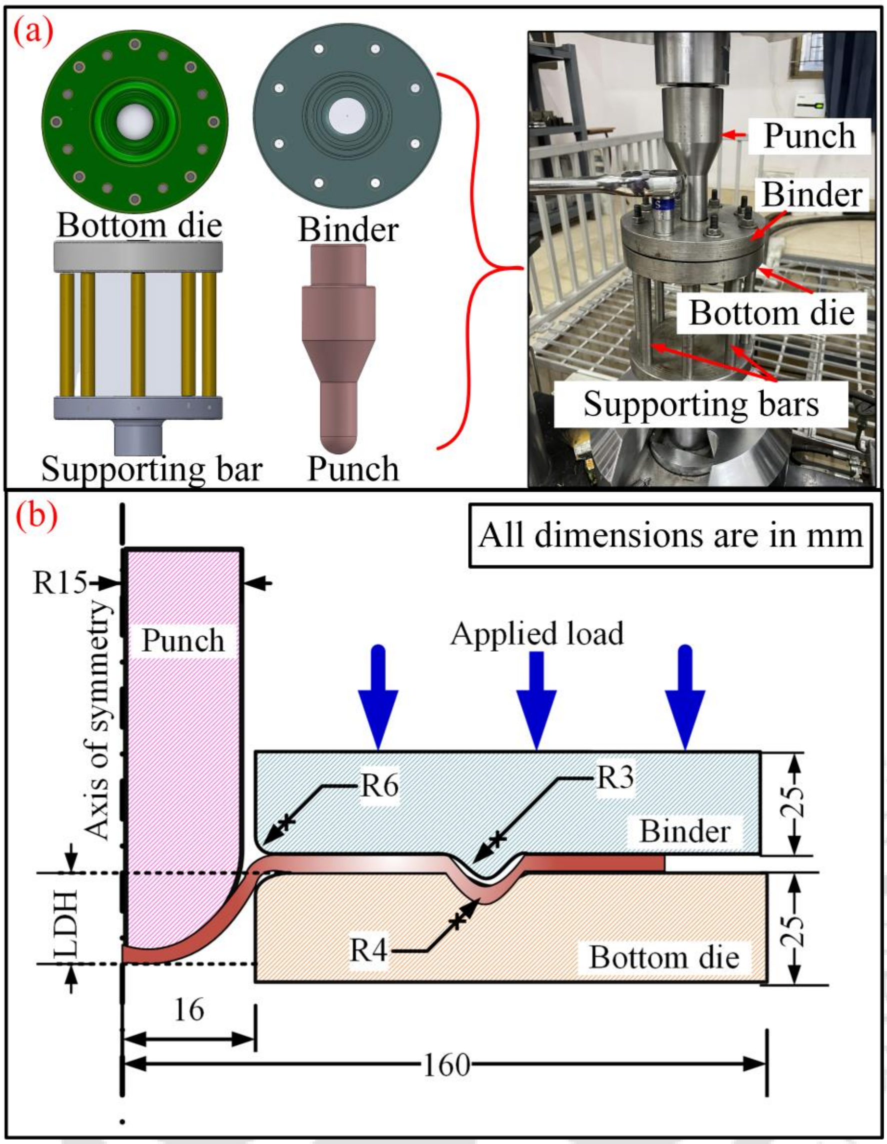

Fig. 3.19 (a) Schematic of limiting dome height setup and (b) tool dimension

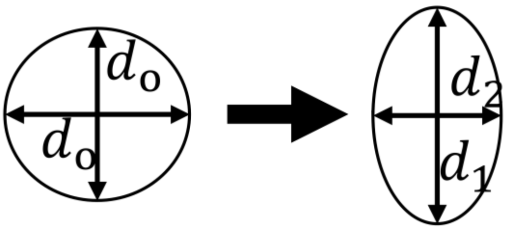

Fig. 3.20 Transformation of grids from initial to final in LDH test

Fig 3.21 Stereo zoom microscope

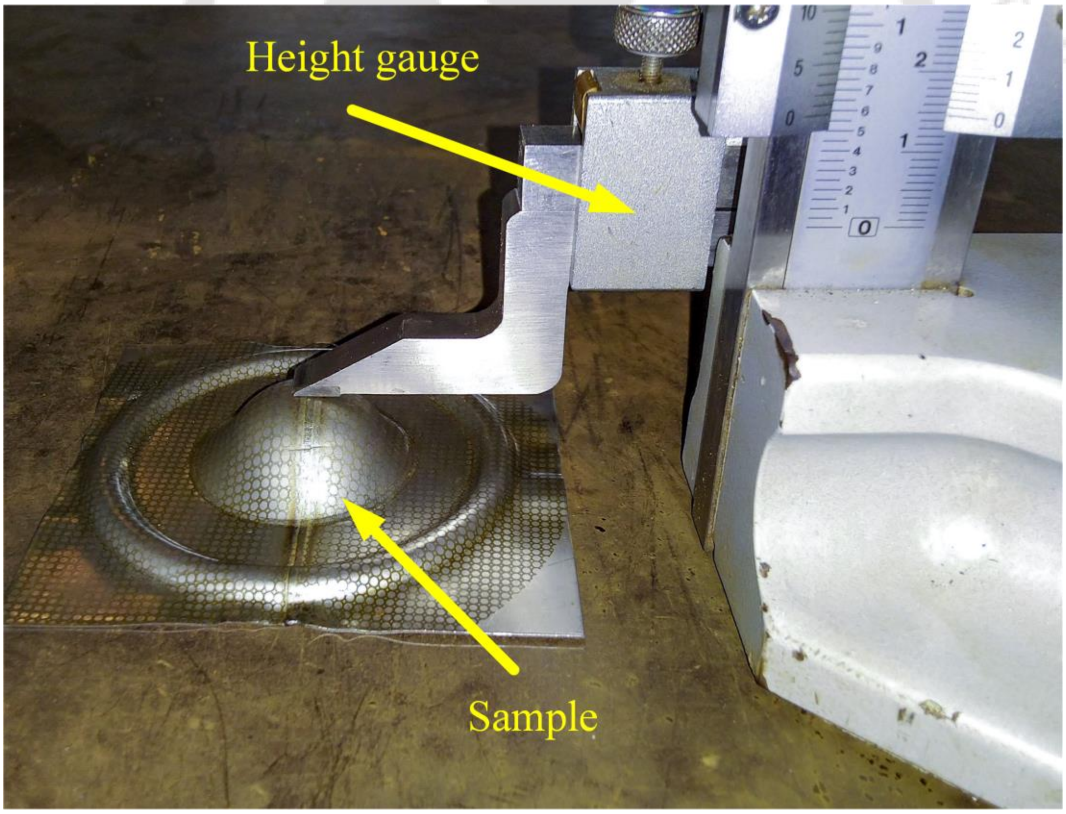

Fig. 3.22 Height gauge for the measurement of LDH

Table 3.6 Details specification of various machines used for testing welded specimens

Machine name	Make & model	Specifications
Dynamic UTM machine	BISS, India MEDIAN 250	▪ Capacity: 250 kN, Actuator displacement: 0 to 80 mm ▪ Hydraulic grips of 0-20 mm flat and 3 to 27 mm round specimen ▪ Tests: Tensile test, compression test, Fatigue, 3 & 4-point bending test, high temperature tensile test ▪ Control mode: Load rate, elongation rate, strain rate, load hold ▪ Testing method: Load mode, displacement mode
Hardness tester	Micro Vickers hardness tester, Omni Tech	▪ Indenter force: 10 gf - 1000 gf ▪ Dwell time: 1-99 Seconds ▪ Indenter velocity: 5 µ/s - 7 µ/s
OM	Leica, Leica ICC50 W	▪ Magnification: 5 X- 100 X ▪ Table movement: 3-axis measuring system ▪ Software: Leica LAS EZ (PC)
FESEM	Zeiss, Sigma	▪ Specimen chamber: 330 mm inner dia, 270 mm height ▪ Specimen weight: Up to 0.5 kg tilted; up to 2 kg not tilted ▪ Movement: X/Y=125 mm, Z=50 mm, T=10º to + 90º, R=360º continuous ▪ Specimen stage: 5-axis motorised cartesian ▪ Chamber detectors: Inlense, SE-2, NEBSD ▪ Magnification: 300 X to 1000 KX
TEM	JEOL, 2100F	▪ Configuration: High resolution (HR) ▪ Resolution: point, 0.23 nm and lattice: 0.1 nm ▪ Acc. Voltage: 200 kV ▪ Electron source emitter: ZrO/W (100) Schottky ▪ 0.5 nA for 1 nm probe ▪ HR diffraction: 333 nm
XRD	Rigaku Technologies, Smartlab	▪ Mode: Powder diffraction, thin film ▪ Technology: Automated high-resolution θ-θ multipurpose X-ray diffractometer (XRD) with Rigaku system Smartlab software ▪ Core attributes: 3 kW sealed X-ray tube, CBO optics, D/teX Ultra 250 silicon strip detector ▪ Core: Photon Max high-flux 9 kW rotating anode X-ray source, in-plane arm (5-axis goniometer), HyPix-3000 high energy resolution 2D HPAD detector, Johansson $K\alpha_1$ optics ▪ Power: 3Ø, 200 V 50/60 Hz, 30 A (sealed tube) or 60 A (rotating anode) ▪ Software: SmartLab Studio II software

Chapter 4

Formability study of micro plasma arc welded 316L stainless steel blanks

4.1 Introduction

Austenitic 316L stainless steel contains interstitial solid solution elements like C and N and substitutional solid solution elements like Mo, Mn, Si etc (Sriba et al., 2018). This alloy is very popular due to its workability in room temperature to elevated temperature and in high corrosive atmosphere (Dai et al., 2022). Thus, it has high demand in different fields like marine structure, gas storage tank, petrochemical industries, food processing industries, nuclear power plant, etc. (Chen et al., 2022). Welded joint of 316L stainless steel alloy sheet has huge scope in those industries, however welding of this alloy sheet is a difficult task due to the formation of welding defects. Moreover, carbide precipitations are formed after the welding at the grain boundaries. With the help of MPAW the formation of such defects can be reduced. Deformable 316L stainless steel welded blank is also used in automobile exhaust system and mechanical bellow manufacturing industries (Subramanian et al., 2021), where high ductile joint is required. The temperature alternation during welding induces microstructural changes in both the FZ and HAZ. These alterations may negatively impact crucial mechanical properties such as formability, tensile strength, hardness, and the alloy structure of the welded blank. Therefore, exploring the relationship between microstructural modifications within different zones of the welded sample and their influence on formability presents significant potential for enhancing the final product quality.

This chapter is mainly focused on the weldability of 316L stainless steel similar joint produced by MPAW process and formability study by LDH test. Total three types of welded blanks, namely T1, T2 and T3 are prepared based on different process parameters level. T1 has minimum current of 9.5 A, 3.5 mm/s speed, 1.5 mm SOD and 1 mm nozzle diameter. T2 has medium current of 10 A, 4 mm/s speed, 1.7 mm SOD and 1.2 mm nozzle diameter. Besides T3 has maximum current of 10.5 A, 4.5 mm/s speed, 1.9 mm SOD and 1.4 mm nozzle diameter. The formability of the MPAWBs is compared with the BM through FLD and strain distribution. Mechanical and metallurgical properties of the welded joints are also examined.

4.2 Microstructural characterization

The detailed microstructure of different regions of the welded specimens are observed by using an optical microscope. The variation of top bead (TB) length, bottom bead (BB) length, and bead height of the welded specimens are shown in Fig. 4.1. It is found that sample T2 has maximum TB and BB lengths of 1.6 mm and 0.97 mm, respectively. Sample T1 is found with minimum TB (1.32 mm) and BB (0.58 mm) lengths. Power density (Watt/m^2) in plasma arc welding can be increased by increasing welding current and welding voltage or reducing the nozzle diameter. A more constricted arc is produced by lowering the nozzle diameter (Park & Hirata, 2017). A 1 mm nozzle diameter is used to prepare the T1 sample, which produces a more constricted arc than the others nozzles. Hence, a narrow bead and higher bead height are formed for the case of T1 specimen.

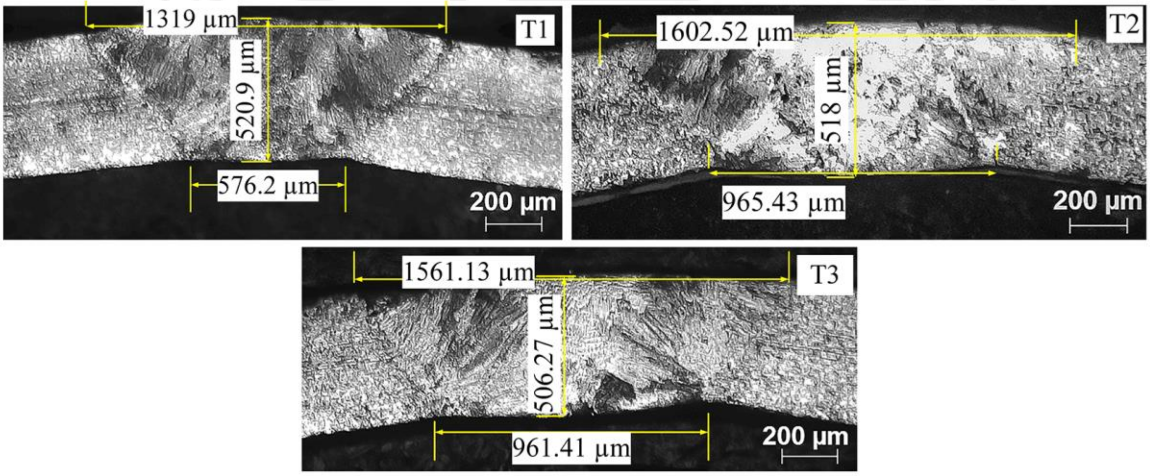

Fig. 4.1 Top and bottom bead length and bead height of welded samples

The microstructural variation of all welded blanks is studied through optical and electron microscope. The macro view of different zones, i.e., BZ, FZ, and HAZ and their corresponding microstructure for specimens T1, T2, and T3 are depicted in Fig. 4.2. Figure 4.2 (a) shows that 316L stainless steel is primarily an austenitic (γ) polycrystalline material with an average grain size of ~12.9 μm. At the BZ, the grain boundaries of austenite and δ-ferrites are also observed. Two different types of microstructure are observed at the FZ, Fig. 4.2 (b) and (c). At the center of the FZ, a skeletal δ-ferrite, and near the HAZ, a columnar dendritic structure is observed. An epitaxial grain growth is at the interphase of FZ and HAZ. The change from a columnar to an equiaxed grain structure in the FZ is a result of the columnar-to-equiaxed transition (CET), which is primarily caused by constitutional undercooling during solidification (Lampman, 1997). At the FZ, some chromium and silicon rich particles are observed through EDX analysis, which is shown in Fig. 4.3 with their locations in FESEM image. These particles are mainly responsible for making the welded joint brittle in nature. Similar microstructural variations are observed in all types of welded specimens. In Fig. 4.2 (d), it can be easily visualized that a narrow zone between the FZ and HAZ is present, referred to as the transition zone. The formation of this zone takes place at the time of the solidification of the molten pool. The tempered HAZ consists of austenite and δ-ferrite. There is no grain growth observed at the HAZ.

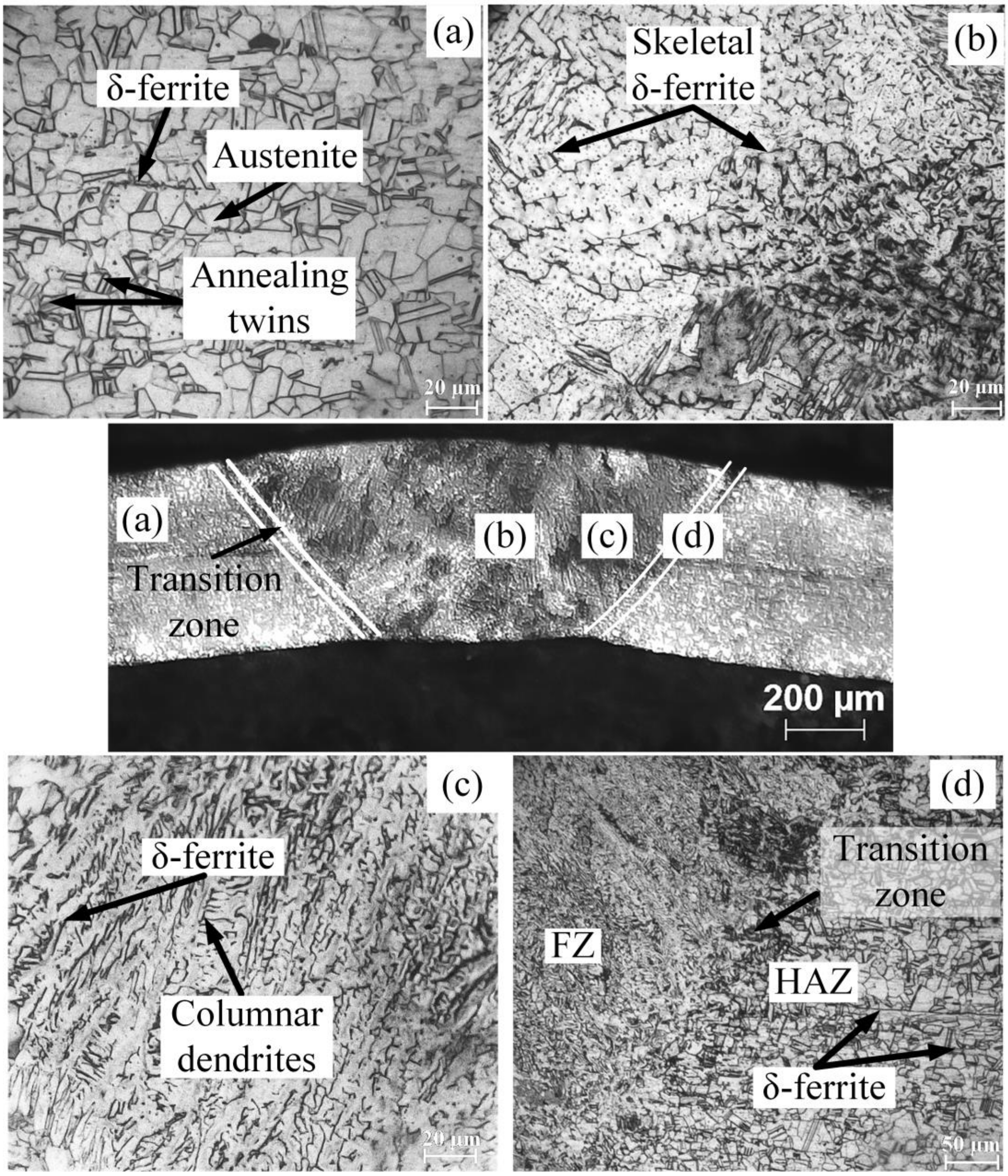

Fig. 4.2 Microstructure of different zones of the sample T1 (a) BZ (b) canter of FZ (c) FZ near to HAZ (d) HAZ

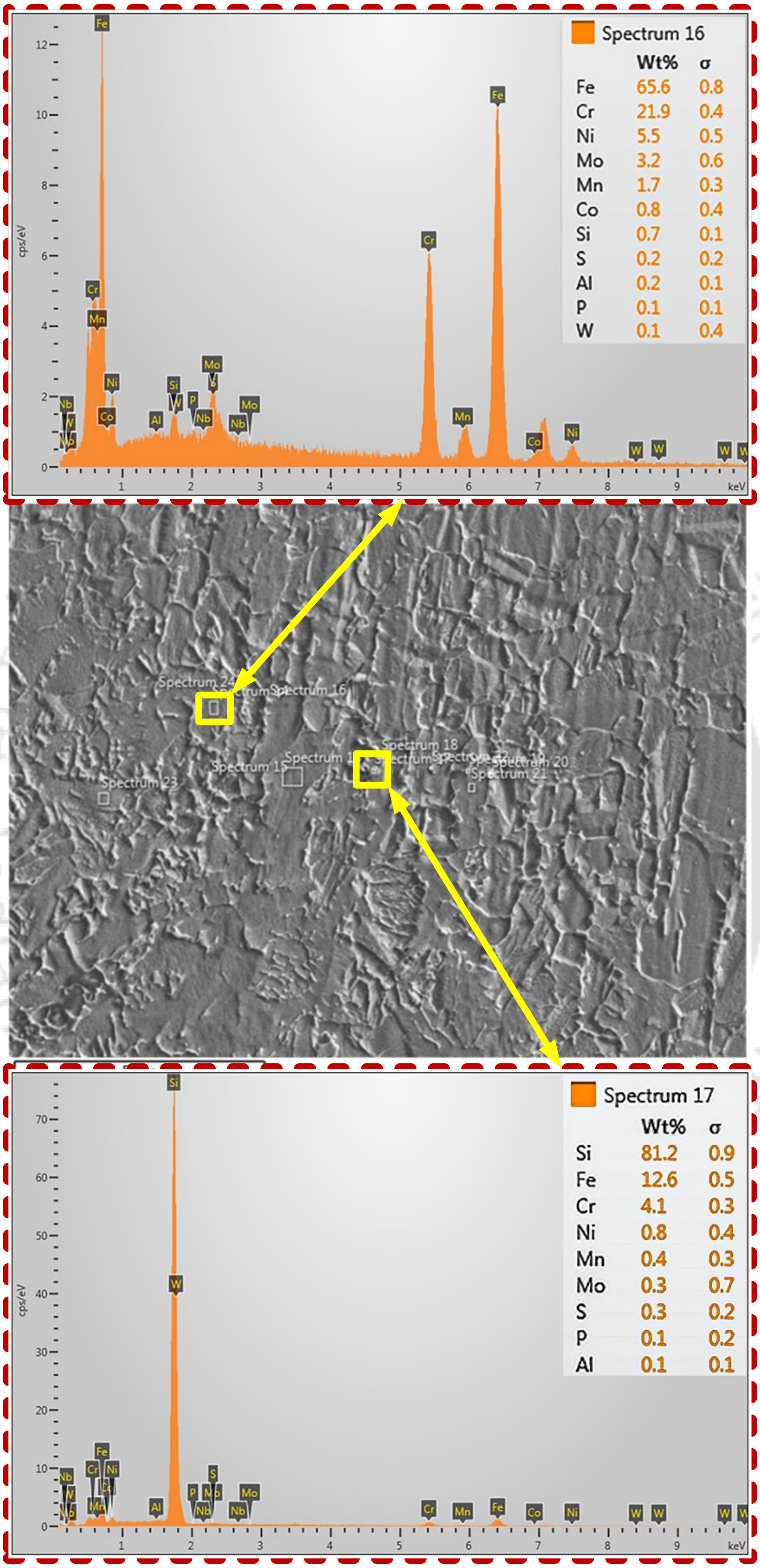

Fig. 4.3 EDX spectrum of a selected FZ region for the sample T1

4.3 XRD analysis

The phases present in the BM and welded joint are explored by XRD analysis, shown in Fig. 4.4. All peak angles (2θ) values are confirmed precisely from standard data (JCPDS Card Nos. 023-0298 and 054-0331 with 3.6 and 2.8075 °A lattice size, respectively). The XRD patterns for the BM and the welded specimens are found with sharp austenite peaks at 43.47°, 50.56°, 74.67°, 90.68°, and 95.92° subsequently (111), (200), (220), (311) and (222) planes, respectively. On the other hand, a few ferrite peaks are also found at 44.62° and 82.18° angles in (110) and (211) planes. The peak intensity of ferrites at the FZ is higher than the ferrite present in the BM. Generally, a small quantity of δ-ferrite is required in stainless steel to reduce the hot cracking during weldment solidification.

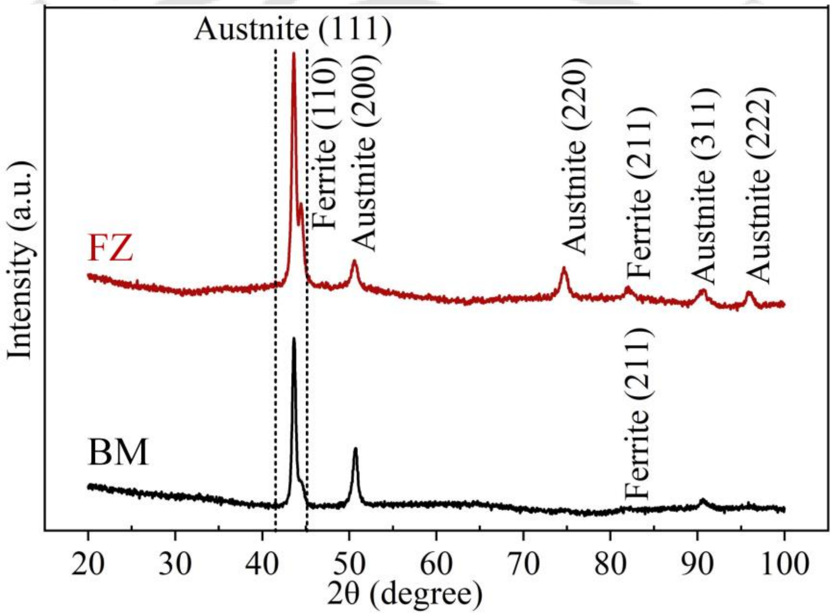

Fig. 4.4 XRD patterns of the fusion zone and base material

Hence, a small peak of δ-ferrite is observed in the BM. However, the intensity of the δ-ferrite present at the FZ is quite higher than that of the BM. The XRD peak intensity depends on stochiometric variation of phases, more periodicity and preferred crystal orientation. Since the thickness of the workpiece is less, and the weld pool size is also narrow, cooling of the weld pool takes place rapidly. During the solidification of the molten weld pool, the primary δ-ferrite gets solidified first, after that, δ to γ transformation takes place (Dadfar et al., 2007). The diffusion process predominates during the δ to γ transformation. The rapid cooling of the FZ leads to insufficient time for the complete phase transformation. Thus, a large amount of δ-ferrite remains at the FZ. This incomplete phase transformation results in the presence of skeletal delta ferrite inside the austenite matrix at the FZ. Hence, the ferrite peak intensity at the FZ is more than the ferrite peak at the BM and similar phenomena was also observed by others (Sabzi et al., 2021; Sriba et al., 2018).

4.4 TEM analysis

The TEM bright field image of different location of the FZ is represented in Fig. 4.5. In which Fig. 4.5 (a) represents the center of the FZ, the δ-ferrite, with planes of (110) and (211), are distributed in austenite matrix of (111), (220), (200), and (311) planes. It agrees the XRD results shown in Fig. 4.4. Bands of grain boundary dislocation are observed in the FZ, shown in Fig. 8(b-c).

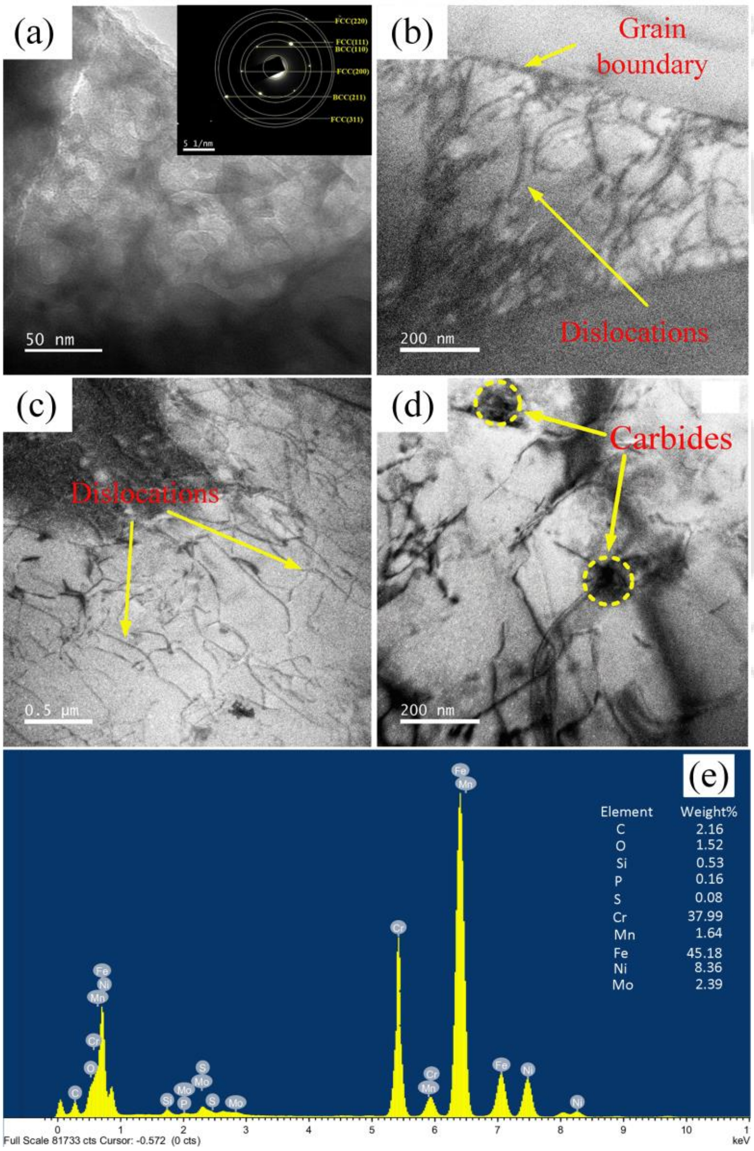

Fig. 4.5 (a) SAED pattern of the fusion zone, (b-c) bright-field image of dislocations, (d) carbide precipitation at the transition zone, and (e) EDX spectrum of carbides

The possible reasons behind the formation of dislocations can be differences in thermal contraction between the δ and γ phases, solid-state transformation from δ to γ, and formation of precipitations in the FZ (Mataya et al., 2003; Sourmail, 2001). Few carbide particles are observed at the transition zone i.e., the interface between the FZ and HAZ, which is shown in Fig. 8 (d). The EDX analysis is conducted by using STEM to confirm carbide precipitation in the transition zone, as shown in Fig. 4.5 (e). It is a metastable chromium carbide ($M_{23}C_6$), which is generally found in austenitic steel during the early stage of precipitation. During welding, the zones that are heated to a temperature near the melting point of the BM, i.e., the solidus temperature of steel, observe the presence of chromium carbides. The presence of such carbides degrades the steel welded joint quality. Due to this reason, strength and ductility of the welded samples get affected.

4.5 Tensile test and hardness analysis

The engineering stress-strain curves for the BM and welded specimens are shown in Fig. 4.6 (a). It is observed that the ultimate tensile strength (UTS) and uniform elongation of the BM are higher than the weld joint (Table 4.1). Heat input at the time of welding plays a key role in getting good weld strength. It has been found (Fig. 4.4) that the quantity of ferrite at the FZ is higher than the BM. The ferrite phase has more hardness as compared with the dominating austenite phase (L. Q. Guo et al., 2013). Therefore, the FZ exhibits more brittle characteristics than the other regions. Moreover, the presence of dendritic structure and carbide phases weaken the weld strength. Hence, all the welded tensile specimens fail at the FZ.

Table 4.1 Mechanical properties of the BM and MPAWBs specimens

Specimen	Yield stress (MPa)	UTS (MPa)	K (MPa)	n-value	Uniform Elongation (%)
BM	293 ± 1	683 ± 2	1400 ± 7	0.39 ± 0.03	57 ± 0.4
T1	304 ± 17	646 ± 5	1239 ± 15	0.34 ± 0.04	44 ± 12
T2	307 ± 8	628 ± 6	1163 ± 25	0.32 ± 0.002	33 ± 8
T3	306 ± 5	620 ± 11	1145 ± 28	0.31 ± 0.009	32 ± 2

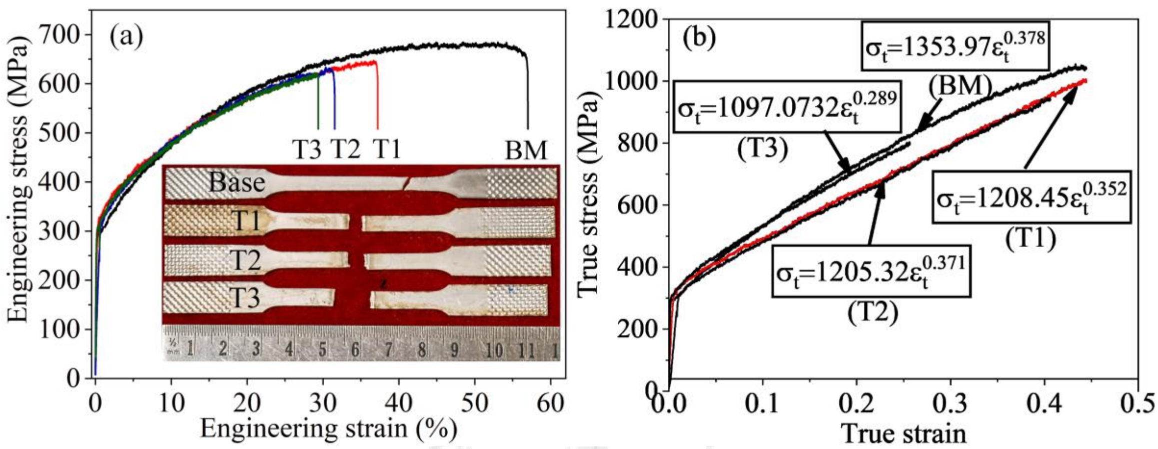

Fig. 4.6 (a) Engineering and (b) true stress-strain plots for the base material and welded specimens

The yield stress (0.2%), UTS, and percentage of elongation up to fracture of the BM and MPAWBs are calculated from the engineering stress-strain plot. The load-displacement data from the tensile test are converted to obtain the true stress (σ_T) and strain (ε_T) values. Thereafter, Hollomon strain hardening curves (Basak et al., 2019) are fitted in-between (0.2%) yield stress and UTS. The hardening equations for the BM and MPAWBs are represented in the true stress-strain diagram, Fig. 4.6 (b). All the mechanical properties of the BM and welded samples are mentioned in Table 4.1. All the welded tensile samples are found to exhibit more than 90% joint efficiency with respect to BM. Among them, specimen T1 provides maximum UTS and elongation. The heat input is less for sample T3 due to the combined effects of higher welding current and speed. Moreover, larger bead width and the lowest bead height is formed due to the higher nozzle diameter. Hence, specimen T3 is found relatively weaker than the other samples.

The microhardness of different zones of the welded specimens are measured and shown in Fig. 4.7. The error bar is measured from the standard deviation of three measured hardness values along the thickness direction. Asymmetrical hardness distribution can be observed. This is due to the variation of microstructure at different regions of the welded joint. The fine dendritic structure has more hardness than the coarser equiaxed microstructure, and this is the main dominating factor for higher hardness at the FZ. Moreover, due to the presence of high dislocation density and ferrite percentage at the FZ, the hardness values also increased sharply (Feng et al., 2015; Sabzi et al., 2022). The FZ hardness of specimens T1, T2, and T3 are 182 ± 2 HV, 186 ± 3 HV, and 184 ± 3 HV, respectively. This variation of hardness might be due to the differences in ferrite percentage present in various samples (Sakthivel et al., 2011).

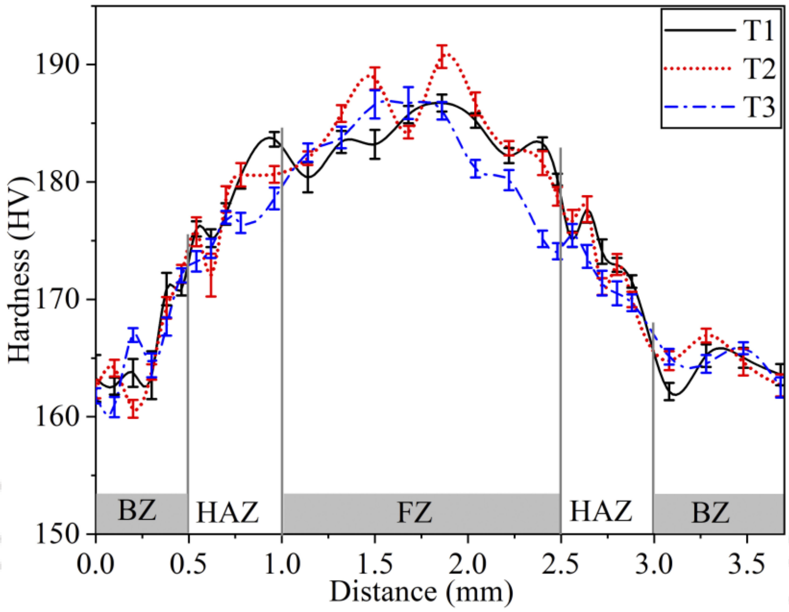

Fig. 4.7 Hardness profile of welded samples

The hardness of HAZ for all the welded specimens is found to be higher than the parent material. Due to the rapid cooling of the FZ, the HAZ does not get sufficient time for grain growth. Moreover, some ferrite particles get deposited in this region because of tempering near melting temperature. Hence, HAZ hardness increases a little more than the BM. Due to the well-defined equiaxed microstructure at the BZ, a minimum hardness of 166 ± 2 HV is observed.

4.6 Formability analysis

4.6.1 Limiting dome height test

The LDH test is carried out for the BM and MPAWBs in dry and lubricated conditions. The stretch forming test is carried out with a slow punch movement rate (1 mm/ min). Figure 4.8 represents the stretch formed samples of BM and welded blanks in dry conditions. It is observed that failure of the stretched welded blanks initiated from the soft transition zone and propagated towards the weld line. This zone is weaker due to the presence of transition lines and precipitations, which are discussed in section 3.1. The formability results of the stretch forming test are represented in Table 4.2. It is found that the LDH of the BM is more significant than that of the welded blanks in both dry and lubricated conditions. This is due to the fact that BM has a higher strain hardening exponent

(n) value and ductility, as discussed in the tensile test. A small reduction of the measured LDH is observed as 4.22%, 9.53%, and 15.03% for the samples T1, T2, and T3, respectively, in dry conditions. This occurs mainly for two reasons, i.e., higher friction between the welded surface and punch interphase and the brittle nature of the FZ. It is found that specimen T1 stretches biaxially more than the other two welded specimens. Because it has a higher n value, ductility, and narrow FZ than the other specimens, on the other hand, specimen T3 shows minimum LDH for its high hardness and less ductility.

Table 4.2 Limiting dome height of the base material and welded specimens

Specimen	Limiting dome height (mm)	
	Dry	Lubricated
Base	15.6 ± 0.55	18.9 ± 0.30
T1	14.9 ± 0.31	15.3 ± 0.25
T2	14.1 ± 0.51	14.9 ± 0.32
T3	13.3 ± 0.80	14.1 ± 0.15

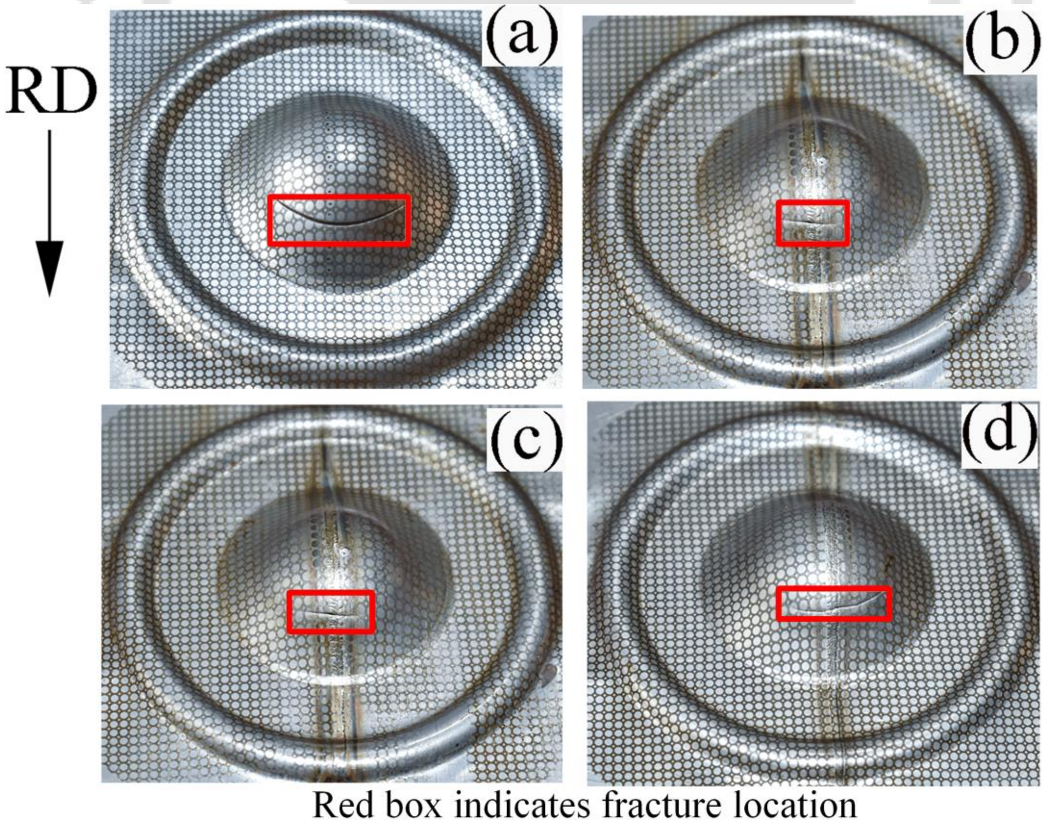

Fig. 4.8 Stretch formed full-size dome of (a) base material (b) T1, (c) T2, (d) T3 samples in dry condition

In lubricated conditions, the LDH of the BM increases about 21.2% compared with the dry state because of less friction between the die and punch. There is a negligible difference in LDH for the welded specimens in dry and lubricated conditions. The samples T1, T2, and T3 are stretched at 1.87%, 5.79%, and 6.17%, respectively, more than the dry condition. This indicates that lubrication does not affect the LDH of welded blanks to a large extent.

The experimental punch load and movement data are plotted in a load-displacement diagram for the BM and MPAWBs of full size (80 mm × 80 mm) specimens in dry and lubricated conditions and shown in Fig. 4.9. In both cases, up to necking, the pressure increases significantly. The maximum load required to deform the specimen of BM is higher as compared with the welded blanks. This happens due to the absence of FZ, which led to an increase in the LDH of the BM. From Fig. 4.9 (a), it is observed that at dry conditions, the load increases equally up to 20.6 kN for the samples T1 and T2. On the other hand, the load increases equally for all the specimens in lubricated conditions. From Fig. 4.9 (b), it is found that there is an increase of maximum load by 16.19%, 15.25%, 9.71%, and 9.28% for the BM, specimens T1, T2, and T3, respectively, in lubricated conditions. The load variation depends on the amount of penetration of the punch into the die. The punch penetration in the lubricated condition is higher than the dry condition because of less friction between the punch and blank. Hence, the load is increased for lubricated conditions.

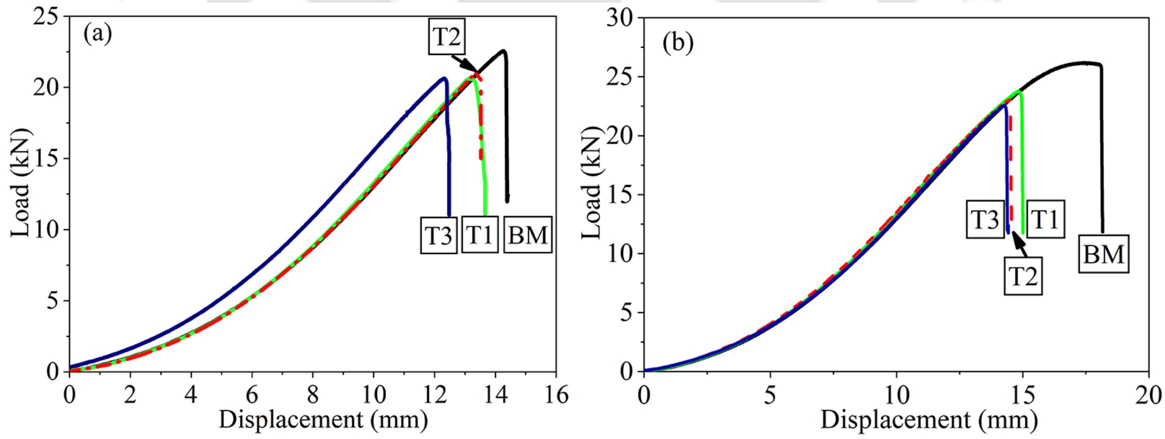

Fig. 4.9 Load variation during stretch forming with respect to punch displacement in (a) dry and (b) lubricated condition of base material and MPAWBs

4.6.2 Forming limit diagram

The experimental FLD is plotted by conducting stretch forming tests with different strain paths in dry and lubricated conditions. Figure 4.10 represents all strain paths stretched specimens of BM and MPAWBs. The true major and minor strains are evaluated from the elongated ellipses in safe, necking, and fractured zones of the BM and welded specimens in the respective strain path. These measured strains are plotted and symbolized with different shapes and colors, as mentioned in Fig. 4.11.

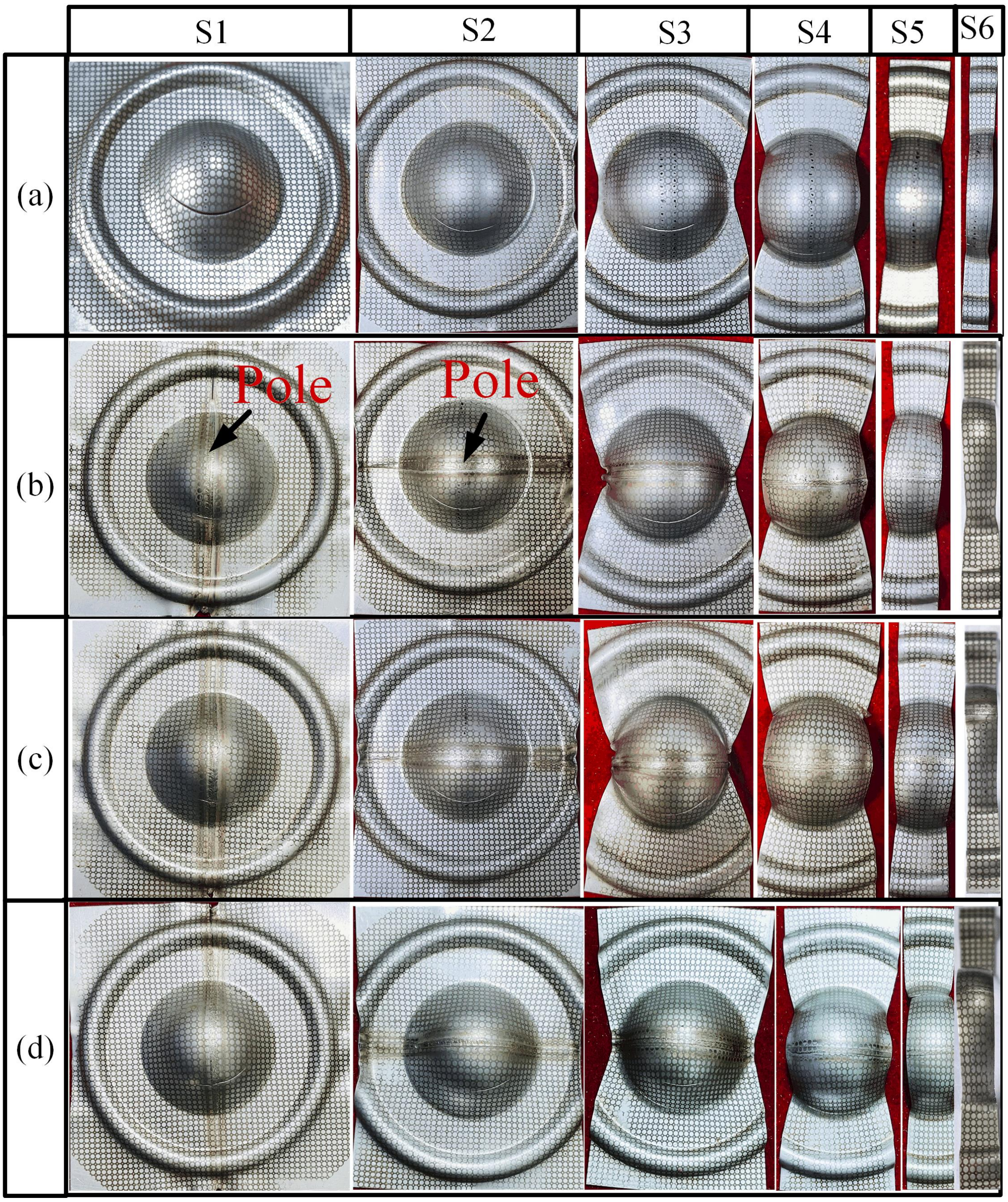

Fig. 4.10 Different strain paths stretched specimens for (a) BM (b) T1 (c) T2 and (d) T3

A distinguished curve is drawn between the necked and fractured points to form the experimental FLD. It can be observed that a series of loading paths from the tension-tension region to the tension-compression region could be achieved using the developed sub-size stretch forming test setup. It is found that strain paths S1, S3, and S6 deform as biaxial, near plane strain, and uniaxial tension, respectively. On the other hand, the 80 mm width specimens (S_L) are stretched near equi-biaxial deformation under lubricated conditions. Table 4.3 depicts the major limiting strain (ε_{ls}) and strain ratio (ε_r) of individual strain paths. From Fig. 4.11 and Table 4.3, it is evaluated that in the tension-tension region of the FLD, the BM owns a maximum of 46.31% major and 27.78% minor limiting strains.

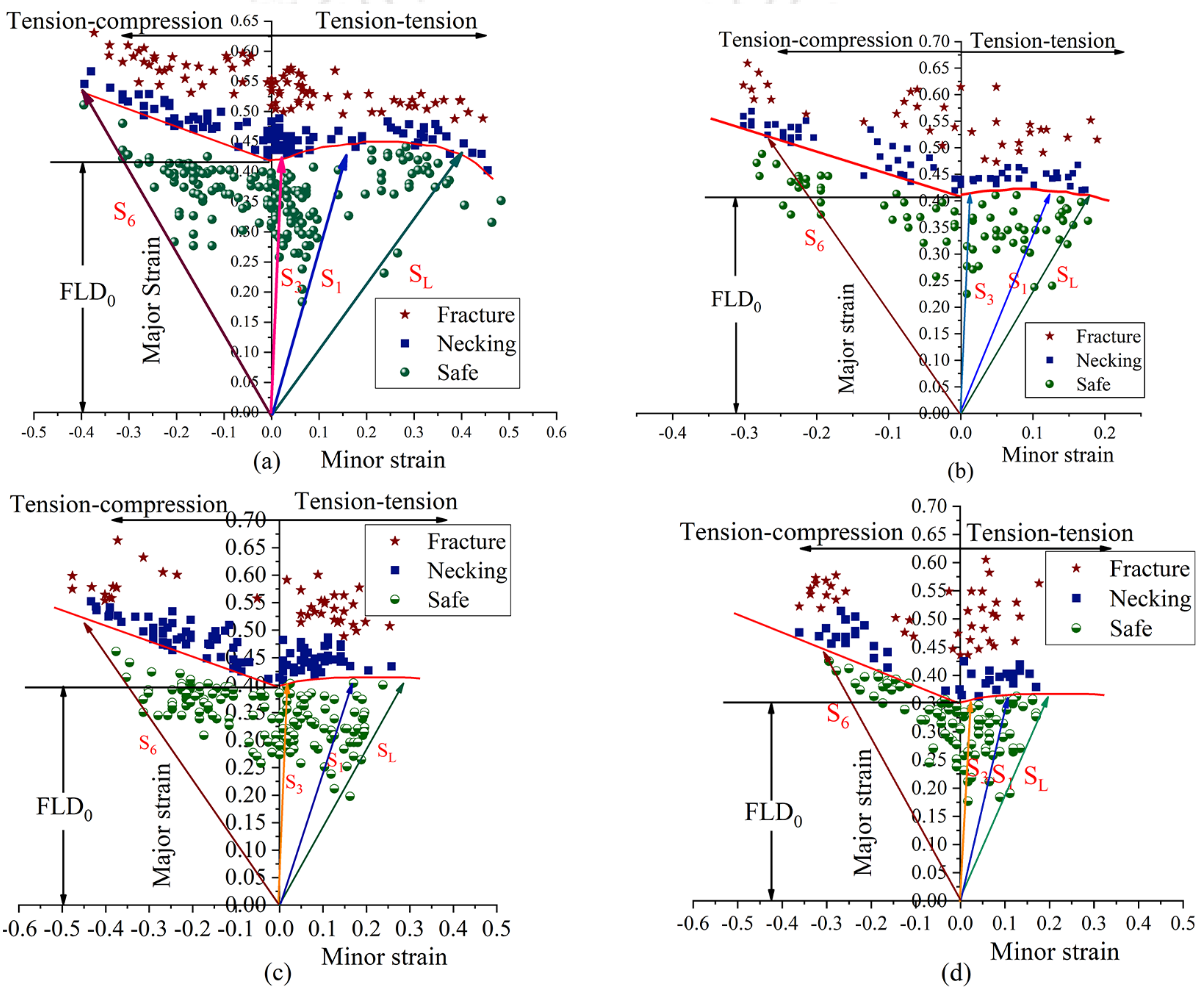

Fig. 4.11 Failure prediction in stretch forming of (a) base material, (b) T1, (c) T2, and (d) T3 specimens by FLD

Specimen T1 is found with 43.93% limiting major and 13.48% minor strains in the tension-tension region. On the other hand, in the same region, the specimens T2 and T3 have 44.51% and 39.19% limiting major and 18.24% and 12.93% minor strains, respectively. This indicates that among all the MPAWBs, specimen T1 has more stretchability than the others welded specimens.

In plane-strain conditions, the BM has a maximum of 42.42% major strain and 0% minor strain. Also, all welded specimens are found with 0% minor strain, and specimen T1 shows a maximum limiting major strain of 40.88% among all the welded specimens in this region. This limiting major strain is indicated as FLD_0, which is the minimum intersection of the forming limit curve with the major principal axis. The FLD_0 is important for the prediction of fracture behavior of cold-formed parts. The *n*-value highly influences the FLD_0, which shifts upward with the increasing *n*-value. Because of this reason, the FLD_0 of BM is found higher than the welded blanks. Specimens T1 and T3 are having maximum and minimum FLD_0, respectively, among the welded samples.

Table 4.3 Limiting major strain and strain ratio in different strain paths

Strain path	Strain condition	Welded specimen							
		BM		T1		T2		T3	
		(ε_r)	ε_{ls} (%)	(ε_r)	ε_{ls} (%)	(ε_r)	ε_{ls} (%)	(ε_r)	ε_{ls} (%)
S1	Tension-	0.60	46.3	0.30	44.9	0.41	44.5	0.3	39.2
S2	tension	0.39	44.3	0.18	43.9	0.22	42.6	0.2	36.9
S3	Plane strain	0.00	42.4	0.0	40.9	0.00	39.9	0.00	34.1
S4	Tension-	-0.13	44.1	-0.21	45.7	-0.21	42.7	-0.10	36.6
S5	compressi	-0.48	49.8	-0.34	47.9	-0.45	46.5	-0.48	41.8
S6	on	-0.55	54.6	-0.51	52.6	-0.61	50.2	-0.49	44.6

It is found that the limiting strain in the tension-compression region is relatively high for the BM and welded specimen as compared with the tension-tension region. On the tension-compression region, the BM has a maximum of 54.6% major strain and strain ratio of -0.55. The welded specimens T1, T2, and T3 are having strain ratio of -0.51, -0.61 and -0.49, respectively, which indicates that all welded specimens have enough drawability.

4.6.3 Strain distribution

The measured logarithmic major and minor strains of the BM and MPAWBs of S1 and S6 strain paths specimens are plotted with distance from the pole to evaluate the strain distribution profile, shown in Fig. 4.12. It is considered that the pole located at zero and right side of the pole is positive, and left side is negative.

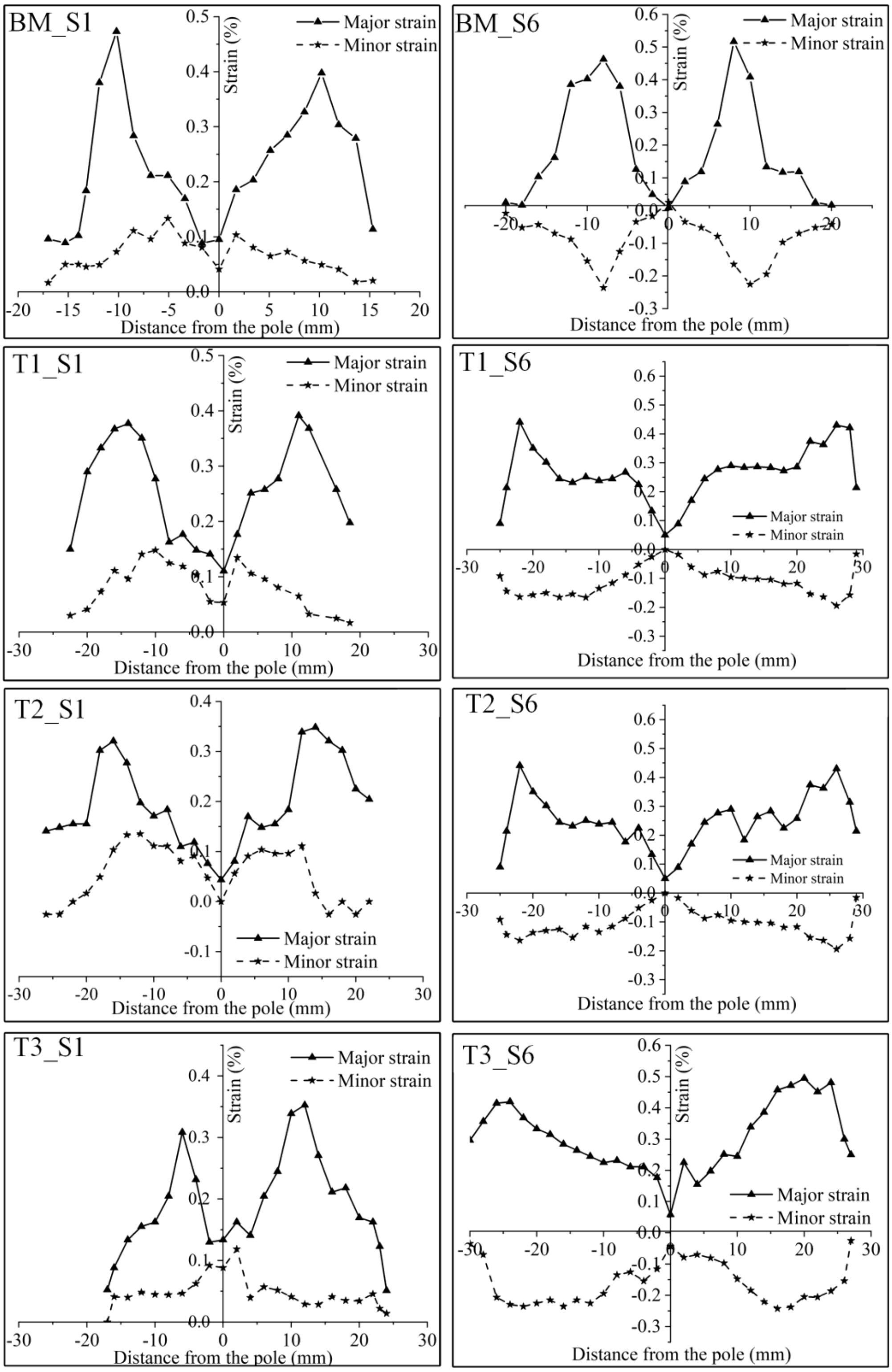

Fig. 4.12 Strain distribution for S1 and S6 of BM and welded specimens

It is observed that strain path S_1 for all the cases deformed biaxially, and grids on both sides of the pole deform equally (Fig. 4.12). Moreover, S_1 specimens break from the center of the weld line, and no fracture points occur on the path of the strain distribution line. Hence, the difference in peak height for S1 of all welded samples is near zero. Due to the same reason, the maximum major strain value is comparatively lower than the LDH test data. A similar pattern of strain distribution is also observed for the case of BM in the S_1 strain path. It can be observed that minimum minor and major strains for S_1 and S_6 are at the pole. On the other hand, maximum major and minor strains are observed far from the pole. The biaxial specimen (S_6) of BM is found with a maximum major strain. In welded samples, T1 and T2 are having maximum and minimum major strain, respectively.

The peak difference between the left hand and right-hand sides of the pole of the tension-compression specimen (S_6) is near zero. The major strain and minor strain of strain path S_6 for all the specimens are above and below the displacement axis, respectively. This indicates that the S_6 strain path samples deform in tension-compression mode. However, it is observed that the BM has a maximum major and maximum negative minor strain in the S_6 strain path. Among all the welded specimens, T1 is found with a maximum major strain.

4.6.4 Fracture surface analysis of the stretched specimen

The fracture surface of the biaxial stretched specimen, tested in dry condition, is investigated to evaluate the failure mechanism. The SEM images of the center of the fracture surface of the BM and specimens T1, T2, and T3, are shown in Fig 4.13. In Fig. 4.13 (a) a large number of regular distributed shallow dimples confirms that the mode of failure in the BM is ductile in nature. Since austenitic 316L stainless steel is a soft, low-hardness material, the fracture occurs relatively slowly following a significant plastic deformation during a stretch forming test. As a result of this, fine cavities and voids like structures are formed (Masoud Sabzi & Dezfuli, 2018b). The MPAWBs are also found with large dimples and voids. The decohesion at the interphase of austenite and ferrite in the FZ occurs due to the difference in plastic properties between austenite and ferrite. As discussed earlier, a large quantity of δ-ferrite at the FZ increases the weld hardness compared with the BM, which is another reason for the failure at the FZ. After the welding, the ferrite to another phase transformation occurs very fast, which breaks the δ-network. As a result, some carbide precipitates at the austenite-ferrite interphase as an intermetallic compound, loosening the joint strength and leading to joint failure. However, lots of voids and dimples are witnessed on the fracture surface of MPAWBs, which indicates that the failure mode of all types of welded MPAWBs is ductile in nature.

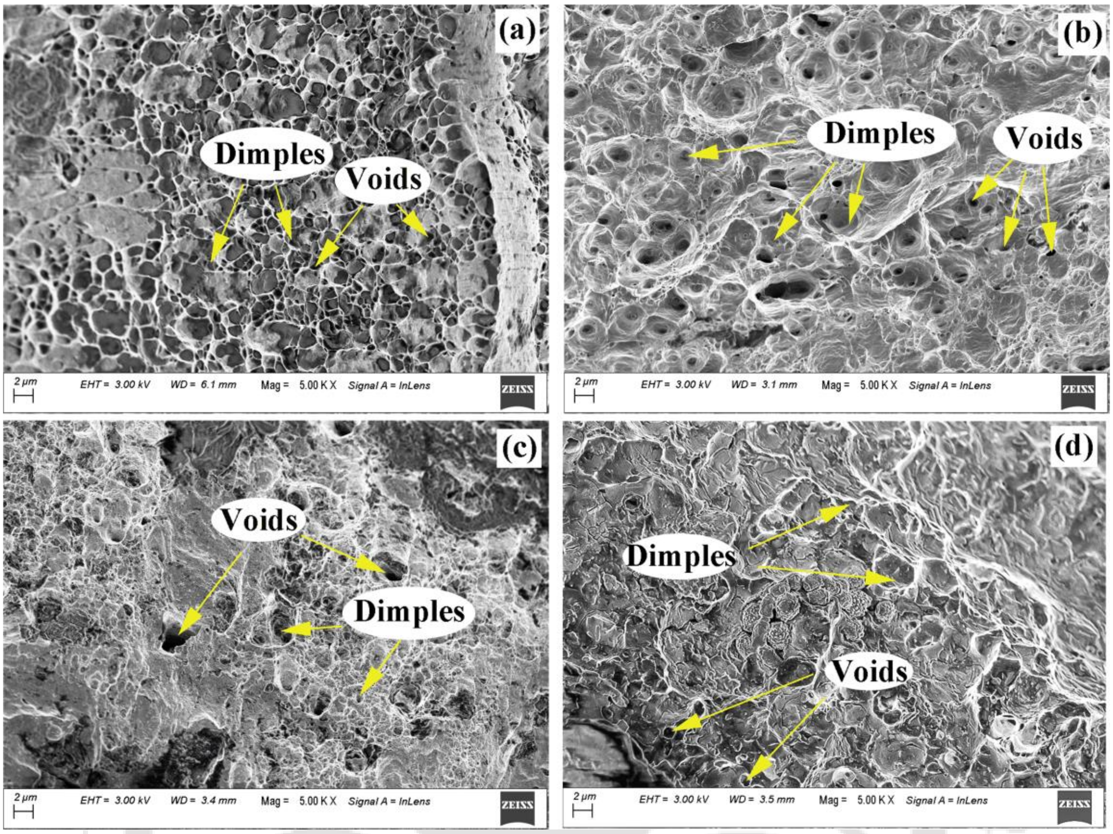

Fig. 4.13 SEM images of the fracture surfaces of (a) base material, (b) T1, (c) T2, and (d) T3 specimens

4.7 Summary

Three different types of welded blanks are prepared successfully by using a different combination of parameter settings in MPAW process. The FZ, BM, and HAZ of the welded samples are discussed through microstructural analysis to correlate the forming behaviour of the welded joint. The BM consists of well oriented coarse grain structure upon which δ-ferrite and annealing twins are distributed. Whereas, the FZ consists of two different types of microstructure, namely, skeletal δ-ferrite at the center and columnar dendritic structure near the transition zone. The XRD study reveals that the quantity of ferrite at the FZ is higher than that of the BM. Besides, TEM analysis confirms that the FZ and transition zone consist of austenite, ferrite, and some secondary phases of Cr and Si carbides. These phases are mainly responsible for embrittling the FZ. More than 90% joint efficiency is achieved in all the MPAWBs. Failure of the welded tensile samples takes place from the FZ. The hardness of the FZ is highest, and HAZ hardness is comparatively larger than the BZ. The limiting dome height of the welded blanks is compared with the parent material in dry and lubricating conditions. It is found that the LDH of the BM is larger than that of the welded specimens in both the conditions. Failure of the welded biaxial specimens occurs across the weld line due to higher friction between the punch and welded surfaces. FLD is developed successfully by using an inhouse developed sub-size micro forming setup. All welded specimens own good ductility, particularly T1 specimen possesses better formability. A uniform strain distribution profile is observed for the S1 and S6 strain path specimens on both sides of the pole. BM shows a higher peak than the welded specimen for both the strain paths. Many dimples and micro voids are found on the fracture surface of the biaxial stretched samples, which evidence ductile failure mode.

Chapter 5

Mechanical behavior of solution-treated micro plasma arc welded Inconel 625 blank

5.1 Introduction

Nickel based super alloy Inconel 625 is mostly used in gas turbine, aerospace, petrochemical and marine industries due to its excellent corrosion resistivity and high performance at elevated temperature (Y. L. Hu et al., 2020). It exhibits a favorable mixture of yield strength, tensile strength, creep resistance, and robust resistance to high-temperature corrosion when subjected to prolonged exposure in harsh environments (Xu et al., 2013). These mechanical properties of Inconel 625 are mainly influenced by presence of alloying elements like niobium, molybdenum in the nickel primary matrix. Besides this alloy has excellent weldability and fabricability, thus it gains major attraction in different industries (Ramkumar et al., 2021). The main challenging tasks encounter in welding of Inconel 625 are thermal cracking, loss of ductility owing to the formation of laves phase and carbide precipitation. Ageing or ST is generally recommended for Inconel 625 based on application, whether high strength or ductility is required. It is observed by author Marchese et al. (Marchese et al., 2018) that due to ageing the strength of the Inconel 625 improved drastically and reduced the total elongation significantly. Besides, due to ST the ductility of this alloy improved in large extent because of dissolution of dendritic structures.

This chapter is concentrated on the improvement of formability of Inconel 625 MPAWBs after the ST. In this regard welded samples are solution treated at 1100 ºC for 1 Hr. A detailed metallurgical analysis is carried out to understand the effect of solution treatment on the formability of the welded blanks.

5.2 Effect of solution treatment on the microstructural variation

Figure 5.1 shows the FESEM image of the as-received and solution treated BM microstructure. The as-received BM (Fig. 5.1 (a)) exhibits equiaxed grains with a minimum size of approximately 36.0 µm, a maximum size of around 93.22 µm, and an average size of approximately 60.7 µm. Additionally, some annealing twins are evident, this may be due to prior hot rolling operations. On the other hand, due to ST, a grain coarsen is observed in the solution treated BM sample. The average grain size of ST sample (Fig. 5.1 (b)) is 71.4 μm with maximum size of approximately 117.9 μm.

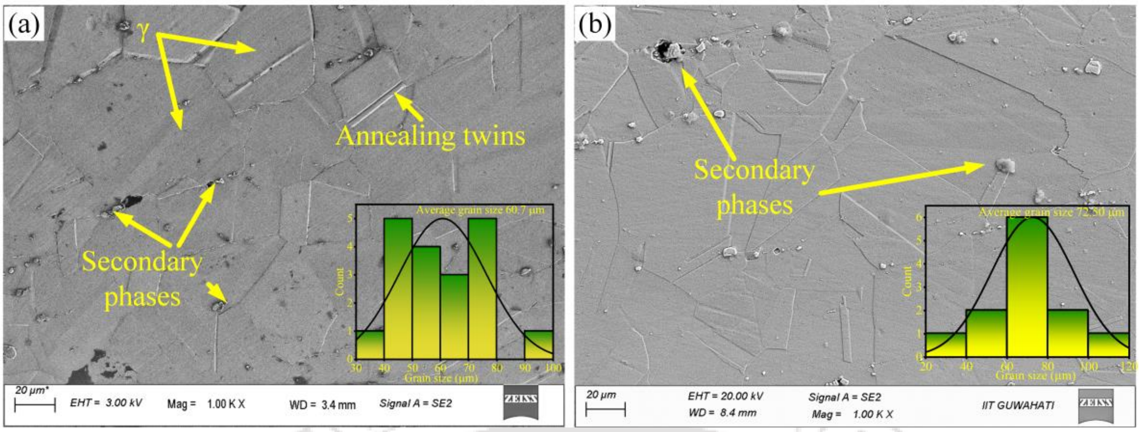

Fig. 5.1 Microstructure of (a) as received BM and (b) solution treated BM

The Inconel 625 is mainly composed of nickel-based austenite (γ) matrix in which some secondary phases like Nb rich Ni_3Nb (γ") and blocky carbide are distributed. Which is responsible for good mechanical properties in different working temperature. An EDX point analysis and mapping are carried out to evaluate the elements of the secondary phases, represented in Fig. 5.2. The EDX analysis confirms that the main constituent element of these secondary phases is Nb. During the ST, these phases tend to dissolve and get elongated. However, complete melting of these phases is very difficult. Thus, after the ST, few of these secondary phases remain in the solution treated BM.

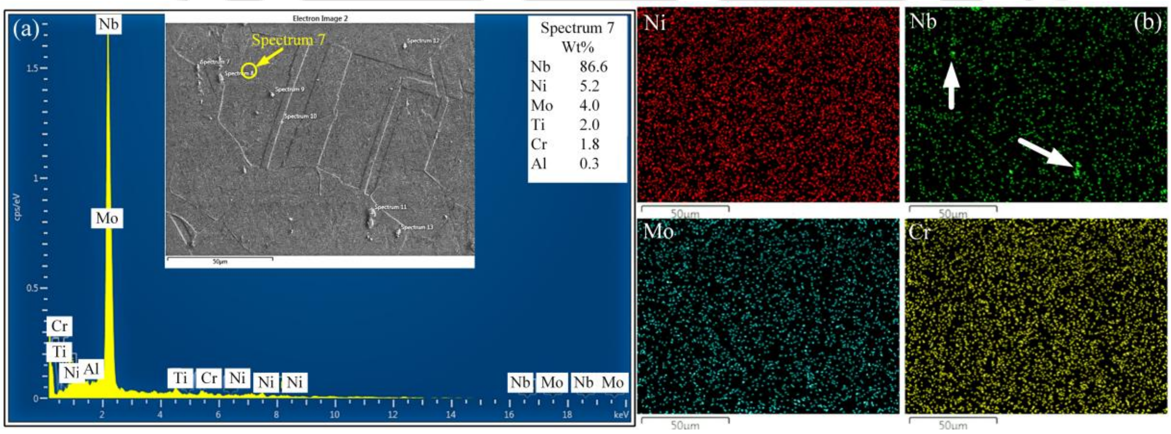

Fig. 5.2 EDX (a) point analysis and (b) mapping of the Inconel 625 BM

Figure 5.3 presents a microscopic view of the weld cross-section, highlighting distinct regions within the FZ, designated as FZ center, FZ near the HAZ, and HAZ, labeled as A, B, and C, respectively. The entire FZ exhibits dendritic structure. Notably, the center of FZ, *i.e*, zone A, is found to have an equiaxed cellular dendritic structure, whereas zone B displays an elongated columnar dendritic structure. An image analysis is carried out to quantify the areas of dendritic grain for the zones A and B, shown in Fig. 5.4. The average grain area of zone A is 29.9 μm^2 with a maximum of 165.44 μm^2. However, zone B is found with an average of 32.36 μm^2 and a maximum of 247.01 μm^2 grains. In this zone, two distinct types of microstructure are observed, i.e., the long identical growth direction grains and fine alternately appeared grains. The formation of different dendritic morphology in the FZ of Inconel 625 is influenced by several parameters like, heat flow and cooling direction, different types of constituent alloying elements and types of welding process (Badiger et al., 2021). The FCC nickel has less diffusion rate with the substitutional alloyoing elements like Nb and Mo (Kourdani & Derakhshandeh-Haghighi, 2018), specially when a fastest cooling is taken plase like welding operation. As a result of this severe microsegregation occurs during the welding of Inconel 625 and produces different types of dendritic microstructures and phases. These microstructures and phases sometimes help for better mechanical properties namely, toughness and strength. However, the columnar grains may have anisotropic properties along their growth direction, which can affect the joint strength and ductility.

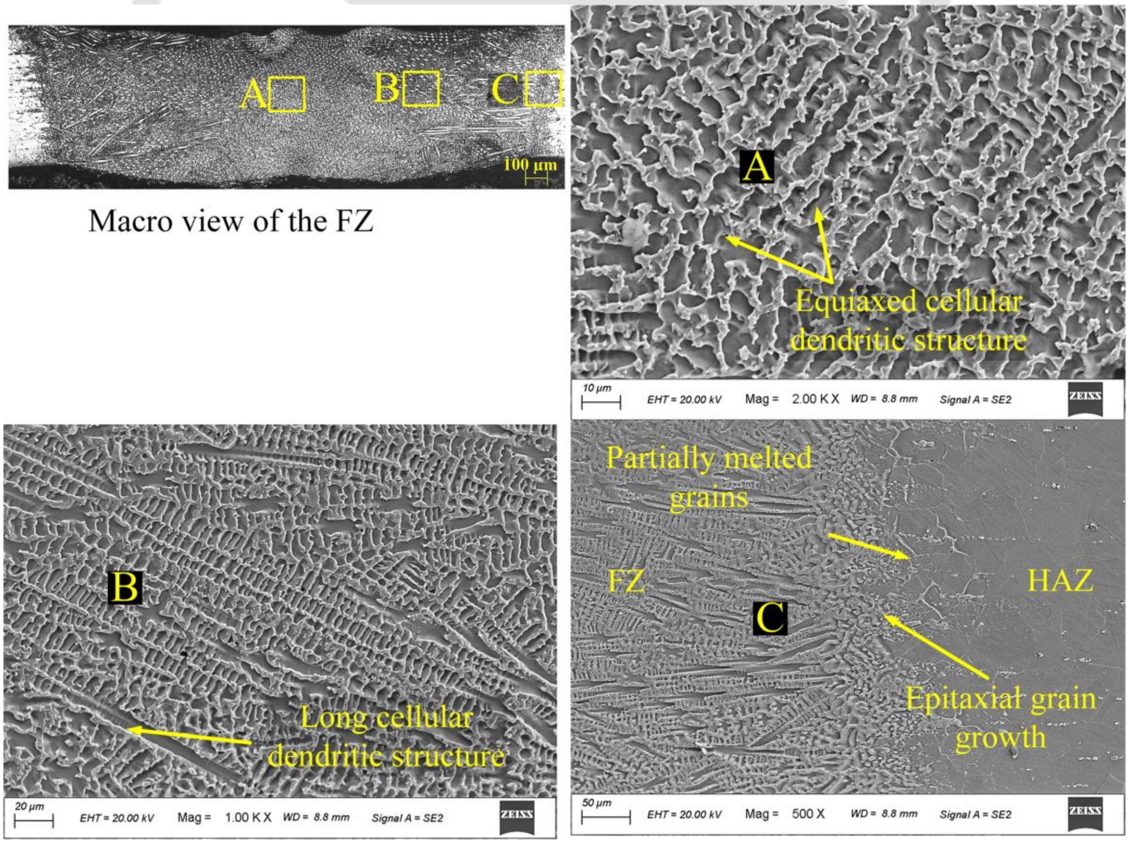

Fig. 5.3 Fusion zone microstructure of the welded blank

The zone C represents the microstructure of the interface of FZ and HAZ. An epitaxial type gain growth is observed in the direction of the FZ to the HAZ. However, no grain growth is occured at the HAZ due to constricted heat input at the time of MPAW. Moreover, it is already mentioned that the as-received BM has large grains, and this is another reason for no grain enlargement at the HAZ (DuPont et al., 2011). During the MPAW, the HAZ experiences a steep temperature gradient from the high-temperature weld pool to the relatively cooler BM. This temperature gradient can result in localized melting of some grains while adjacent grains remain solid. As a result of this some partially melted grains are found adjacent to the FZ.

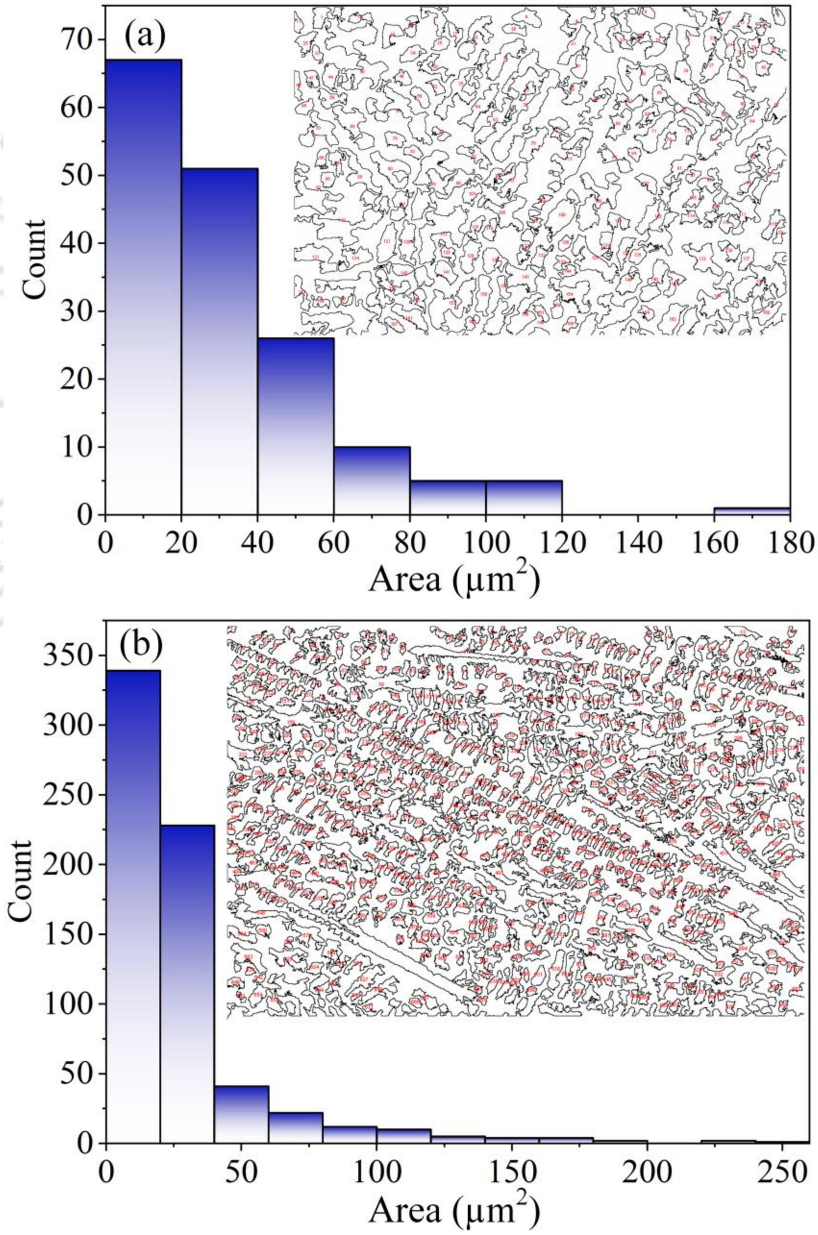

Fig. 5.4 Distribution of grain areas at the (a) center of FZ and (b) FZ near to the HAZ

Some secondary precipitates are found distributed over the grains and grain boundaries in the FZ microstructure, enlarge view of these phases are shown in Fig. 5.5. With the help of EDX point analysis (Table 5.1) and TEM analysis (Fig. 5.6), it is confirmed that the precipitates are carbides and laves phase. The formation of secondary phases is predicted by the pseudo ternary equilibrium phase diagram of Inconel 625, presented in Fig. 5.7. The C and Nb ratio (C/Nb) influence the formation of these phases, the higher ratio of C/Nb produces γ + NbC phases, indicated in Path I. On the other hand, low C/Nb ratio, indicated in path III, leads to the formation of γ + Laves without any NbC. However, in the present investigation, the FZ microstructure consists with the combination of γ + Laves + NbC phases (Floreen et al., 1994). Which indicates that the trend of solidification followed the path II.

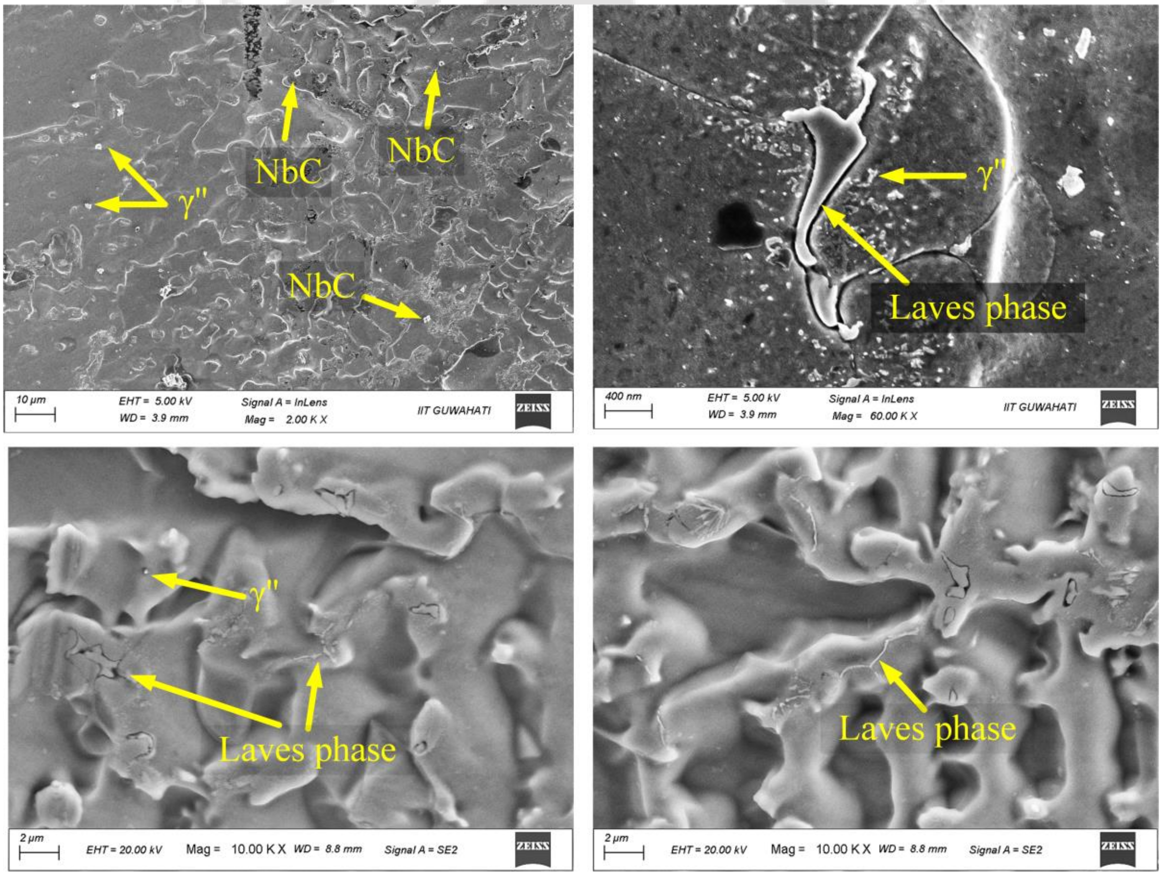

Fig. 5.5 Different types of secondary phases at the FZ microstructure

Table 5.1 Chemical composition of secondary phases in the FZ as welded Inconel 625 sample

Phases	Nb	Mo	Ti	Cr	Fe	Ni
NbC	80.0	3.8	4.6	3.8	-	7.4
Laves	26.8	12.3	0.9	18.5	3.5	37.8

It is observed from Fig. 5.6 (a) that the Laves phase has hexagonal closed packed structure with lattice parameter: a=b=0.20 nm, c=0.23 nm and c/a=1.15. The presence of carbides and Laves phase can lead to reduce ductility and increase hardness of the FZ. The Laves phase can also generate anisotropy in mechanical properties (Hu et al., 2021). The crack initiation and propagation can occur form the Laves phase boundaries, leading to premature failure.

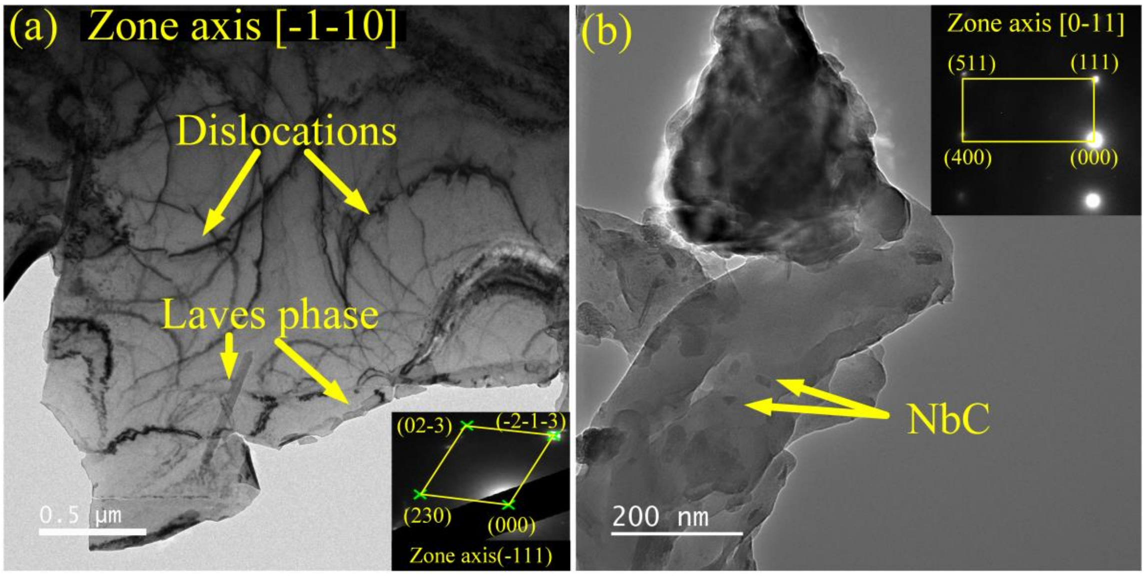

Fig. 5.6 TEM bright field image of as welded Inconel 625 sample (a) Laves phase and (b) NbC

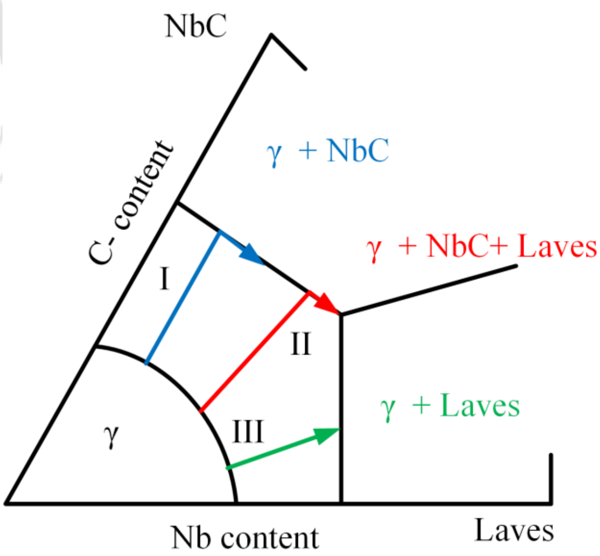

Fig. 5.7 Schematic view of pseudo ternary phase diagram of Inconel 625

Figure 5.8 represents FESEM images of the FZ after ST at 1100 ºC with holding time of 1 h. A significant microstructural variation is observed at the FZ after the ST. Due the ST the existing dendritic structure of the as-welded sample completely dissolves and produces a large equiaxed grains throughout the FZ. However, some secondary phases are also found distributed over the grains. The EDX analysis (Fig. 5.9) revels that the phases are enriched with high percentage of Nb and Ni. The composition analysis and TEM analysis confirm that the phases are Laves and MC type carbides. Due to the ST at 1100 ºC, the Laves phase gets dissolute in the γ-matrix. Consequently, the volume of Laves phase reduces after the ST. However, complete dissolution of Laves phase at this temperature is not possible, thus some small granular like Laves phases are found in scatter manner on the grains and grain boundaries after the ST, a similar trend was also observed by Hu et al. (Mostafaei et al., 2016). With increasing solution temperature, the Laves phases reduces and elongation improves but the strength of the welded blank reduces drastically due to the dissolution of carbides and grain coarsening (Sukumaran et al., 2017).

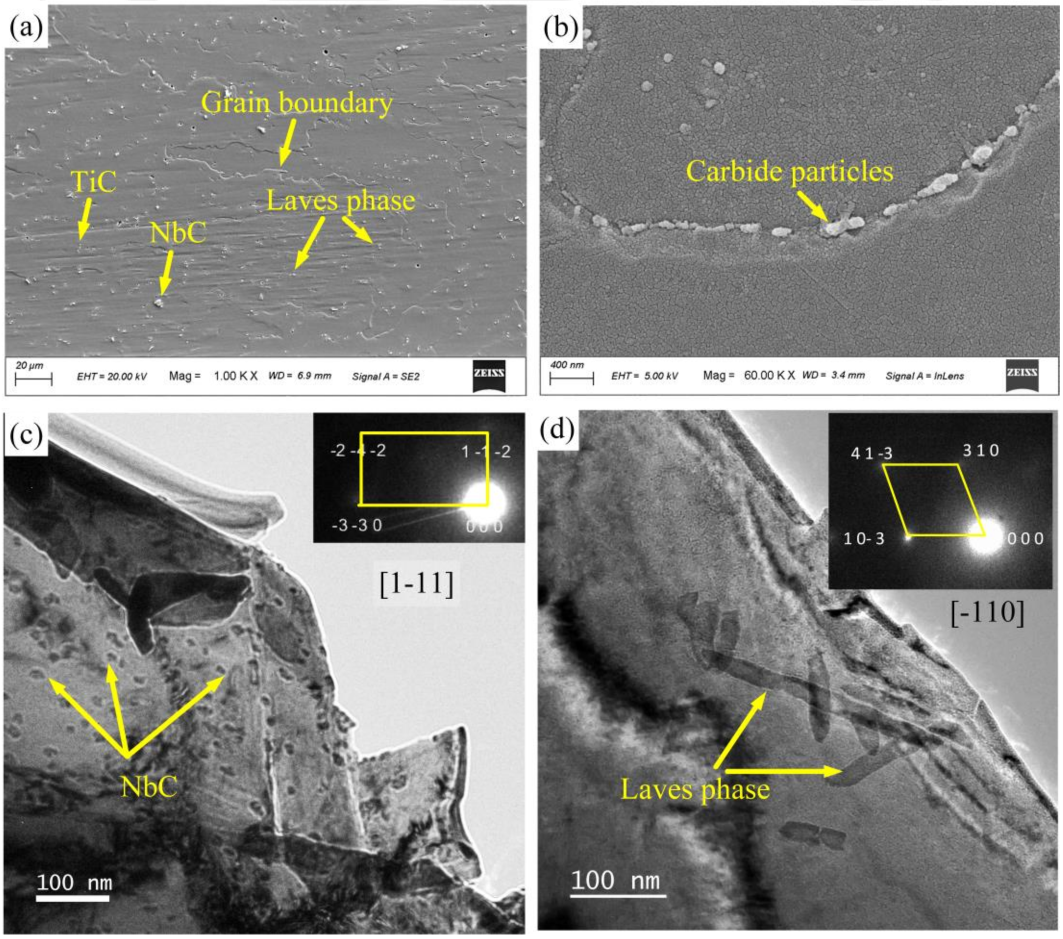

Fig. 5.8 (a) Fusion zone microstructure of STWB, (b) magnified view of the grain boundary, (c) TEM bright field image of carbides and (d) Laves phases

Figure 5.8 (b) represents the enlarge view of grain boundary of the STWB. Which revels that grain boundaries consist of small chain like particles of ~ 175 nm width. The TEM bright field image and SAED pattern of this particle confirm as the NbC (Fig. 5.8 (c-d)). During ST, the Laves phases dissolve and release a significant amount of Nb. This excess Nb subsequently facilities the formation of MC type carbides (Sahu & Bag, 2021).

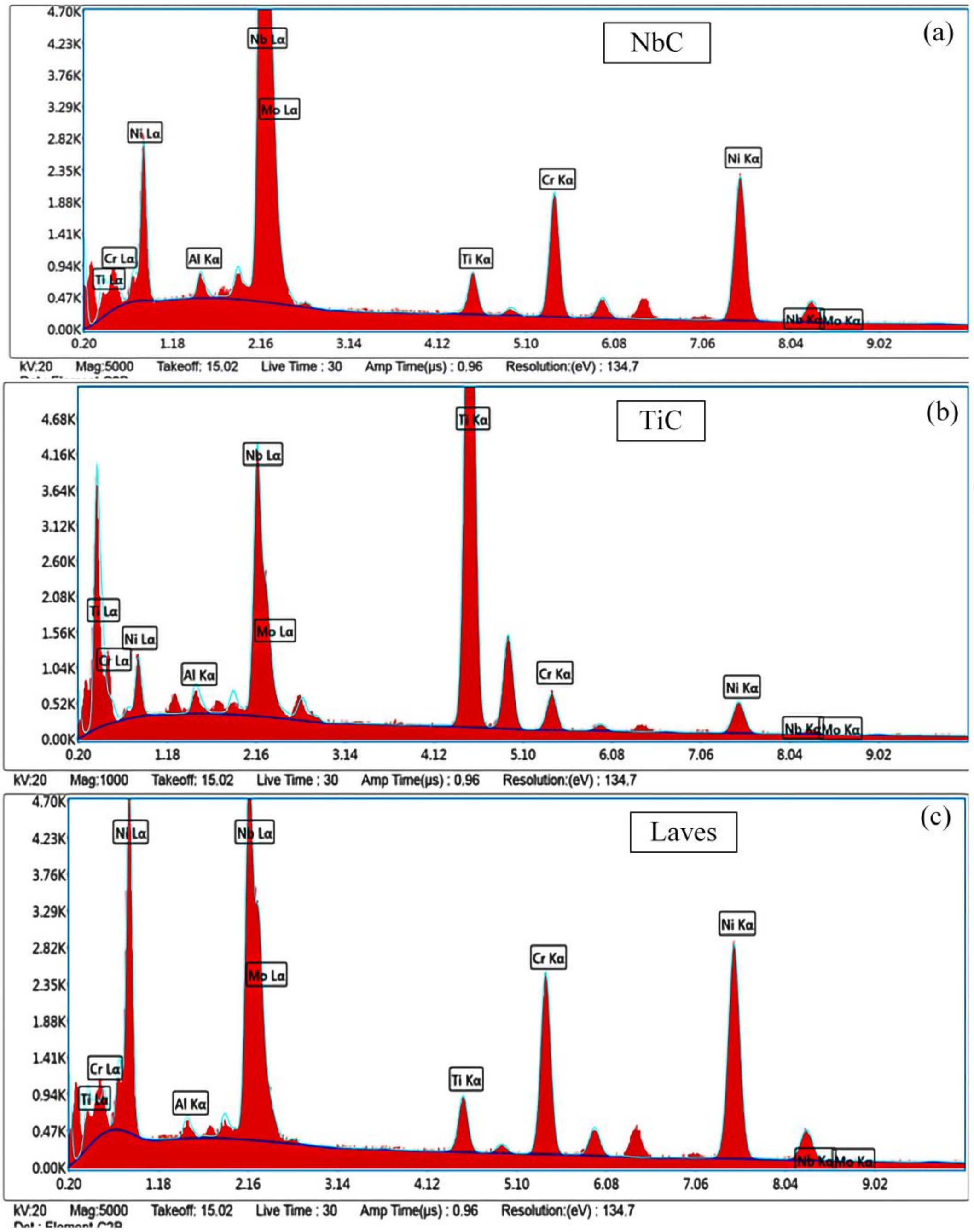

Fig. 5.9 EDX point analysis of (a) NbC (b) TiC (c) Laves and (d) summary of elemental composition

The XRD analysis is performed to investigate the crystallographic characteristics of the BM, FZ of the welded blank and the FZ of STWB. Figure 5.10 (a) displays the XRD patterns of all the cases. The peaks of different phases are identified by using standard JCPDS files (01-082-8282, 00-002-1031 and 00-1999). The prominent diffraction peaks of the as-received BM, at 2θ angles, are approximately 44.5°, 51.9°, 76.4°, 92.91º and 98.4º correspond to the (111), (200), (220), (311) and (222) planes of the FCC- γ phase. It is found that the width of the diffraction peak in STWB is smaller than the MPAWB, which indicates that the residual stress in MPAWB sample is decreased after ST. An extra NbC peak is also observed in the sample of STWB at 70.68º in (311) plane, which has good agreement with the FESEM and TEM analysis.

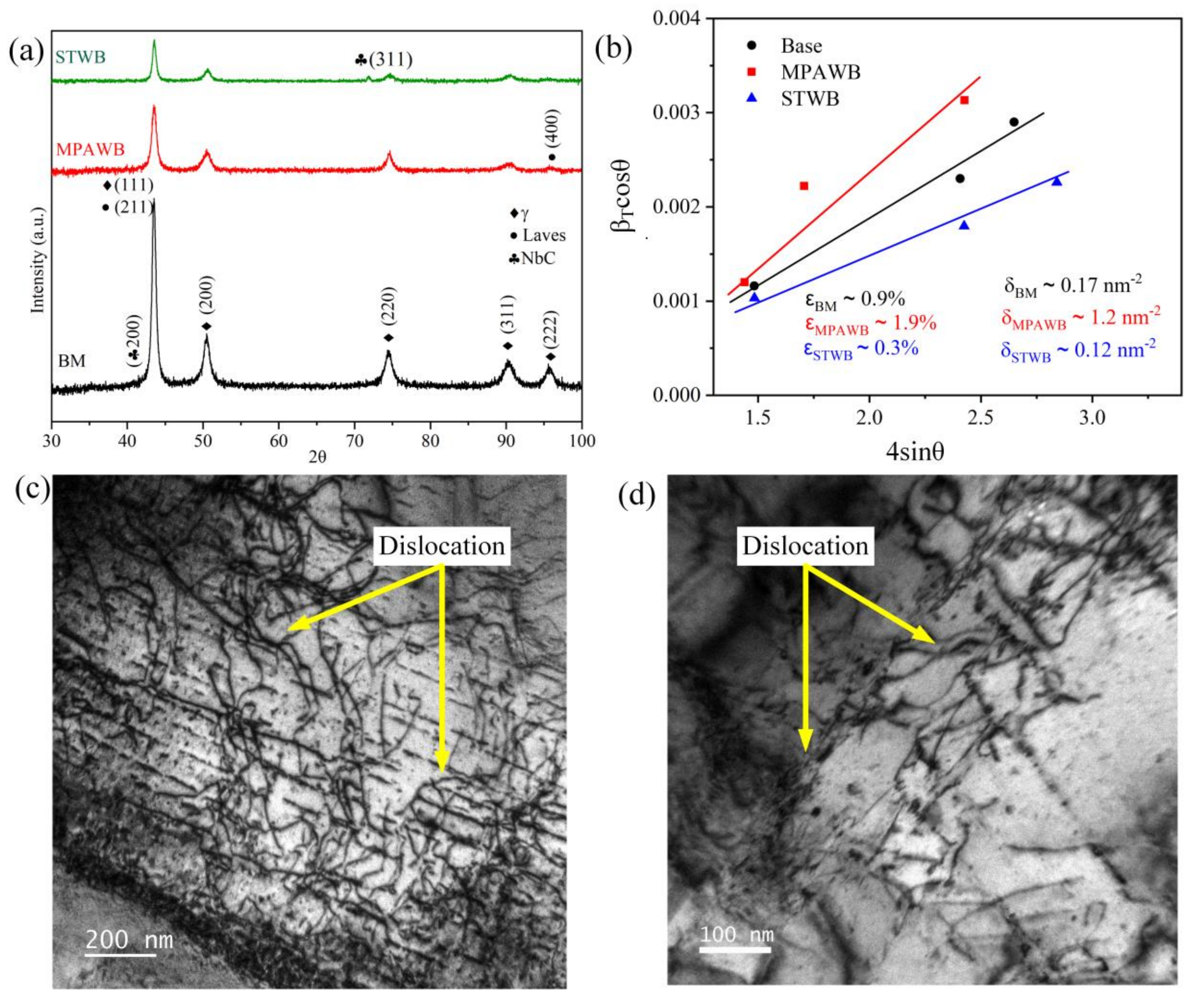

Fig. 5.10 (a) XRD pattern of as-received BM, FZ of as welded sample and FZ of STWB, (b) the peak broadening βcosθ as a function of 4sinθ, where the slope of the linear fit represents the value of micro strain, (c) TEM brightfield image showing dislocation density of as welded sample and (d) TEM image showing dislocation density of STWB.

The micro strain and dislocation density of the BM, as-welded MPAWB and STWB are calculated by Williamson–Hall method, as per Eqs. (1-2), from the XRD data.

$$\beta cos\theta = \frac{K\lambda}{D} + 4\varepsilon sin\theta \quad (1)$$

$$\delta = 2\sqrt{3}\varepsilon/(Db) \quad (2)$$

Where, β is the combined peak broadening of the Bragg's peak, λ= 0.15406 Å is the wavelength of Cu K-α radiation, k= 0.9 is the coefficient, D is the size of micro crystalline, b is the Burgers vector (0.2 nm), θ is the Bragg's angle of XRD profile. The lattice strain (ε) is calculated by linear fitting of the Eq. (1). The dislocation density (δ) is measured from Eq. (2). The lattice strain is maximum for the case of MPAWB, and the STWB has lowest amount of lattice strain. This indicates that during the ST, recrystallization takes place, which reduces the lattice strain. ST also helps to relieve thermal stresses developed during the welding process within the material, which can contribute to low lattice strain. It is observed that MPAWB has maximum dislocation density with the comparison of STWB (Fig. 5.10 (b)). The main reason behind the lower dislocation density of the STWB is the dissolution of the intermetallic phases during the ST. The TEM analysis of the FZ of MPAWB and STWB also reveals that the MPAWB has dense dislocation density (Fig. 5.10 (c-d)). The high dislocation density may resist against the deformation and exhibit higher flow stress (Gashti et al., 2016).

5.3 Micro hardness and tensile test

The hardness behaviour of the MPAWB and STWB is represented in the Fig. 5.11. The hardness profile revels that the hardness of the FZ of MPAWB is higher (268.9 ± 9 HV) than that of the as-received BM (200 ± 5.2 HV). The hardness value of the MPAWB gradually increases from the BZ to FZ. During MPAW, the FZ experiences a rapid heating and cooling cycle. The rate of cooling in the FZ is generally much higher than the other zones of the WB. This is because of the localized concentrated heat input during the MPAW. The faster cooling can lead to the formation of hard and brittle phases as well as trapping of dislocations. Both of these increase the hardness of the FZ. It is already discussed that the FZ of the welded blank consists of secondary phase like Laves and carbides, which are harder than the BM. Moreover, during the solidification of weld pool, the constitutional alloying elements of Inconel 625 segregate and deposit near the dendritic grain boundaries and increase the hardness value. A significant hardness variation is also observed between the MPAWB and STWB. Due to the ST, the hardness values of the BZ and FZ of the STWB are reduced. The maximum FZ hardness of the STWB is found as

252.16 ± 6.73 HV and maximum BZ hardness is 119.43 ± 7.12 HV. The main reason behind the reduction of microhardness values of the STWB is the dissolution of Laves phase. Moreover, due to the ST, the dendritic microstructures are melted and formed a homogeneous microstructure. Thus, the hardness of the STWB is found lower with comparison of MPAWB.

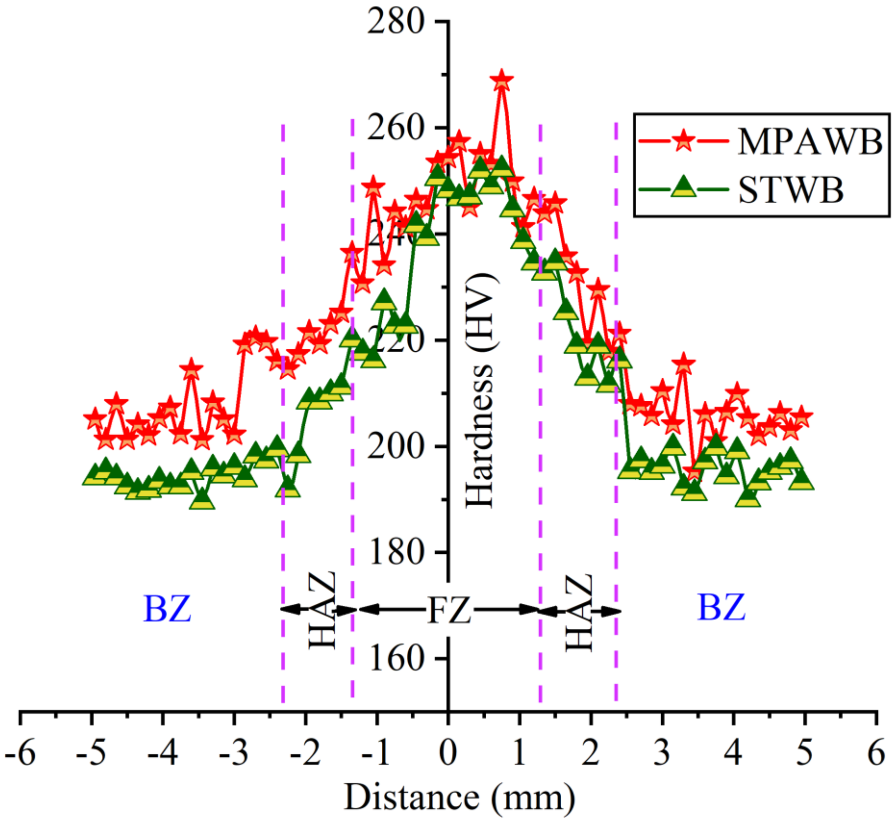

Fig. 5.11 Hardness profile of the MPAWB and STWB

The tensile tests are performed for the as-received Inconel 625 BM, MPAWB and STWB. The engineering stress-strain data is presented in Fig. 5.12 (a), along with the corresponding fracture locations (Fig. 5.12 (b)). The Inconel 625 base material exhibits impressive mechanical properties, 53.80% elongation and UTS of 846.51 MPa. The UTS of MPAWB is 841.45 MPa, *i.e.*, joint efficiency of 99.4%. Microstructural analysis (Section 3.1) indicated that the FZ of the welded blank contains brittle dendritic structures resulting from the segregation of alloying elements and the formation of intermetallic Laves phases and carbide particles. Consequently, the FZ exhibits a brittle nature, which is reflected in the mechanical behaviour. As a result of this, the overall elongation of the MPAWB is found with 40.02%.

The STWB shows 44.98% elongation, which is 12.39% more than the MPAWB. The microstructural analysis of the STWB reveled (Section 3.1) equiaxed grains in the FZ. This type of micristructure is preferable than the dendritic structure for ductility improvement of Inconel 625. Generally, during the deformation of MPAWB the secondary phases like carbides and Laves hindrance the flow of dilocations. However, in the case of STWB, there is few secondary phases remain on the matrix to produce obstracle against the flow of dislocations. Thus, a good ductility is achieved after the ST.

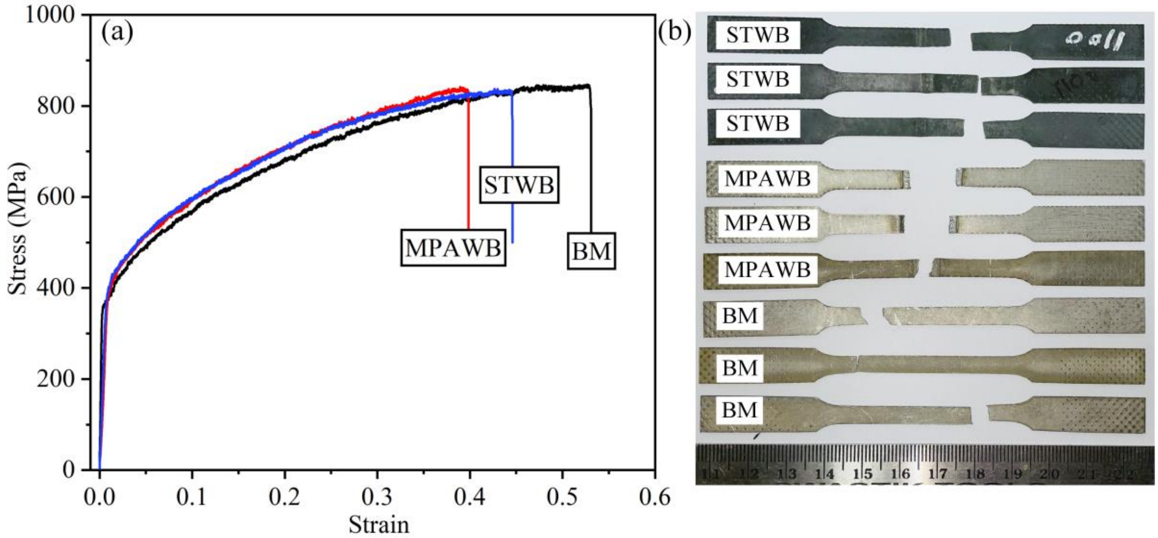

Fig. 5.12 (a) Engineering stress-strain plot and (b) photograph of fractured tensile specimens

The true stress-strain are evaluated from the load-displacement data to obtain the n-value, and K-value. In this regard the logarithmic true stress-strain values, in the hardening region, is fitted following the Hollomon hardening law, shown in Eq. (2). The measured mechanical properties are presented in Table 5.2. Figure 5.13 represents the true stress-strain and strain hardening diagrams. It is observed that STWB has higher n-value (~ 0.36) than MPAWB (~ 0.34). Generally, the strain hardening exponent is significantly influenced by the grain size, presence of secondary phases, and dislocation density. In metallic materials, there exists an inverse relation between the yield strength and n-value. Specifically, the materials with lower yield strength tend to exhibit higher n-value. The yield strength of the MPAWB is reduced following the ST, leading to an increase in the n-value. Furthermore, the phenomenon of strain hardening is a consequence of dislocation multiplication. A higher initial dislocation density tends to slow down the dislocation multiplication, resulting in a lower n-value. The XRD analysis has already been reveled that the dislocation density of the MPAWB is higher than the STWB. Materials with a higher n-value can undergose more plastic deformation, which is a preferable characteristic for sheet metal forming.

$$\sigma = K\varepsilon^n \quad (2)$$

Table 5.2 Mechanical properties obtained from tensile test

Sample	UTS (MPa)	YS (MPa)	Elongation (%)	K-value	n-value
BM	846 ± 12.2	365 ± 9.8	53.8 ± 5.0	1642 ± 12.3	0.37 ± 0.02
MPAWB	841 ± 4.2	409 ± 8.2	40.0 ± 4.2	1618 ± 11. 2	0.34 ± 0.01
STWB	837 ± 5.5	396 ± 6.2	44.9 ± 4.2	1598 ± 8.2	0.36 ± 0.05

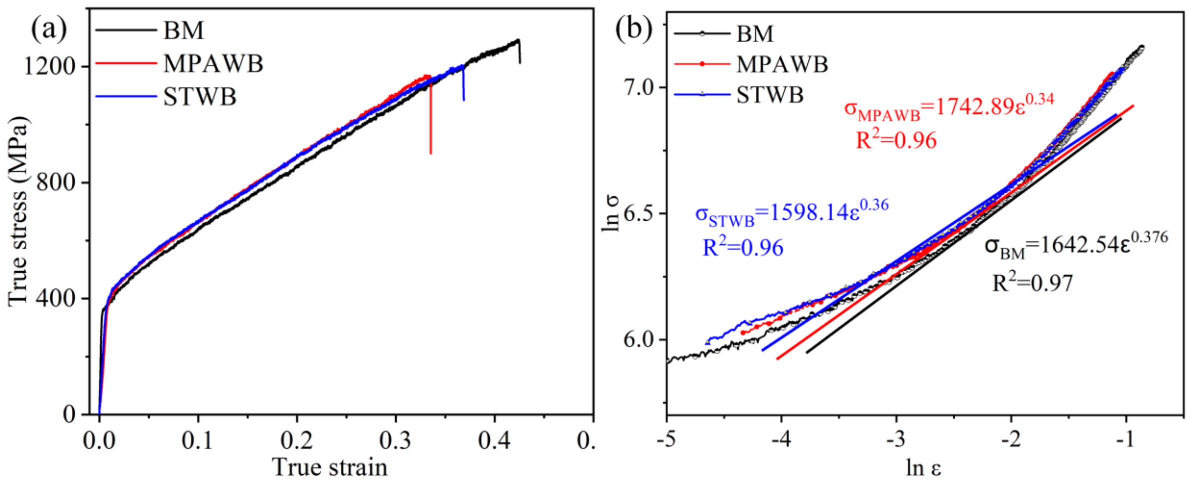

Fig. 5.13 (a) True stress-strain and (b) Strain hardening curve

It is observed from the Fig. 5.12 (b) that all MPAWB fails from the FZ center. The microsegregation during the welding of Inconel 625 produces a concentration variation of alloying elements at the FZ. Such variations can lead to localize weaknesses, making the center of the FZ more susceptible to failure. Moreover, Inconel 625 is prone to the formation of intermetallics, which are often brittle in nature and weaken the material. It is also observed that all the STWBs fail from the BM which is far from the FZ. The Inconel 625 is a solid solution strengthen alloy which is strenthened by different types of alloying elements like Co, Cr, Fe and Mo. These elements combine with the γ matrix and provides strength. However, due to the ST most of the secondary phases like blocky carbide chains presence in the as-received BM break down, and average grain size also increases. These causes weaken the BM after ST. Thus, the failure of the STWB is taken from the BZ instead of FZ.

5.4 Formability analysis

The formability of the as-received BM, MPAWB, and STWB are measured by LDH tests. Figure 5.14 represents the stretched specimens from the biaxial to uniaxial strain paths. The highest point of stretched dome is marked as the pole, illustrated in Fig. 5.15. It is found that the BM in lubricated condition is failed from the the pole. During the LDH test under lubricated condition, the friction between the interface of punch and blank is less with the comparison of dry condition. The reduction in friction allows for easier stretching of the blank, which leads to necking and thinning of the specimen at the pole. Due to the similar reason the MPAWB and STWB, in lubricated conditon, also fail near the pole, which is parallel to the weld line. However, in dry condition the S1 specimen of BM fails away from the pole. Similarly, the S1 specimen of MPAWB fails far from the pole and the failure is initiated from the center of the FZ and propagates towards to the BM. The microstructural and microhardness analysis showed that the FZ consists of dendritic structure with brittle secondary phases. The S1 to S6 specimens of the STWB fail predominantly from the BZ. As discussed earlier, due to the ST, the microstructure of the FZ becomes homogeneous. Moreover, the dissolution of the laves phase improves the FZ ductility. Because of these reasons, the STWB does not fail at the FZ. The BM after ST loses its strength due to the dissolution of secondary phases like metastable γ''. Thus, all the STWB specimens fail from the BZ.

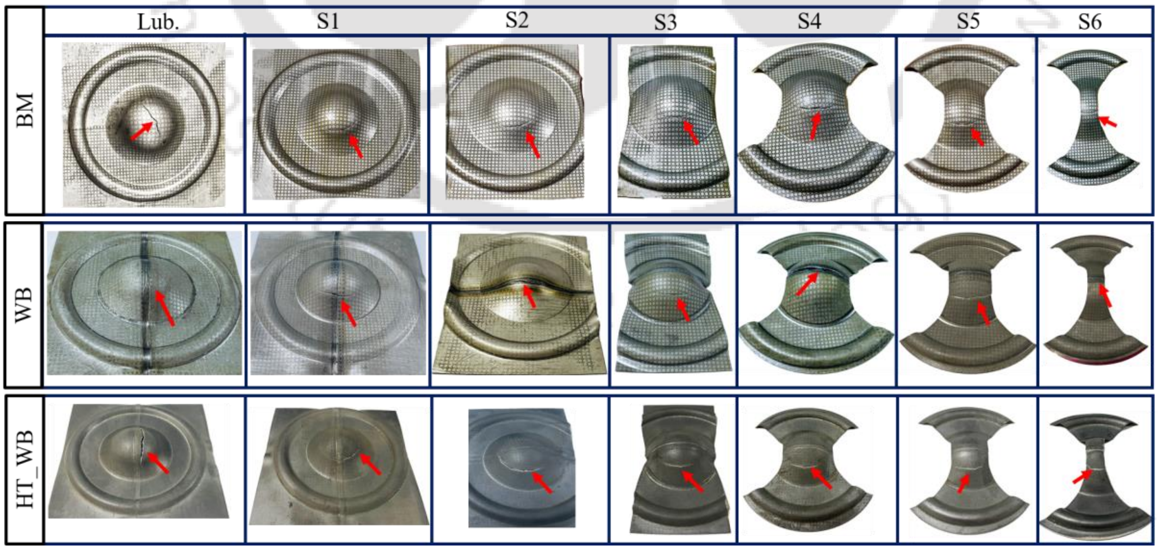

Fig. 5.14 LDH test specimens in different strain paths of the as-received BM, MPAWB and STWB, the red arrows indicate failure locations

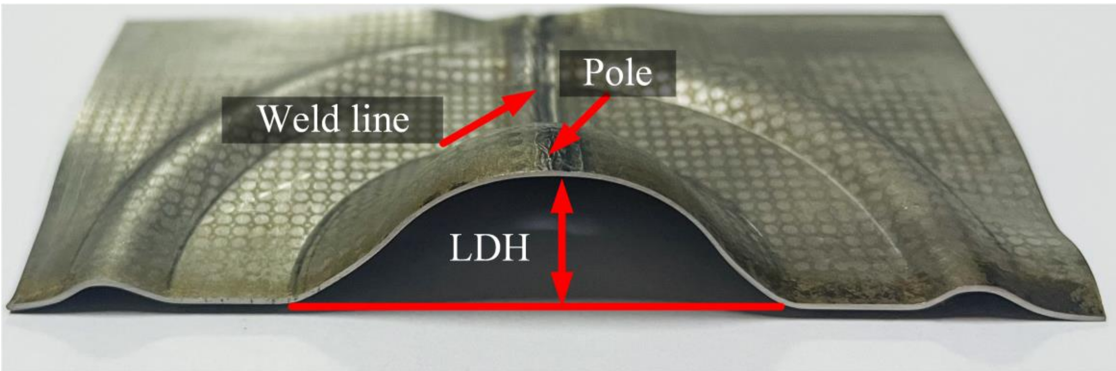

Fig. 5.15 Cross section view of S1 stretched specimen

The measured LDH in lubricated condition, and three different srain paths, i.e., S1, S4 and S6 for the BM, MPAWB and STWB are presented in Table 5.3. It is observed that the as-received Inconel 625 BM has maximum LDH. The LDH of S1 specimen for STWB is 12% higher than the MPAWB. Besides, the specimens in strain path S4 exhibit minimum LDH for all the cases. This could be attributed to the possibility of the S4 specimens closely approach to the plane strain condition. The minimum width strain path specimens i.e., S6, are found with maximum LDH for all the cases. This may be happened because the S6 specimen stretched following the uniaxial strain path. The LDHs of S6 specimens for MPAWB and STWB are 13.7 mm and 14.89 mm, respectively.

Table 5.3 Experimental measured limiting dome height in various strain paths

Strain path	Specimen		
	BM	MPAWB	STWB
Lubricated	11.7 ± 0.21	10.2 ± 0.89	11.4 ± 0.22
S1	10.6 ± 0.52	9.1 ± 0.77	10.2 ± 0.25
S4	10.2 ± 0.10	8.2 ± 0.66	9.8 ± 0.50
S6	15.6 ± 0.41	13.7 ± 0.63	14.8 ± 0.87

Figure 5.16 represents the load-displacement (LD) plots for the specimens S1 and S6, which are having maximum (80 mm) and minimum (10 mm) widths, respectively. It can be observed that the load required for the BM in S1 and S6 strain paths are highest as ~26.85 kN and ~12.05 kN, respectively. More displacement indicates more punch movement inside the workpiece, and high displacement requires more force.

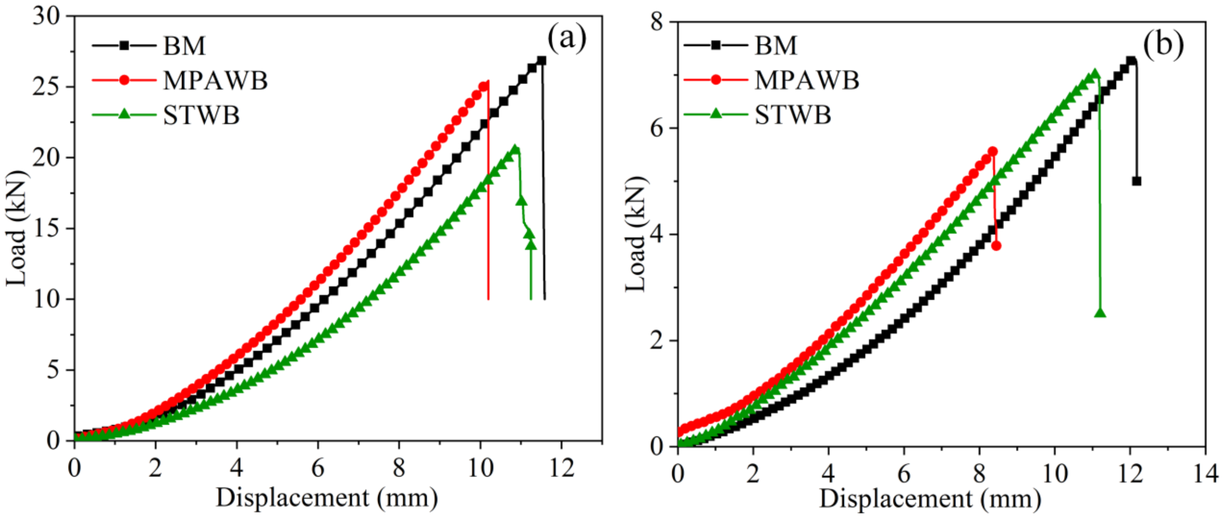

Fig. 5.16 Load-displacement diagram for (a) S1 and (b) S6 specimens

The S1 specimen of STWB is found with higher displcement of 10.89 mm than the MPAWB as 10.04 mm. The slopes of the LD curves of MPAWB are higher than the BM and STWB for both the strain paths. It is observed from the hradness test that the FZ is more harder compared to other regions due to the presence of secondary phases and dendritic structures. Thus, during the bulk deformation in LDH test, the MPAWB produces larger resistance against the deformation and behaves as more brittle than the other specimens.

In LDH test, specimens are stretched from biaxial to uniaxial, as a result the etched circular grids printed on the surface of the workpiece get elongated and transforming into ellipses. Following the Eq. (3) and using the data obtained from both the fractured and non-fractured grids true major strain (ε_1) and minor strain (ε_2) are computed. These strain values are subsequently depicted in the FLD, as illustrated in Fig. 5.17. The boundary that distinguishes the fracture zone from the safe zone is mentioned as the FLC, the zone situated just below the FLC represents the necking zone. The strain ratio [$\alpha = (\varepsilon_2/\varepsilon_1)$] is calculated for all samples and represented in Table 5.4. The full dimension specimen (80 mm × 80 mm) in lubricated condition for all the cases are stretched biaxially as the α value is near to unity. Furthermore, the strain ratios of S1, S2, and S3 specimens are also remained within the tension-tension region. In contrast, the specimens S4, for all the cases, exhibit stretching behavior as plane strain path, characterized by α value close to zero. The specimens with the narrowest width, denoted as S6, exhibit a α value close to -1/2, indicating that these specimens are stretched according to a tension-compression strain path.

$$\varepsilon_t = ln\,(\frac{d_f}{d_o}) \tag{3}$$

Where, ε_t is true strain, d_o is initial grid diameter and d_f is final diameter after stretching.

Table 5.4 Variation of strain ratio in different strain paths specimens

			α = ($\varepsilon_2/\varepsilon_1$)				
Specimen	Lub.	S1	S2	S3	S4	S5	S6
BM	1.06	0.58	0.57	0.09	0.04	-0.18	-0.52
MPAWB	1.04	0.74	0.54	0.01	0.02	-0.21	-0.57
STWB	1.01	0.63	0.48	0.056	0.001	-0.26	-0.49

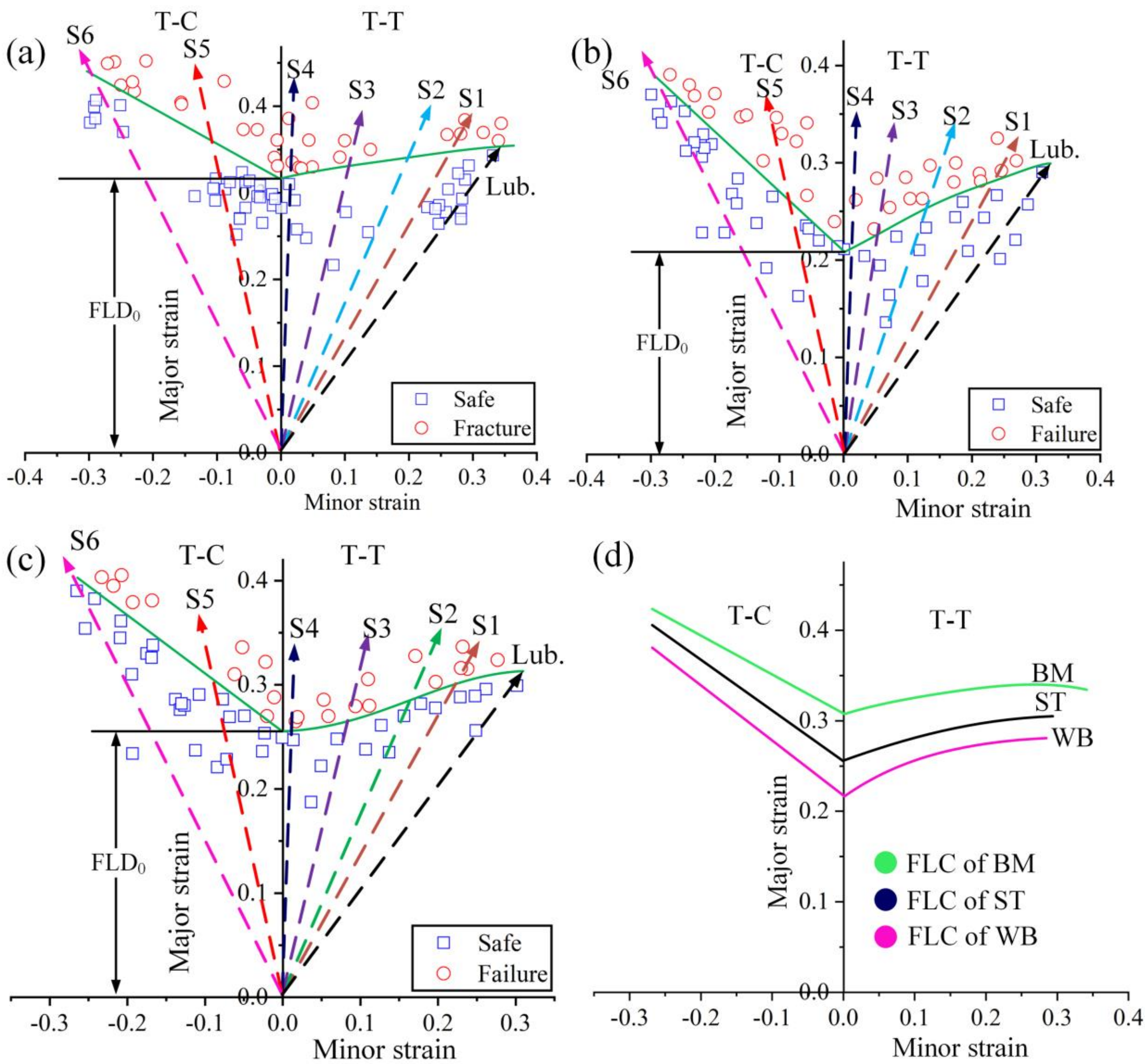

Fig. 5.17 (a) FLD of Inconel 625 BM (b) FLD of MPAWB (c) FLD of STWB and (d) comparison of forming limit curve

The inter-section of the FLC and major strain axis is considered as FLD_0. A comparison of FLCs of BM, STWB and MPAWB is shown in Fig. 5.17 (d). The FLD_0 of the BM is 0.32 (Fig. 5.17 (d)), which is highest among all the cases. The FLD_0 of the MPAWS and STWB are 0.23 and 0.26, respectively. Due to the dissolution of secondary phases during ST, the obstacle of dislocations movement is reduced. Thus, the STWB could stretch more than the as-welded sample without fracture.

The surface strain distribution of the S1 specimens are calculated for the BM, MPAWB and STWB to draw a comparison among them. Figure 5.18 represents the surface strain distribution profile of one side of the pole, due to symmetrical shape of the stretched dome other side is not considered. The maximum stretching is occurred far from the pole and minimum near to the draw bead. The BM, MPAWB and STWB have 0.26, 0.20 and 0.15 major strains, respectively, at the pole. On the other hand, at the pole they have 0.09, 0.07 and 0.03 minor strains. The maximum major strains for the BM, MPAWB and STWB are found as 0.41, 0.28 and 0.23, respectively. As both the minor and major strains are positive, the strain path of the S1 specimens is considered as tension-tension.

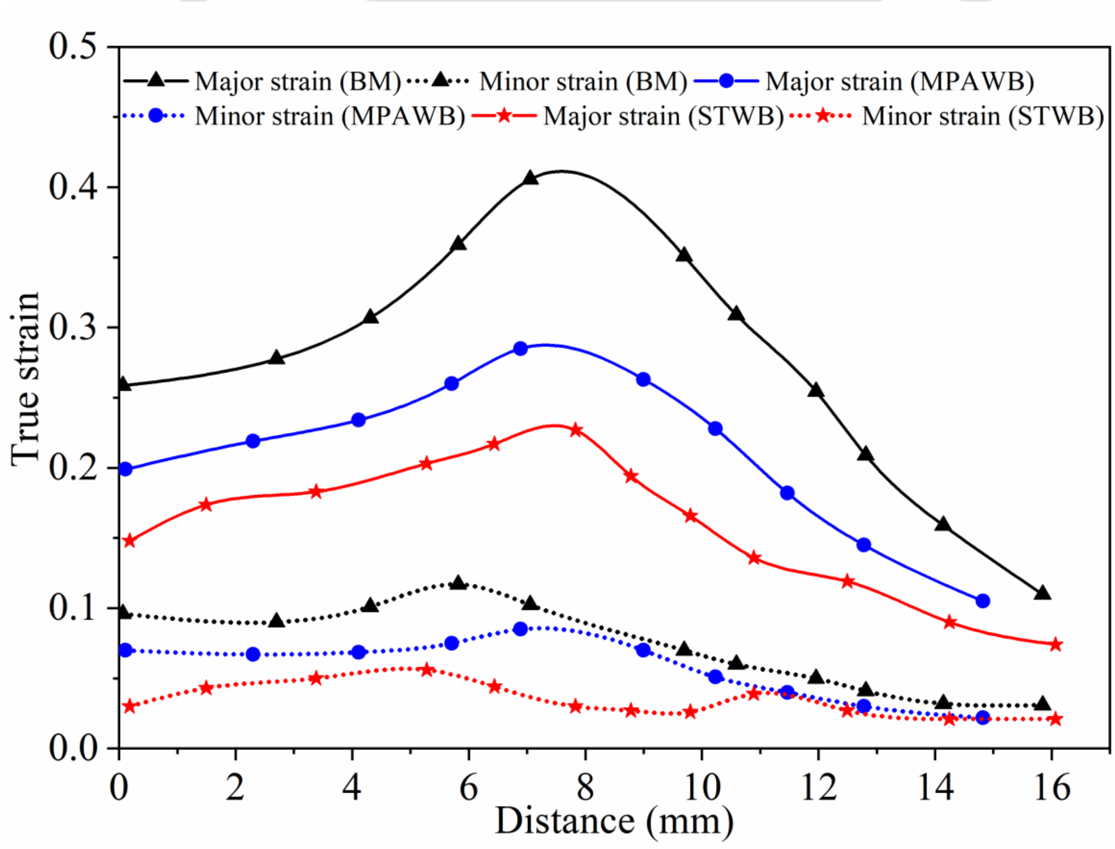

Fig. 5.18 Surface strain distribution profiles of S1 specimens for BM, MPAWB and STWB

The thickness distribution of S1 specimen is measured from an extreme end of the dome to the pole. Figure 5.19 (a) depicts the cross section of the dome and Figure 5.19 (b) shows the thickness distribution profiles of the BM, MPAWB and STWB. It is found that the thick distribution profile is not uniform across different locations of the stretched dome. This occurs due to the generation of varying stress and strain conditions across different sections of the stretched dome. It is observed that the maximum thinning is occurred far from the pole. As maximum stretching occurs with the BM, thus more thinning (42%) is observed in this case. Besides, the MPAWB and STWB are found with 33% and 38% thickness reduction after stretching.

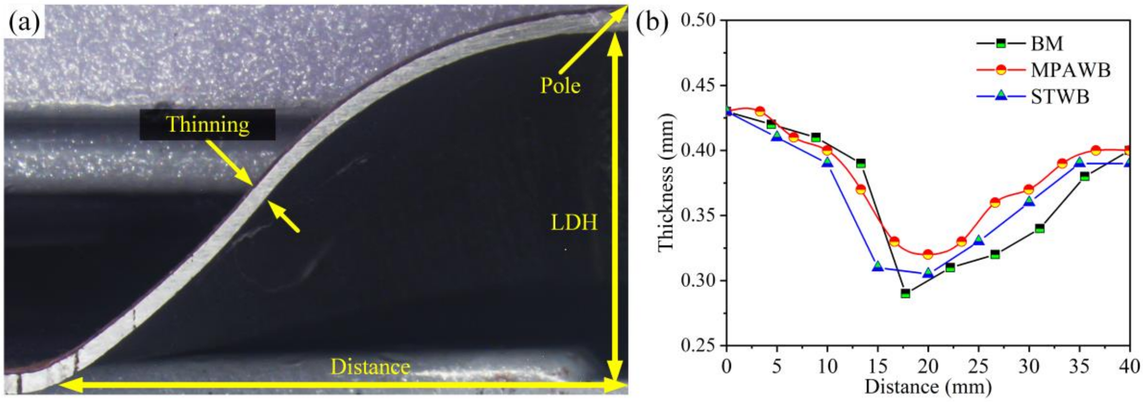

Fig. 5.19 (a) Cross section view of a stretched dome and (b) thickness distribution of S1 specimens

The fracture surfaces of the S1 specimen for the MPAWB and STWB are charcterized to study the mode of failure in biaxial loading condition. Figure 5.20 represents the fracture surfaces of the MPAWB and STWB. It is observed that the MPAWB consits of shallow and large dimples with honeycomb structures and some voids, generated due to the plucking of materials during the LDH test. Which confirms ductile mode of failure. The fracture surface of the STWB consists of fine honeycomb structure, voids and dimples. The STWB fails from the BZ instead of the FZ. The LDH test as well as tensile test both confirm that the STWB is more ductility with the comparison of MPAWB.

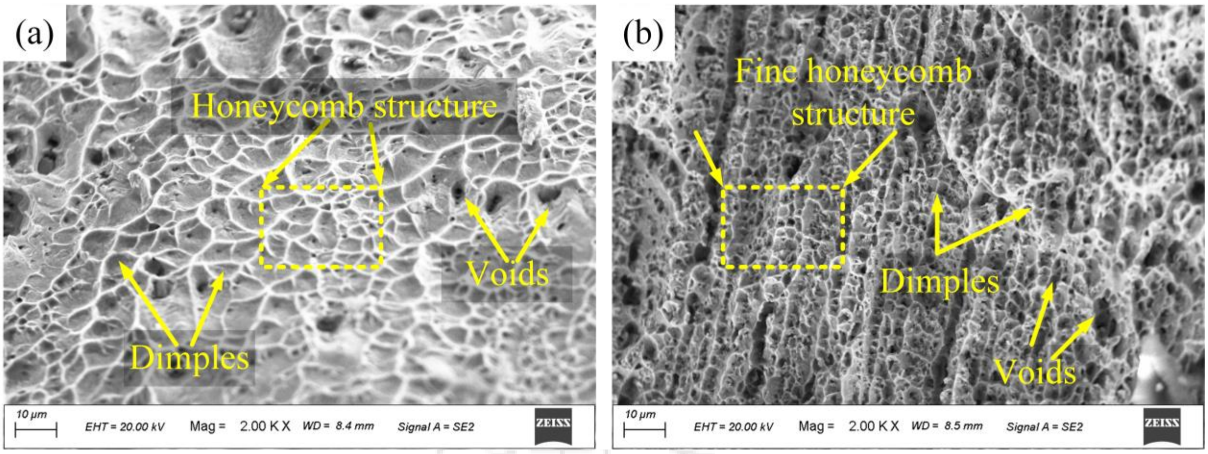

Fig. 5.20 Fracture surface morphology of (a) as-welded Inconel 625 sample and (b) STWB

5.5 Summary

MPAW is used to join thin nickel based super alloy Inconel 625. Subsequently, the WBs are solution treated at 1100 ºC to study the formability of them. The joint metallurgy is studied to make a correlation among the FZ metallurgy and mechanical properties like tensile strength, maximum elongation and formability of the MPAWB. It is observed that the FZ of the MPAWB consists of long cellular and equiaxed cellular dendritic structure. The dendritic boundaries are comprised with Laves network, with some distributed NbC over the γ matrix. Because of these secondary phases, the hardness and yield strength become higher than the BM and STWB. A massive change is observed in metallurgy at the FZ after the ST. After solution treatment, an equiaxed homogeneous microstructure is achieved in the FZ of the welded blank due to dissolution of irregular dendritic structures. Because of this, 12.39% higher elongation is achieved for the STWB with comparison of MPAWB. The FLDs are established successfully through the experimental tests results involving deformation along six different strain paths. The solution treatment improves the formability of the STWB by dissolution of intermetallic and secondary phases. The surface strain and thickness distribution profile of S1 specimens are measured experimentally for the as-received BM, MPAWB and STWB. More thinning is witnessed far from the pole for all the three cases. Maximum 42% thinning is found for the case of BM, 33% for the MPAWB and 38% for the STWB.

Chapter 6

Influence of fusion zone metallurgy on the mechanical behaviour of Inconel 625 and 316L stainless steel dissimilar joint

6.1 Introduction

Dissimilar joining of material not only full fill the service requirement but also results in huge cost reduction due to the replacement of expensive materials by relatively cheaper one. Inconel 625 has the ability to retain mechanical properties and corrosion resistivity from room temperature to elevated temperature. Thus, it gains huge demand in different industries like aerospace, nuclear power plant, gas turbine etc. (Hu et al., 2021). Besides, 316L stainless steel is a low-cost structural material which has excellent corrosion resistivity, good mechanical properties, better thermal conductivity etc. (Yao et al., 2023). Hence, this material has large applications in high corrosive atmosphere, medical devices, chemical pipe lines, marine equipment etc. (Guo et al., 2023). By dissimilar joining of alloy Inconel 625 and 316L stainless steel, the overall cost can be reduced without affecting the functionality of the whole system. The dissimilar joining is commonly used in the field of nuclear industry, sub-size boilers, liquid rocket components in association with gas turbines, and cryogenic engines. Recently, NASA (Dreshfield et al., 1992) has developed a small scale boiler with the combination of this two alloys. Besides, this dissimilar sheet welded joint is used in different industries. However, the chance of formation of intermetallic compound increases in dissimilar joining of Inconel 625 and 316L stainless steel, which has direct effect on the formability of the welded blanks. Therefore, achieving desired three-dimensional shape with uniform strain distribution across the surface of dissimilar welded blanks using a rigid tool, devoid of issues such as wrinkling and breakage, presents a considerable challenge.

This chapter is solely focused on the successfully joining of alloys Inconel 625 and 316L stainless steel by using MPAW. Thereafter, the formability of the welded blank is measured by LDH test and compared with the as received parent materials. The cause and location of failure of the MPAWB are analyzed thoroughly by metallurgical study.

6.2 Microstructural analysis

The microstructures of as received BMs are evaluated in Fig. 6.1. It is observed that both the BMs, (i.e., 316L stainless steel and Inconel 625) incorporate with equiaxed grains and some annealing twins, which may have formed at the time of rolling operation. It is clear from Fig. 6.1 (a) that a homogeneous distribution of δ-ferrite is evident on the γ-matrix in the BM of 316L stainless steel with an average 12 μm grain size. Whereas, an average of 45 μm large grains are observed in Inconel 625 BM. In which some Nb rich secondary phases are found distributed over the primary γ-matrix is represented in Fig. 6.1 (b), which is confirmed by EDX point analysis.

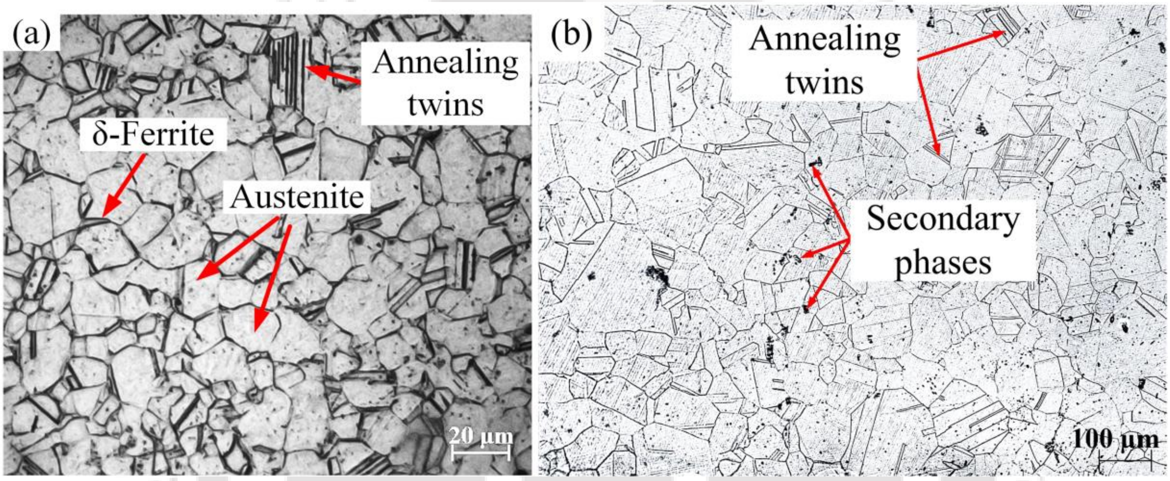

Fig. 6.1 Optical images of (a) 316L stainless steel and (b) Inconel 625 base materials

The macro view of the weld region is shown in Fig. 6.2 (a). The macrograph reveals three discrete zones, namely BM zone, HAZ, and FZ. A higher magnification view of the FZ and the interface of FZ-BMs are analysed separately by FESEM and shown in Figs. 6.2 (b-e). In Fig. 6.2 (b), it can be easily visualized that the FZ and the HAZ of the 316L stainless steel is separated by a narrow partially melted zone named as transition zone. An epitaxial grain growth is occurred during the solidification of the transition zone. This is happened due to the presence of more than one phases inside the material. However, a different kind microstructural structures are evident at the FZ, located near to the Inconel 625 BM. These differences are attributed to the effect of asymmetric Marangoni convection, where variations in surface tension between the base metals create uneven flow patterns in the molten pool (Bahrami et al., 2015). As result of this asymmetric FZ morphology is observed at the interface of 316L stainless steel-FZ and Inconel 625-FZ. A grain refinement can be observed at the HAZ due to faster cooling of the welded blank.

Figures 6.2 (c-e) shows different types of microstructure present at the FZ. The microstructure consists of different types of dendritic structure at different locations of the FZ. Mo and Nb have a low equilibrium distribution coefficient (Hardy et al., 2020), which is the main reason for the formation of severe segregation during the solidification of weld metal. Due to a similar reason, these elements have a higher tendency to solute redistribution in the time of solidification (Lippold et al., 2005). Because of solute redistribution, the temperature gradient in solid and liquid interface gets reduced, which promotes the constitutional super cooling. Consequently, the mode of solidification changes from cellular to dendritic or equiaxed.

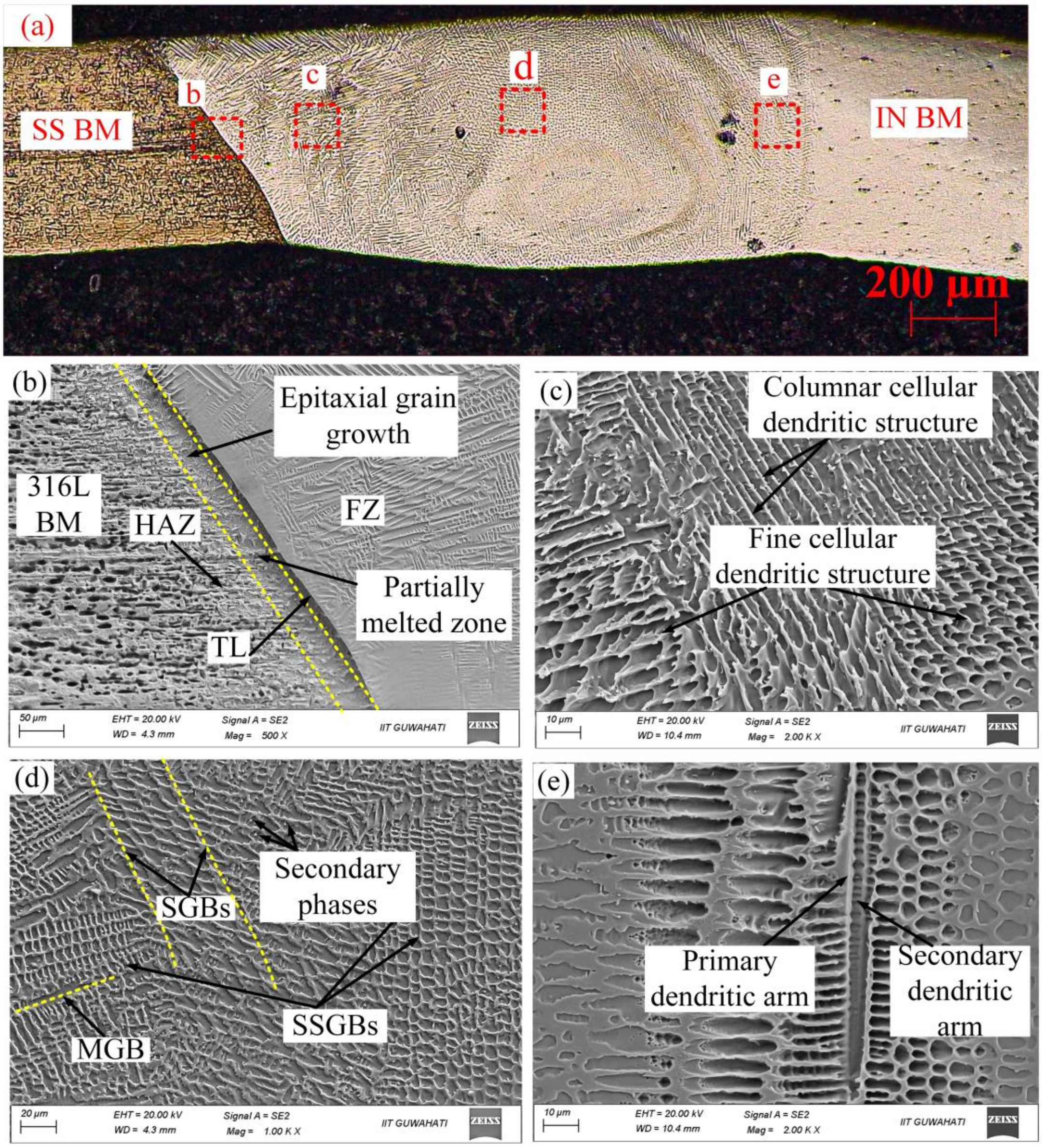

Fig. 6.2 (a) Macro view of Weld cross section, Microstructure (b) at the 316L stainless steel-FZ interphase (c) near the TZ (d) FZ center and (e) FZ-Inconel 625 interphase

Figure 6.2 (c) shows an FESEM image of the FZ near the transition zone, which has columnar and fine cellular dendritic structure. However, the solidification mode is varied from equiaxed to dendritic when moving from weld center to the fusion boundary. Dendritic morphology changes at the FZ are controlled by the temperature gradient (G) and solidification rate (R) ratio (G/R). Kou (Kou, 2003) addressed that this ratio is minimum at the center of FZ and maximum near the transition zone at a constant temperature gradient because of the higher solidification rate. Hence, the *G/R* ratio at the weld center is relatively smaller than the fusion boundary, which stimulates constitutional supercooling. As a result, the mode of solidification switches from dendritic to equiaxed dendritic. Three types of grain boundaries namely, solidification subgrain boundaries (SSGBs), solidification grain boundaries (SGBs), and migrated grain boundaries (MGBs), are observed at the weld center (Fig. 6.2 (d)). Fine honeycomb like cell structure and small dendrites are found at the weld center, and they are separated from each other by SSGBs. Because of their compositional differences from the bulk microstructure, these boundaries are visible in the microstructure (Lippold et al., 2011). The long SGBs are observed at the center of the FZ, which separates different groups of SSGBs. The formation of solidification grain boundaries (SGBs) is caused by the meeting of subgrains packets that compete with each other for growth at the end of the weld pool. As each group of grains has a distinct growth direction and orientation, their intersection creates a boundary with significant angular misalignment, which is generally referred to as a "high angle" grain boundary. The angular mis-orientation between SGB and SSGB is mainly responsible for the formation of dislocation network at the center of FZ. Some MGBs are also observed at this particular location, and it is formed due to the migration of crystallographic components of SGBs. Few small size (1.6 μm) secondary phases are also observed in interdendritic regions. The FZ microstructure adjacent to the Inconel 625 base zone differs from the microstructure near the 316L BZ and no unmixed regions are observed at this location (Fig. 6.2 (e)). Bright long primary and secondary dendritic arms with dark dendritic core is observed in this region. It is observed by many authors that the thermal conductivity of Nickel based alloy is higher than the thermal conductivity of austenitic steel at elevated temperatures (Shakil et al., 2014). Therefore, Inconel 625 side of the weldment would have a much steeper temperature gradient than the 316L stainless steel side. Extreme solute redistribution and concentration gradient variation may be responsible for the formation of such microstructure.

Figure 6.3 (a-c) represents the EDX point analysis of different locations of the FZ and Table 6.1 lists the average composition at the 316L stainless steel BM, 316L/FZ interface, FZ, FZ/ Inconel 625 interface, and Inconel 625 BM. The Table 6.1 shows that the Wt.% of Cr, Nb, and Mo in the FZ center are much higher than the 316L stainless steel BM. However, a uniform distribution of these alloying elements is observed throughout the FZ.

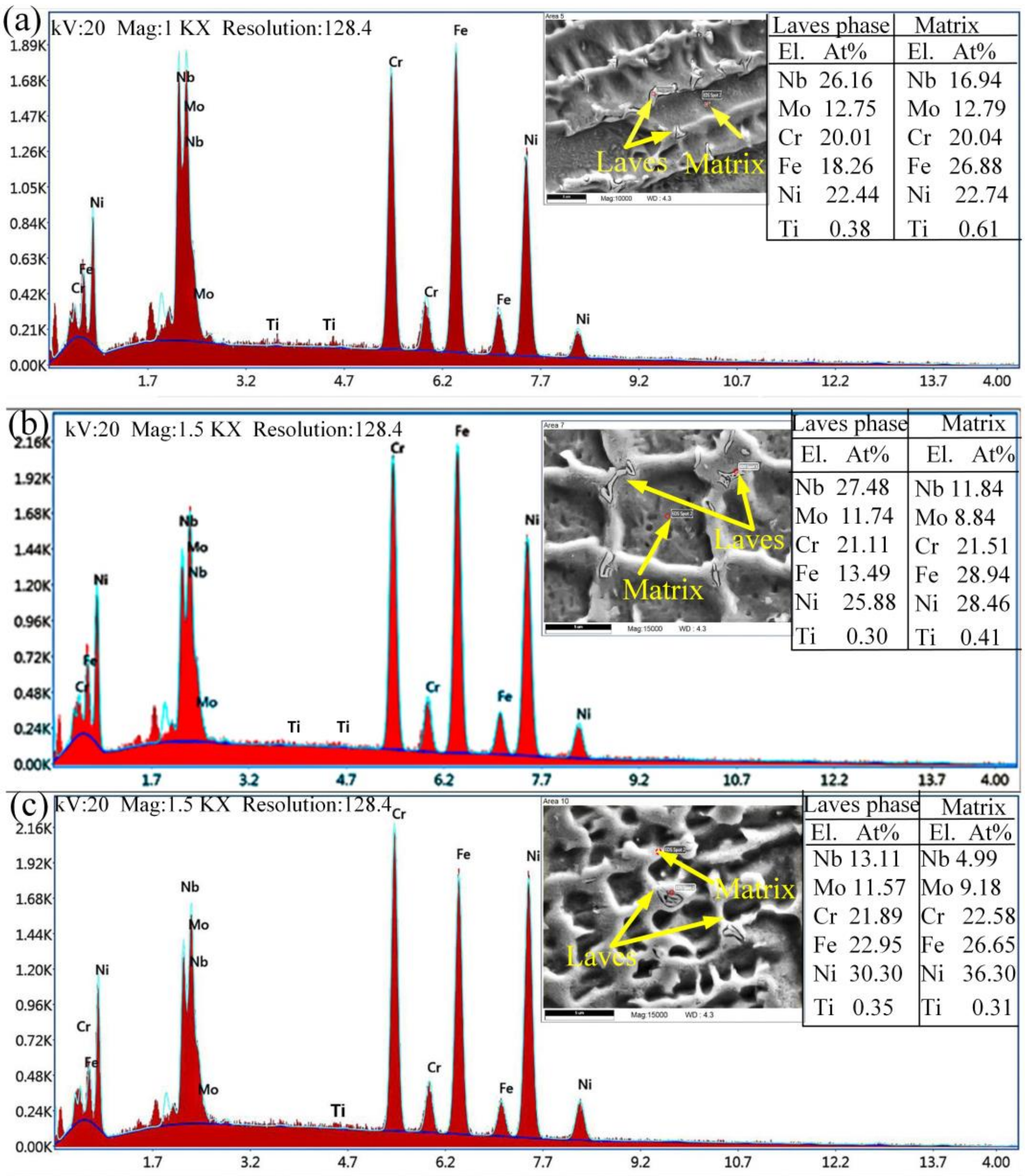

Fig. 6.3 EDX point analysis of (a) 316L-FZ interface (b) FZ center and (c) FZ-Inconel 625 interface

The magnified FESEM images of the FZ region reveals that there are many irregular shaped phases deposited throughout the interdendritic region. These phases are identified as A_2B (A: Ni, Cr, Fe; B: Mo, Ti, Nb) type secondary Laves phases, which is confirmed by

EDX point analysis (Xu et al., 2013). It is well known that Nb and Mo have a larger atomic radius than the other constituent elements. Hence, these elements are segregated at the grain boundaries during solidification and stimulate the formation of Laves phases (Sayyar et al., 2020). Moreover, due to the dissimilar joining of 316L stainless steel and Inconel 625 the percentage of iron at the FZ is increased and the chance of Laves formation is increased (Floreen et al., 1994). The Laves phase is generally brittle in nature, which leads to reduction in ductility, fatigue, and creep rupture properties of the joint.

Table 6.1 Average Wt.% of alloying elements in different locations of the welded joint

Location	Fe	Ni	Cr	Mo	Nb	Ti	Al	Si	S
316L (BM)	68.6	8.9	17.7	2.1	_	_	0.1	0.4	0.1
316L/FZ interface	32.6	29.7	17.9	10.9	3.3	_	_	_	_
FZ center	31.6	30.0	18.4	10.1	3.7	0.42	2.0		
FZ/Inconel 625	18.4	38.0	19.9	13.2	4.9	0.38			
Inconel 625 (BM)	3.8	63.2	22.9	6.6	2.6	0.3	0.2	0.2	0.2

An EDS line scan (Fig. 6.4) is also performed along the cross section of the weld bead by covering the two BMs and the FZ. A remarkable variation of Fe and Ni are observed at the interfaces of 316L/FZ and FZ/Inconel. Fe and Ni have a small atomic radius compared to other alloying elements, which helps them to diffuse easily in the molten weld pool. Moreover, an asymmetric Marangoni convection creates uniform of Ni and Fe at the FZ is.

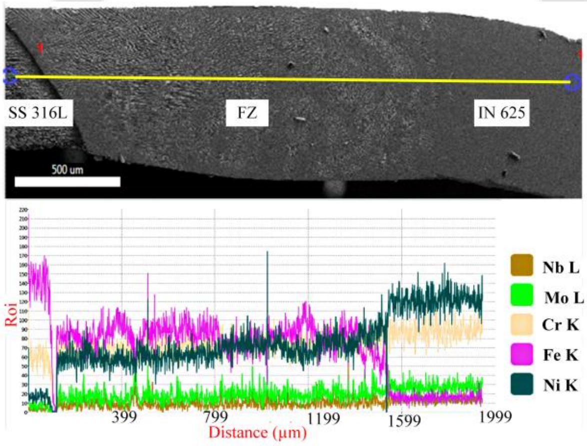

Fig. 6.4 EDX line analysis along the cross section of weld joint by covering FZ and two BMs

6.3 X-ray diffraction analysis

The phases present in the base metals of 316L stainless steel and Inconel 625 and the FZ are determined by XRD analysis and confirmed by using standard JCPDS card numbers (00-23-0298, 00-54-0331, 01-081-6808, 049-1427, 01-071-9888, 01-071-9886), shown in Fig. 6.5. There are two major phases detected in the XRD pattern of 316L stainless steel *i.e.*, FCC austenite (γ_{Fe}) matrix and BCC ferrite (δ_{Fe}) in (111) and (110) planes. The Inconel 625 has FCC Ni (γ_{Ni}) matrix in (111), (200), (220), (311) and (220) preferred crystal orientation and there are also lots of small peaks are present, which indicates the presence some secondary phases like γ"-Ni_3Nb and carbide precipitates (NbC). It is also observed that the XRD pattern of the FZ is almost similar to the XRD pattern of Inconel 625 BM. However, a small peak of δ-ferrite (δ_{Fe}) in the (110) plane is found at the FZ. The FZ is formed by the joining of two dissimilar materials *i.e.*, 316L stainless steel and Inconel 625 and the δ_{Fe} and austenite is the two major phases in 316L stainless steel. Thus, this extra δ_{Fe} comes from the 316L stainless steel after welding. According to the XRD results, there is no evidence for the formation of any intermetallic phases in the FZ. During the MPAW, the weld bead cools down very fast and also adequate quantity of shielding inert gas is used. As a result, most solid solution strengthening elements like Mo and Nb stay in the solid solution of the γ_{Ni} matrix, and chances of intermetallic phase formation is reduced.

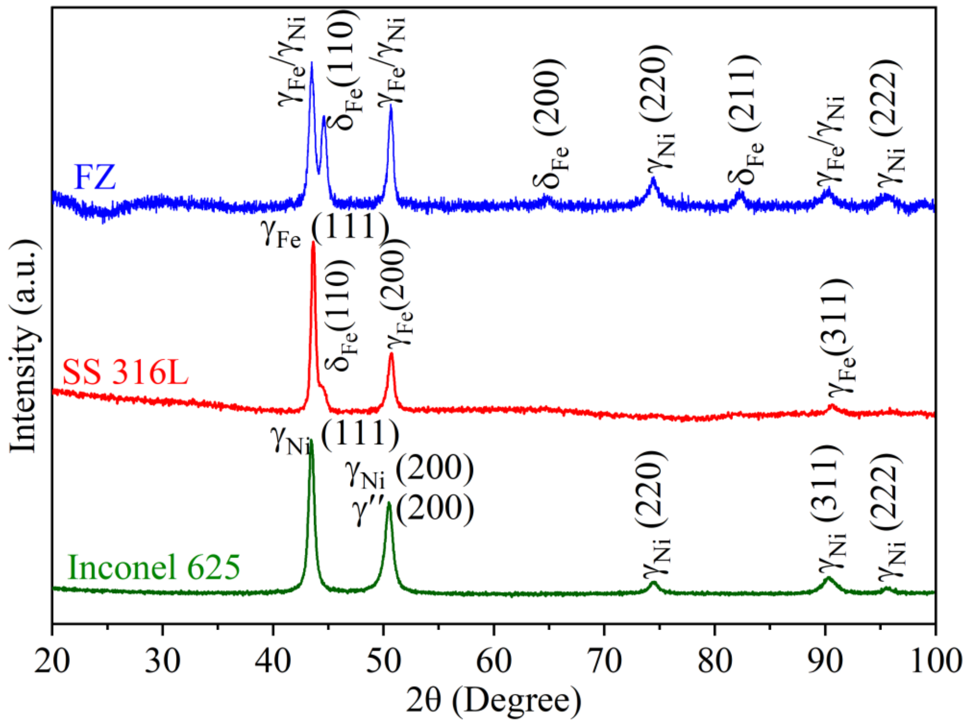

Fig. 6.5 XRD pattern of Inconel 625, 316L stainless steel base materials and FZ

6.4 TEM analysis

The complete information on the structural properties is ascertained using TEM analysis, which also identifies the various particles present in the FZ. A high-resolution TEM is used to examine the presence of different phases. It is observed from Fig. 6.6 (a) that many phases like Cr_3C (201), NbC (200), and Ni_3Nb (γ" in (220) plane) are distributed over the γ-matrix, which is confirmed by selected area diffraction (SAED) analysis. Dynamic recrystallization is also observed at the FZ, shown in Fig. 6.6 (b). To prevent static recrystallization resulting from high cycle temperature, some parallel band-like structures are visualized at the FZ (Ganka Zlateva and Zlatanka Martinova, 2008).

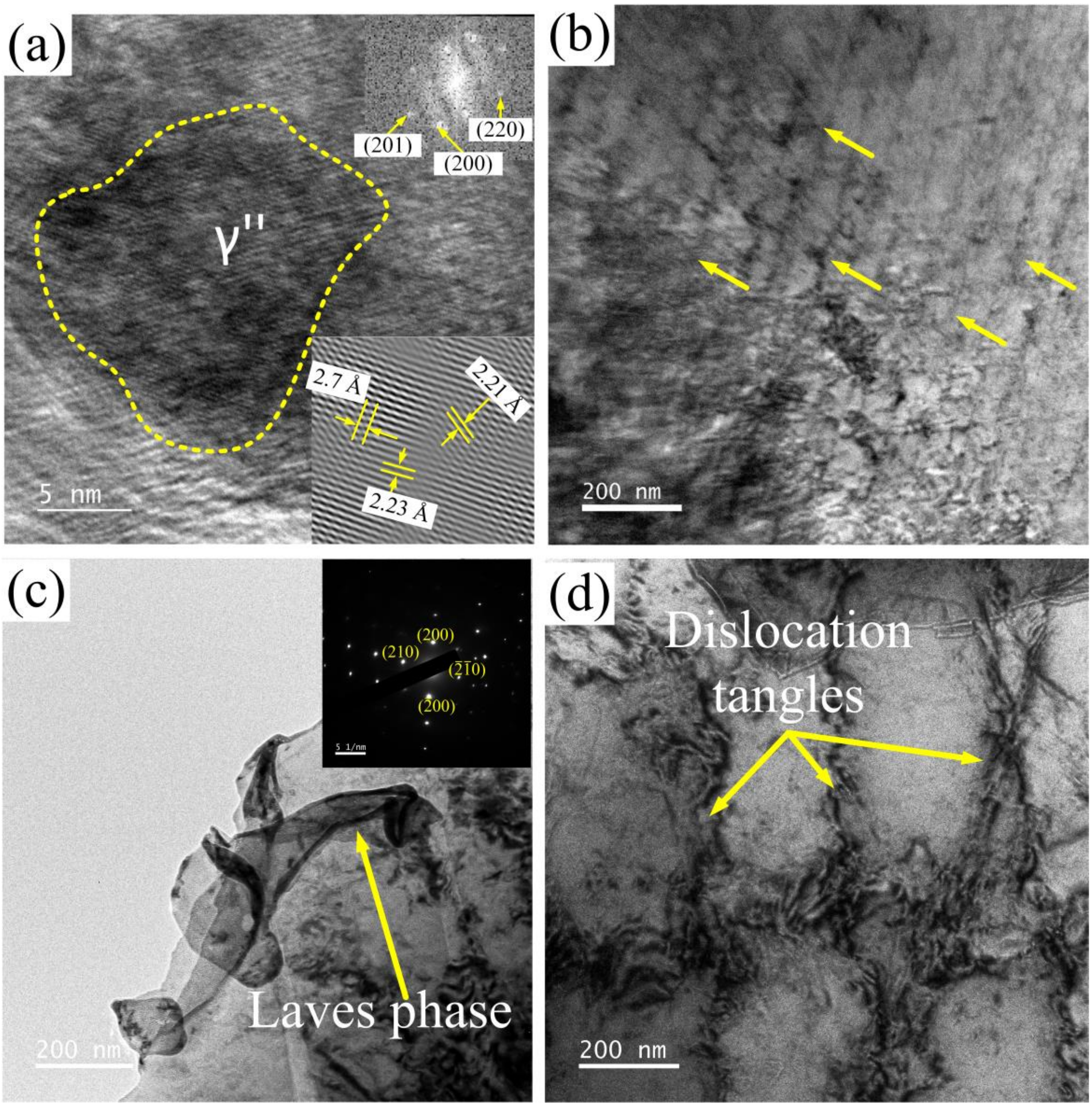

Fig. 6.6 (a) The HRTEM micrograph of the highlighted region (b) evident of dynamic recrystallization and (c)-(d) particles present at the FZ

An irregular shape precipitate is observed in Fig. 6.6 (c), confirmed as Laves phase (Ni_2Nb) by SAED analysis. It has complex crystal structures in (210) and (200) planes. These Nb-enriched Laves are interconnected with each other inside the dendritic structure. Presence of such phases the weld joint becomes more brittle and harder than other part of the welded blank. Which, has severe effect on the formability of the welded blank and chance of failure may be triggered from these phases. During the welding operation the workpiece experienced with first heating and cooling thermal cycle. As a result of this many dislocation lines (dislocation tangles) are accumulated at the boundary of the cellular structure, as mentioned in Fig. 6.6 (d). This type of crystal defect provides an obstacle against the crack propagation inside the grain of the FZ (Chen et al., 2020).

Figure 6.7 (a-c) represents the bright field images of different types of spherical and needle-like carbide particles at the FZ, their corresponding EDX spectrographs are shown in Fig. 6.7 (a'-c').

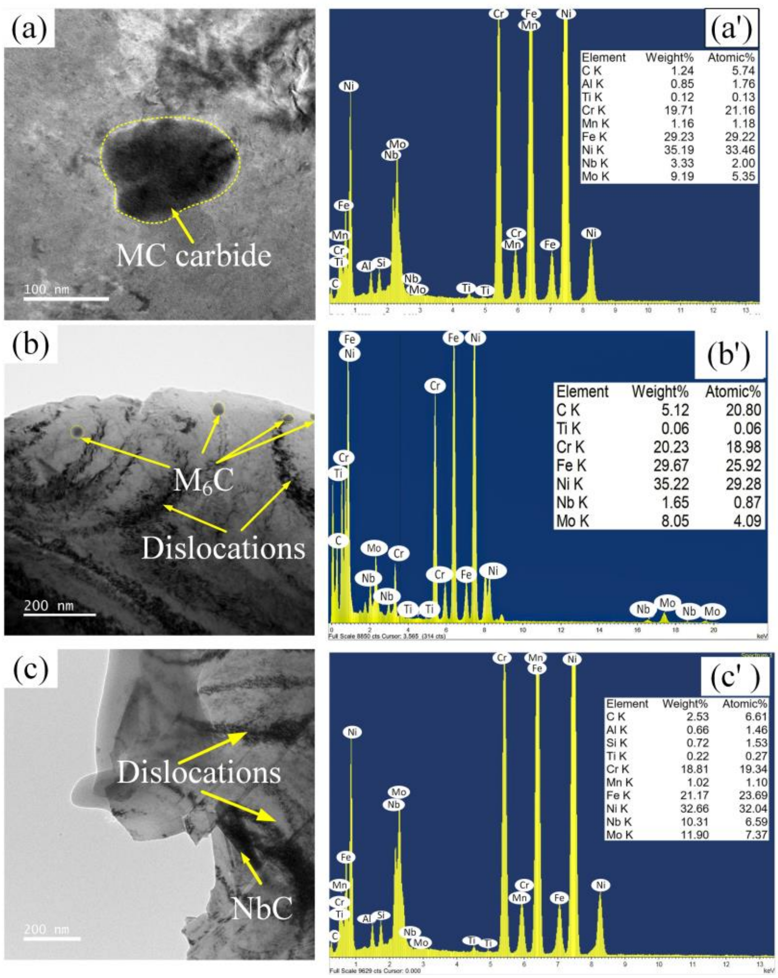

Fig. 6.7 (a-c) Bright field image of precipitates and (a'-c') corresponding EDX spectrums

The EDX results confirmed that these particles are MC, M_6C, and NbC types of carbide. These types of carbides are generally formed due to the eutectic reaction with the γ matrix at the end of solidification after welding. Most of the precipitates are enriched with Cr, Mo, and Nb hard alloying elements. A larger size (~130 nm) MC carbide is found near the epitaxial grain boundaries, and a small size (~30.7) M_6C carbide is at the FZ center. These larger size carbides are sometimes responsible for failure.

6.5 Micro hardness analysis

A Vickers micro hardness tester is employed to measure the hardness and its distribution through the thickness of the weld cross section. Figure 6.8 depicts the micro hardness trend of the weld bead encompassing BMs and the FZ.

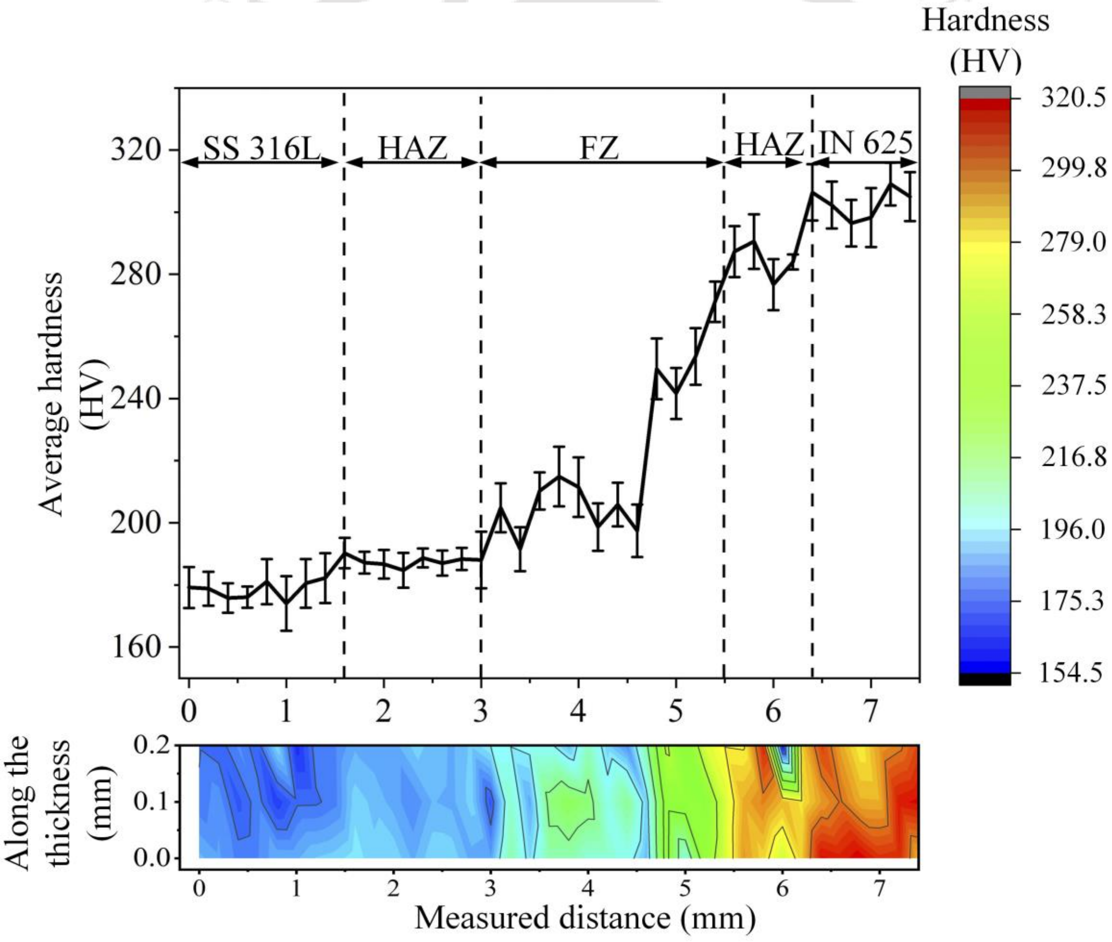

Fig. 6.8 Micro hardness profile along the cross section and through thickness of welded blank

The FZ displayed a higher hardness value of 214.92 ± 3 HV compared to the 316L stainless steel hardness value of 182.21 ± 5 HV. In Inconel 625 side, a significantly higher hardness was observed in the HAZ and BM zones. The average hardness value of Inconel 625 was 309.05 ± 5.7 HV, the highest in comparison to other regions. This is because hardness of parent Inconel 625 material is much higher than the 316L stainless steel, and thus a sharp hardness peak difference (~126.84 HV) is observed between 316L stainless steel and Inconel 625. The percentage of nickel at the FZ is higher than the BM of 316L stainless steel, but not more than that of Inconel 625, and it also contains few solid solution strengthening alloying elements and precipitations. As a result, the FZ hardness was found higher than the 316L stainless steel. However, the hardness inside the FZ is inconsistent, which may be related to convection phenomena in the weld pool and the variations in the supersaturation of strengthening elements like Nb and Mo in the γ-matrix. The width of the FZ is found as 2.5 mm from the hardness profile of the welded blank.

6.6 Tensile test and fractography analysis

The engineering and true stress-strain curves of the BMs, and welded blank are compared in Fig. 6.9 (a-b), and the averaged tensile properties are tabulated in Table 6.2. The obtained UTS of the welded blank is 67% of Inconel 625 and 94% of 316L stainless steel. It is observed from the elongated grids printed on the test samples, that the 316L stainless steel side elongated more than the Inconel 625 side during the tensile test of the welded blank. The welded blank elongation is obtained 30%, which is almost equal to the Inconel 625 elongation. However, The FZ does not behave as weakest zone of the welded tensile specimen. Presence of different types of precipitates and uniform mixing of different alloying elements like Nb, Mo and Cr, the FZ become stronger and increased the hardness value which is discussed earlier. As a result of this failure location is shifted away from the FZ and toward the transition zone of 316L stainless steel side (Fig. 6.10 (a)). The EDX analysis shows that there is a remarkable element variation in the partially melted zone. Because of the non-homogeneity of alloying elements, transition zone on the 316L stainless steel side become the weakest zone as compared with the other zones. As a result, all welded tensile specimens are failed in this zone.

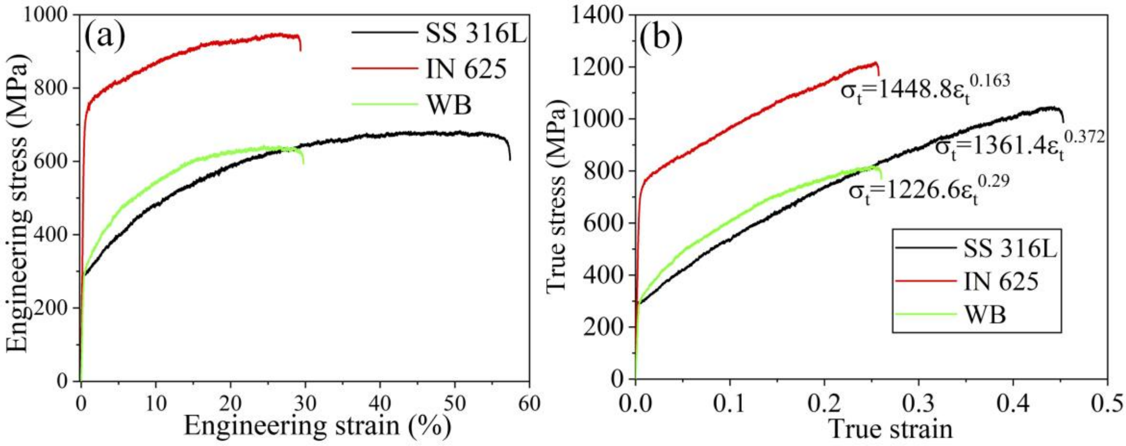

Fig. 6.9 (a) Engineering and (b)True stress-strain curves for BMs and WB

The true stress-strain data within the plastic region is fitted according to Hollomon's strain hardening law, and the hardening equations of BMs and the welded blank are evaluated and represented in Fig. 6.9 (b). It is found that 316L stainless steel and Inconel 625 have maximum and minimum strain hardening exponent (n) values, respectively, and the welded blank has a medium n-value. It is to be noted that a higher n-value is preferable for sheet metal forming.

Table 6.2 Experimental results of uniaxial properties of the BMs and welded specimen

Sample	YS (MPa)	UTS (MPa)	Elongation (%)	K-value	*n*-value
316L	293 ± 7	682 ± 2	58 ± 4	1353 ± 10.2	0.37 ± 0.02
Inconel 625	718 ± 5	949 ± 6	30.4 ± 1	1481 ± 5.5	0.16 ± 0.01
MPAWB	295 ± 1	643 ± 11	30.5 ± 5	1239 ± 1.8	0.30 ± 0.05

A detailed fractography analysis is carried out on the fracture surface of the tensile specimen of welded blank. Figure 6.10 (b) represents the fracture surface morphology which consists of multiple voids and deep dimples, it indicates that the joint has good ductility. The EDX report of different locations on the fracture surface is mentioned in Fig. 6.10 (c). The particles inside the voids are found as Cr rich particles. This observation indicates that the cohesive force between the γ-matrix and the solid solution strengthening elements (Cr, Mo, Ti) at the transition zone is less. Because of this reason, different precipitates separate easily from the primary matrix at the time of deformation.

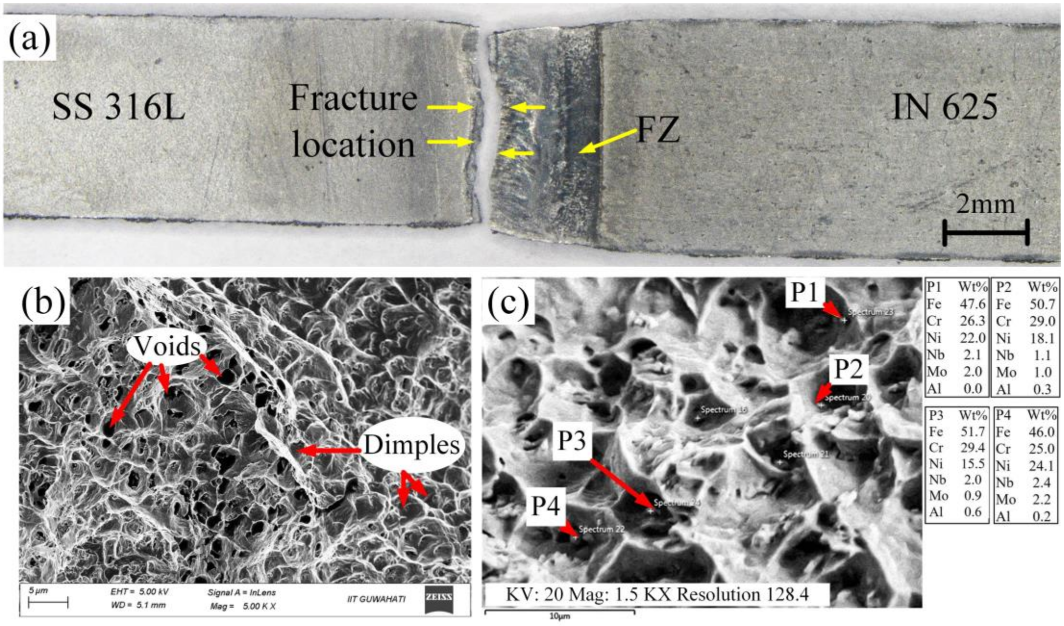

Fig. 6.10 (a) Enlarge view of the fracture location (b) Fractography and (c) EDX point analysis of the tensile fracture specimen

The elemental mapping of the fracture surface is shown in Fig. 6.11, which indicates the presence of a higher amount of Fe and Cr. As discussed earlier that the higher quantity of Fe helps to form Laves phase. Hence, the TZ, located near the 316L stainless steel BM is found with a comparatively higher amount of Laves phase. These Laves phases play a key role in fracture initiation by providing preferable sites for micro voids creation. Thus, the failure of the welded blank is taken place from the TZ.

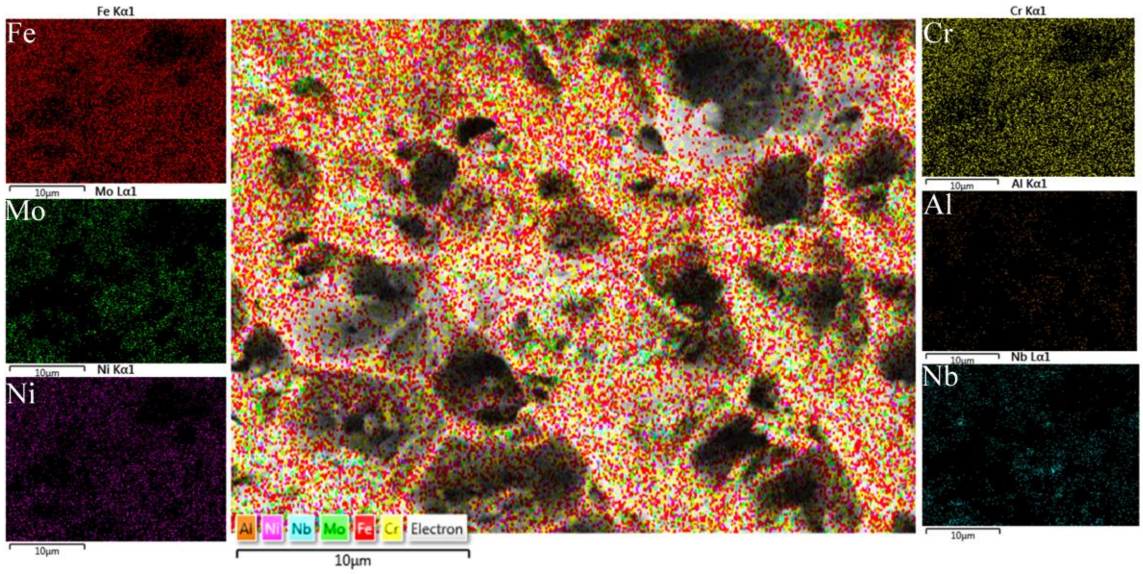

Fig. 6.11 EDX mapping of the tensile fracture surface of the welded blank

6.7 Formability study

6.7.1 Limiting dome height and fracture comparison

The limiting dome height (LDH) test is carried out using a laboratory scale stretch forming setup. The LDH of the BMs and welded blanks of full size S1 (80 mm × 80 mm) specimen is measured in both the dry and lubricated condition by using a height gauge vernier (0.001 mm least count) and mentioned in Table 6.3. A significant difference in LDH is observed among the BMs and welded blank. The LDH of the welded blank is drastically reduced by 45.77% compared to 316L stainless steel and 30.92% compared to Inconel 625 in dry condition. Due to rapid cooling, the microstructure of the FZ modified from equiaxed to fine dendritic structure which may be responsible for the increase of hardness. Moreover, as found in the TEM analysis, precipitation of NbC, MC, and M6C within the FZ also increases hardness. The increase of hardness is mainly responsible for the reduction of LDH in the welded blank. However, in lubricated conditions, approximately 6.8% LDH improvement is achieved for the welded blank. Due to the presence of lubrication, a less frictional force is exerted between the punch and blank during the forming operation. As a result of this, the LDH of the BMs and welded blank are increased as compared with the dry condition.

Table 6.3 Limiting dome height of BMs and welded blanks in dry and lubricated condition

Specimen	Dry (mm)	Lubricated (mm)
316L	12.3 ± 0.09	16.3 ± 0.05
Inconel 625	9.7 ± 0.05	11.54 ± 0.02
Welded blank	6.7 ± 0.47	7.16 ± 0.1

The measured experimental load and punch movement data of S1 specimens are plotted as a load-displacement (L-D) curve (Fig. 6.12) to make a comparison between the BMs and welded blank. A similar trend is observed for all the specimens in the L-D curve. However, the slope of the L-D curve of the welded blank is found higher than the 316L stainless steel in both the dry and lubricated condition. As the welded blank has lesser *n*-value and higher yield point than the 316L stainless steel, the welded blank can resist more stress than the 316L stainless steel. Thus, the slope of welded blank is shifted above the 316L stainless steel BM during the LDH test. On the other hand, the load required for Inconel 625 is higher than the 316L stainless steel and welded blank in both dry and lubricated conditions due to similar reason. Moreover, solid solution strengthen Inconel 625 has higher strength and hardness values than the stainless steel and welded blank, hence load required for this specimen is maximum.

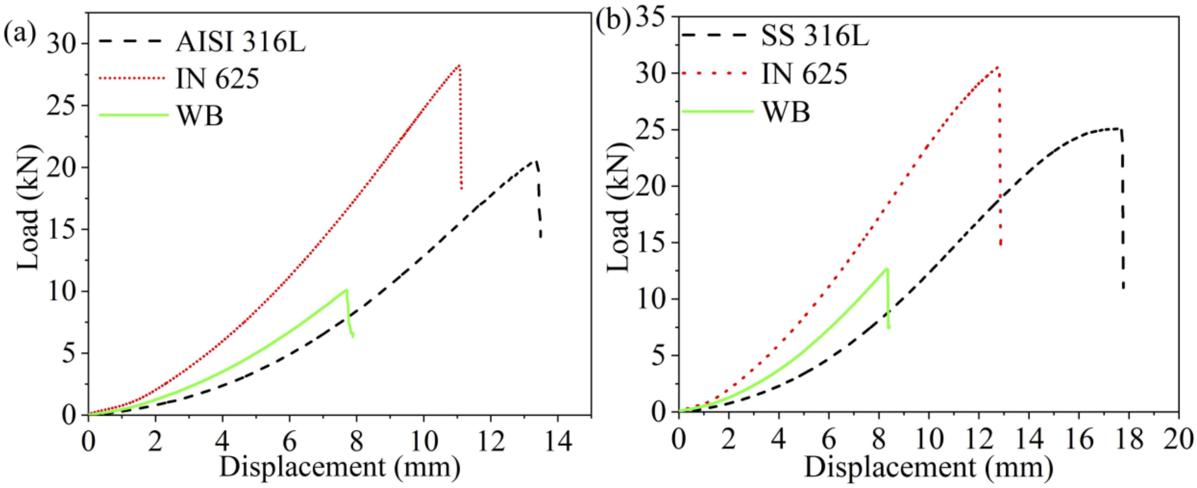

Fig. 6.12 Experimental load-displacement curve for the BMs and welded blank (a) dry and (b) lubricated condition

The maximum load required in lubricated condition is more than the dry condition for all the specimens. As in lubricating condition, the punch penetrates more into the blank, hence higher force is required for larger deformation. It is found that the punch movement for welded blank is approximately 8 mm and the force required to stretch the sample is 41.35% of Inconel 625 and 50.45% of 316L stainless steel in lubricated condition

The fracture locations of the welded blank and the BMs are evaluated and shown in Figs. (6.13-6.14). There is a significant difference in fracture location. The uppermost point of the dome is marked as pole. Figure 6.13 represents the fractured domes of tension-compression (S6) specimens. It is observed that S6 specimen of the BMs are failed near the pole because of reduction in cross section at that particular location. On the other hand, the welded blank failed from the week partially melted zone in 316L stainless steel side, which is located exactly at the pole. EDX analysis indicated a notable disparity in the distribution of elements within the partially melted zone. This non-uniformity of alloying elements renders this zone the weakest in comparison to others. Consequently, during the LDH test, the specimen fails from this transition zone.

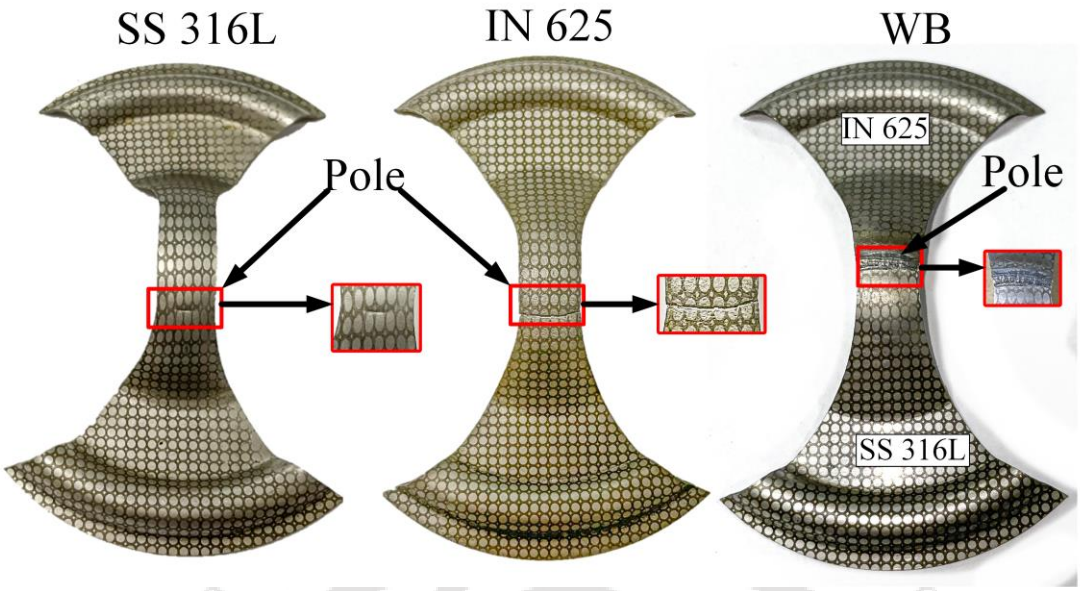

Fig. 6.13 Stretched tension-compression specimen for the BMs and welded blank with their magnified view of fracture location

The failure location of biaxial stretched specimen (S1) for BMs and welded blank are represented in Fig. 6.14. Both the BMs are failed far from the pole and the fracture direction is transverse to the rolling direction (RD). However, the failure of S1 specimen of the welded blank follows similar trend as S6 specimen, i.e., parallel to the welding direction and from the week TZ.

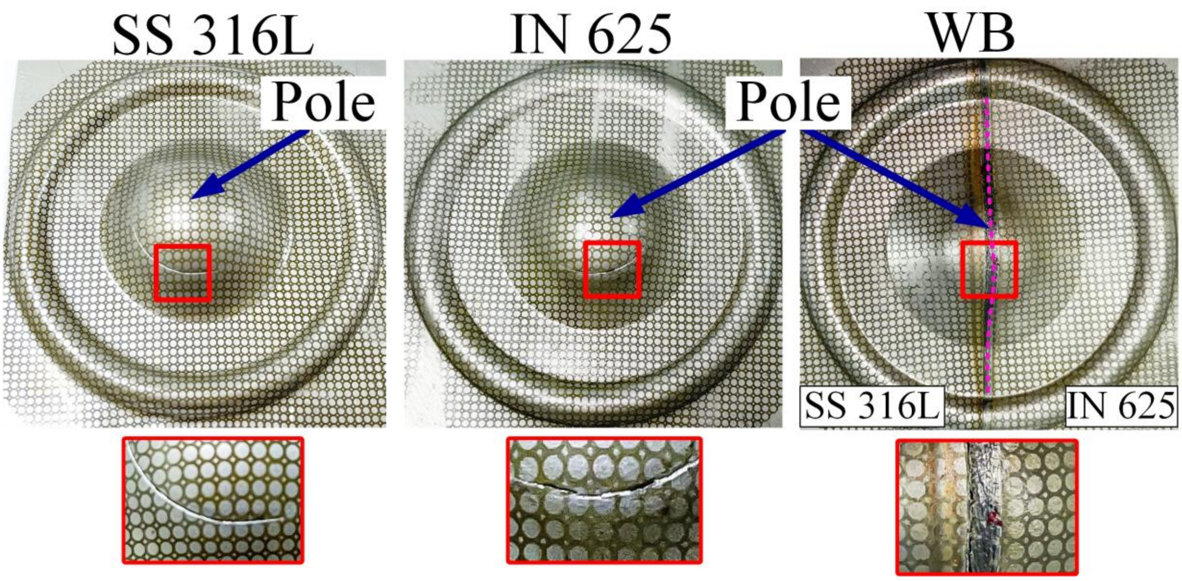

Fig. 6.14 Stretched tension-tension specimens for the BMs and welded blank with magnified view of their fracture location

A weld line shift is observed for the case of biaxial stretched S1 specimen. As the strength of Inconel 625 is more than the 316L stainless steel, the 316L stainless steel region is stretched higher than the Inconel 625 region during the LDH test of dissimilar welded blank. Hence, a few millimeters (~1.2 mm) weld line shift is observed towards the Inconel 625 side.

6.7.2 Forming limit diagram

The circles printed on the workpiece get elongated and become an ellipse after LDH test. The true major (ε_1) and minor (ε_2) strains are measured from the elongated ellipses on both sides of the fracture location of different strain path specimens and plotted as FLD in Fig. 6.15. This diagram is extremely useful for determining the global formability of sheet metal stampings. The grids near the fracture line are elongated more, considered as necking points. On the other hand, below and above of necking point is considered a safe point. A forming limit curve (FLC) is fitted between the safe and necking points to measure the limit of formability. Any strain points located above the FLC are considered at risk for failure, and below the FLC is considered safe. The measured strain ratios (β) from the elongated grids vary from the biaxial stretching region (β=1) to the uniaxial tension region (β=0.5). It is observed that the lubricated specimen (S') and S6 specimen are stretched as biaxially and uniaxially, respectively, for all the cases, and the S3 specimen is stretched near to plane strain (β=0) condition. The intersection of FLC and major strain axis is known as FLD0, and the value of FLD0 of 316L stainless steel, Inconel 625, and MPAWB are 0.44, 0.33, and 0.22, respectively. This indicates that the weld joint has comparatively less forming ability due to the presence of hard FZ. The FLCs of 316L stainless steel, Inconel 625 and welded blank are represented separately in Fig. 6.15 (d) to make a proper comparison among their formability. It can be observed that the FLC of 316L stainless steel is higher among all specimens, and the welded blank has a minimum FLC. The presence of molybdenum and low percentage of carbon in 316L stainless steel provide better ductility, which is beneficial for the forming processes. The FZ consists of hard Laves phase and metal carbides which reduces its ductility. The strength of Inconel 625 is higher than the 316L stainless steel as it is a solid-solution strengthened and precipitate hardened alloy consist of various intermetallic compounds like γ" (Ni_3Nb) γ' (Ni_3Al or Ni_3Ti) with the nickel matrix. Thus, maximum FLC is found with 316L stainless steel base metal. However, the difference of FLCs between Inconel 625 and welded blank is comparatively less.

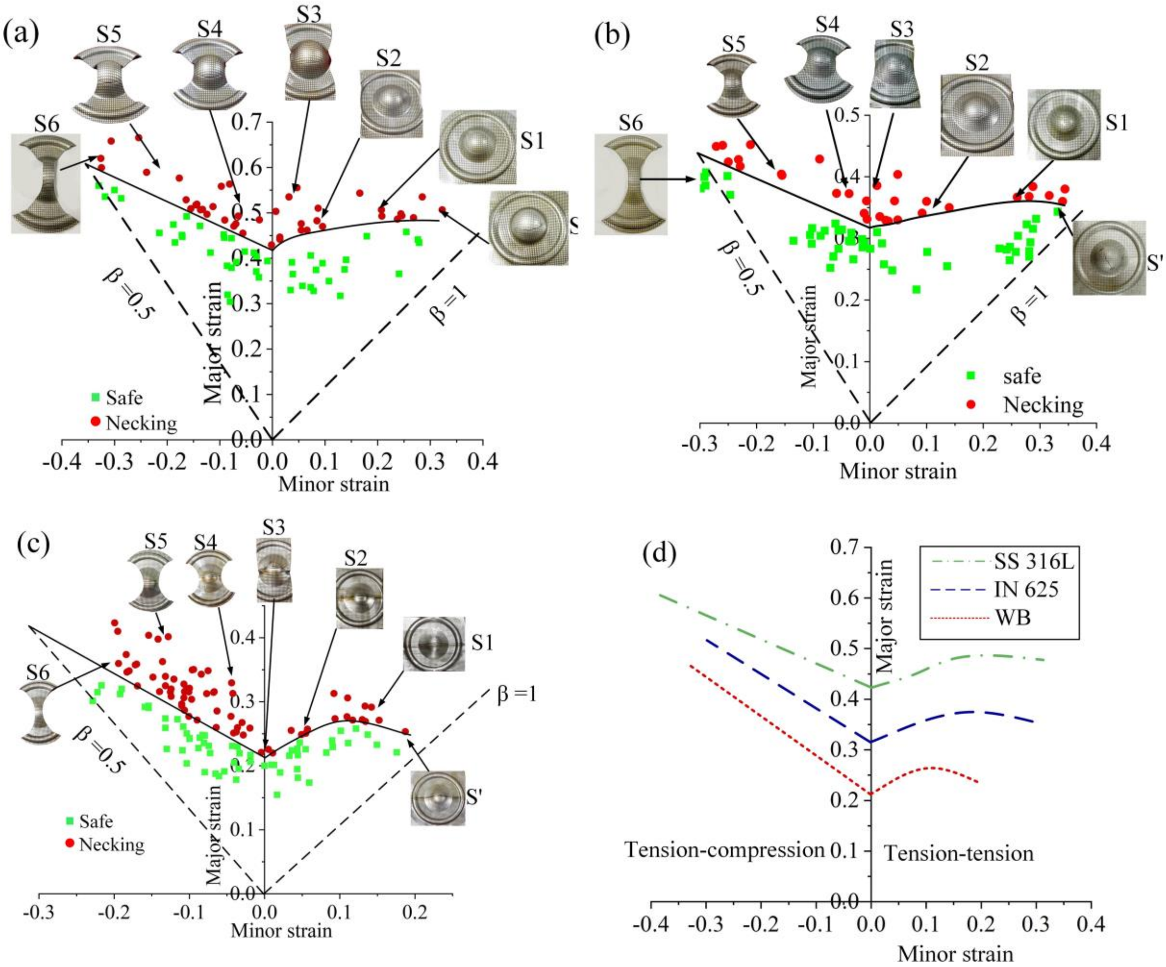

Fig. 6.15 FLD for (a) 316L stainless steel (b) Inconel 625 (c) welded blank and (d) comparison of FLC among the BMs and welded blank

6.7.3 Surface strain and thickness distribution

The logarithmic strains ($\varepsilon_1, \varepsilon_2$) are measured across the pole for the welded blank and BMs to obtain the surface strain distribution. The strain distribution profiles for the tension-tension (S1) and tension-compression (S6) specimens are shown in Fig. 6.16.

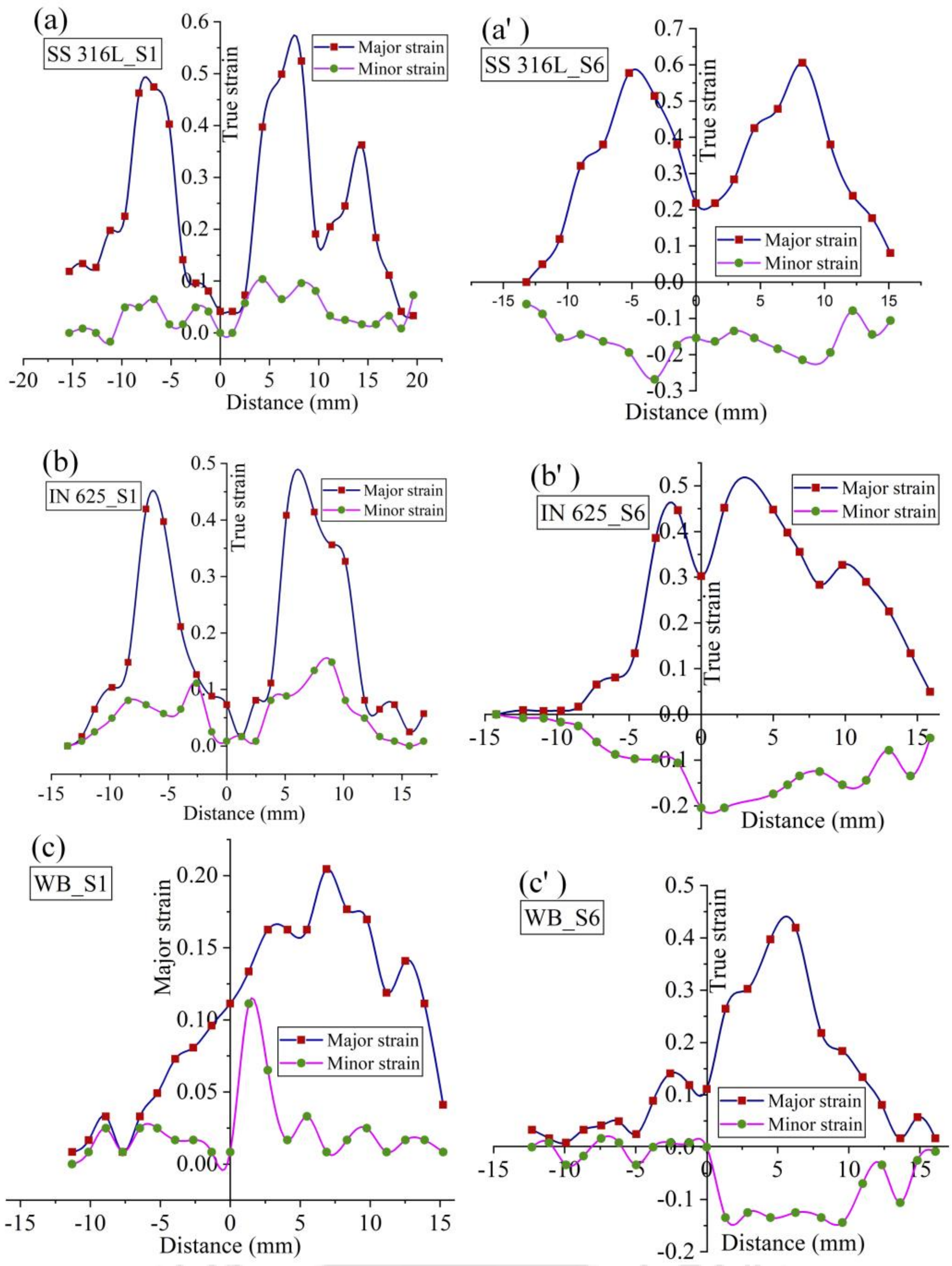

Fig. 6.16 Strain distribution profiles of 316L stainless steel, Inconel 625 and welded blank (a-c) for S1 and (a'-c') for S6 strain path specimens

Figure 6.16 (a) and (b) represents the strain distribution profile of the 316L stainless steel and Inconel 625 BMs for S1 strain path. A symmetric strain distribution profile is observed for both the BMs in which two mains sharp ε_1 peaks are observed on both side of the pole. The strain is maximum near the pole and gradually decreases far from the pole. However, a small peak height difference of ±0.08 and ±0.03 for 316L stainless steel and Inconel 625, respectively, are observed between the two peaks due to the presence of a fracture point on the locus of the strain path. It is also noticed that the center of the pole has minimum ε_1 and ε_2 strain. Figure 6.16 (a') and (b') are the strain distribution profiles of tension-compression (S6) stretched specimen of the BMs. A similar pattern is also observed in this case. However, maximum ε_1 peaks are shifted away from the pole for both the parent materials. As the S6 specimens are stretched with tension and compression, the ε_2 is found with a negative value and minimum occurs adjacent to the pole. Figure 6.16 (c) and (c') represent the strain distribution profiles of the welded blank of S1 and S6 specimens. The graph reveals that in both the S1 and S6 specimens the maximum strain occurred at the 316L stainless steel side (right side of the graph) of the welded blank. There is a strain difference of ±0.10 and ±0.30 in major direction for S1 and S6 specimens, respectively. This is because 316L stainless steel is more ductile than the FZ and Inconel 625. Regarding ε_2, the S1 sample shows the highest strain value near the pole, while the S6 sample displays the lowest strain value at the pole due to the tension-compression effect.

The stretched dome (S1) of 316L stainless steel, Inconel 625 and welded blank are cut across the fracture line and the variation of thickness, both on side of the pole, is measured by a stereo zoom microscope. The thickness distribution is compared among the BMs and welded blank and shown in Fig. 6.17.

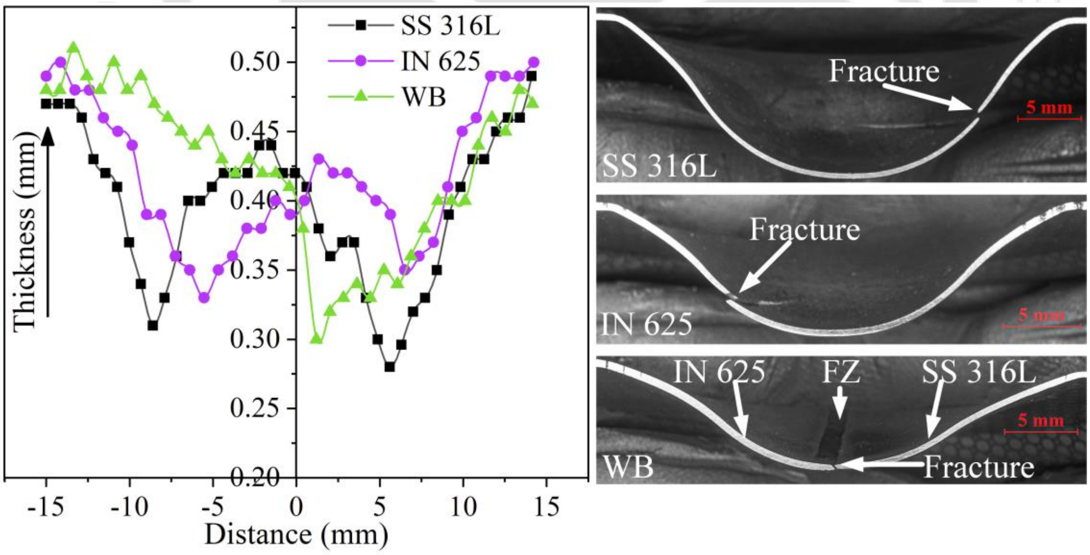

Fig. 6.17 Thickness distribution and cross-sectional view of 316L stainless steel, Inconel 625 and welded blank for S1 specimen

An un symmetric thickness distribution profile is obtained for the case of welded blank in consequence of non-uniform deformation at the time of LDH test. As a result of this the weaker 316L stainless steel side is stretched more and pushed the weld line toward the strong Inconel 625 side. Because of this reason the overall LDH of the welded blank gets reduced. On the other hand, the thickness distribution profiles of the BMs are found with symmetric on both side of the pole.

6.8 Summary

The dissimilar joining of sheets is always a challenging task due to their differences in melting temperature, thermal expansion of coefficient and thermo-mechanical properties. However, with the help of MPAW technique two dissimilar alloy sheets i.e., Inconel 625 and 316L stainless steel are joint together without any defects due to the controllable heat input at very low current range. The FZ microstructure revels that it has a homogeneous mixture of γ_{Fe} and γ_{Ni} matrices in which Mo, Nb, and Cr are distributed uniformly. The FZ exhibits greater hardness compared to the 316L stainless steel because of the existence of diverse precipitates. Substantial differences in the distribution of these alloying elements occur at the interfaces between the FZ and HAZ. The dendritic structures at the FZ contain Nb enriched brittle Laves phase, which is confirmed by EDX and TEM analysis. The MC, M_6C, and NbC carbides are also distributed inside the FZ. Because of such intermetallic phases the hardness of the FZ increases drastically. With the comparison of as received parent materials, the welded blank blank has almost 94.4% of 316L stainless steel and 67.86% of Inconel 625 joint efficiency. The MPAWB is found with 30% elongation which is 99.5% of the Inconel 625 BM. The tensile sample is predominantly failed from the interphase of FZ and HAZ due to the variation of alloying elements in large extent. The measured LDH of the 316L stainless steel, Inconel 625 and MPAWB are 16.3 mm, 11.54 mm and 7.16 mm, respectively. This reduction of LDH of the MPAWB is mainly influenced by the brittle behavior of FZ due to the presence of different types of secondary phases. 316L stainless steel is more ductile than the Inconel 625, thus during the LDH test the weld line is shifted (1.2 mm) towards the stronger Inconel 625. The failure of the stretched dome is mainly initiated from the laves phase, which is present in high percentage at the transition zone i.e., interphase of FZ and HAZ. The FLC comparison revels that the 316L stainless steel has maximum and MPAWB has minimum formability. The welded blank exhibits a non-symmetric strain distribution profile due to larger stretching of high ductile 316L stainless steel side. Whereas, both 316L stainless steel and Inconel 625 base materials exhibit symmetric strain distribution on both sides of the pole.

Chapter 7

Conclusions and future scope of the work

7.1 Conclusion of the present work

Fusion welding is the most commonly used joining technology which has wide working range from thin to thick materials. This technology has high demand in different industries like automobile, railway, shipbuilding, aerospace etc. MPAW is a most economic and trusted arc welding process for the joining of thin sheets. However, the joint quality in MPAW process mainly depends on the process parameters settings like welding current, welding speed, shielding and plasma gas flow rate, nozzle diameter, stand-off distance etc. Alloys 316 stainless steel and Inconel 625 are the most used materials in different industries due to their superior properties like high corrosion resistance form room temperature to elevated temperature and excellent mechanical properties. Similar and dissimilar joints of these materials also have huge applications. However, during welding a massive metallurgical variation takes place in the FZ. As a result of this the mechanical properties such as formability, hardness and tensile strength are affected. By using different types post welding heat treatment, the joint quality can be improved.

In this thesis a detailed study has been carried out on the similar and dissimilar MPAWB of 316L stainless steel and Inconel 625 sheets. The initial study is based on the similar joining of 316L stainless steel. In which three different types of welded samples are prepared successfully by using different combination of parameter settings. The FZ, BM, and HAZ of the welded samples are discussed through microstructural analysis to correlate the forming behavior of the welded joint. Furthermore, LDH test is carried out to differentiate the formability among the BM and MPAWBs. The second study is based on the joining of Inconel 625 using MPAW process and effect of solution treatment on the forming behaviour of the WB. The last study is based on the dissimilar joining of 316L stainless steel and Inconel 625. A detailed microstructural study is carried out to find different structures and phases present at the FZ. The LDH tests of the welded blank and BMs are also successfully conducted, and measured FLCs are compared among them. The findings derived from the current research endeavour yield several noteworthy conclusions, outlined as follows:

- The 316L stainless steel BM consists of well oriented coarse grain structure upon which δ-ferrite and annealing twins are distributed. Whereas, the FZ consists of two different types of microstructure, namely, skeletal δ-ferrite at the center and columnar dendritic structure near the transition zone.

- The XRD study reveals that the quantity of ferrite at the FZ is higher than that of the 316L stainless steel BM. TEM analysis confirms that the FZ and transition zone consist of austenite, ferrite, and some secondary phases of Cr and Si carbides. These phases are mainly responsible for embrittling the FZ.
- The LDH of 316L stainless steel is larger than that of the welded specimens in both dry and lubricated conditions. The welded biaxial specimens fail across the weld line due to higher friction between the punch and welded surfaces.
- A uniform strain distribution profile develops during formability test of S1 and S6 strain path specimens on both sides of the pole. 316L stainless steel BM shows a higher peak than the welded specimen for both the strain path specimens. The biaxial stretched samples are failed in ductile mode, which is evident by many dimples and micro voids on the fracture surface.
- The FZ of the Inconel 625 welded blank consists of long cellular and equiaxed cellular dendritic structure. The dendritic boundaries are comprised with Laves network, with some distributed NbC over the γ matrix. Because of these secondary phases, the hardness and yield strength become higher than the Inconel 625 BM and STWB.
- After solution treatment, an equiaxed homogeneous microstructure is achieved in the FZ of the Inconel 625 welded blank due to dissolution of the irregular dendritic structures. A 12.39 % higher elongation is achieved for the STWB with comparison of MPAWB.
- The Inconel 625 welded blank is having higher dislocation density than the STWB. It has direct effect on the formability of the specimens.
- The FLDs are established successfully through the experimental tests results involving deformation along six different strain paths. The solution treatment improves the formability of the welded blanks by dissolution of intermetallic and secondary phases.
- The surface strain and thickness distribution profile of S1 specimen are measured experimentally for the as-received Inconel 625 BM, MPAWB and STWB. More thinning is witnessed far from the pole for all the three cases. Maximum 42 %

thinning is found for the case of Inconel 625 BM, 33 % for the MPAWB and 38 % for the STWB.

- In dissimilar welding, the FZ consists of homogeneous mixture of γ_{Fe} and γ_{Ni} matrices in which Mo, Nb, and Cr are distributed uniformly. The hardness of FZ is higher than the 316L stainless steel base material, due to the presence of precipitates. A large variation of these alloying elements is at the interphases between the FZ and HAZs. The dendritic structures at the FZ contain Nb enriched brittle Laves phase, which is confirmed by EDX and TEM analysis. MC, M_6C, and NbC carbides are also distributed inside the FZ. The presence of such particles sharply increases the hardness of the FZ.
- The joint efficiency of the dissimilar welded blank is 94.4% and 67.86% compared to 316L stainless steel and Inconel 625 base materials, respectively, with 30% elongation. The tensile samples fail from the interphase of FZ and HAZ of 316L stainless steel base material side in ductile mode of failure due to variation of constituent elements.
- The LDH of the Inconel 625 is significantly decreased by 30.92% in the welded stretched specimen. This is due to harder and less ductile fusion zone and also presence of various secondary phases. 316L stainless steel has the highest LDH compared to Inconel 625 and welded blank. The welded blanks fracture from the transition zone, which is parallel to the joint line. FLC of the welded blank is situated beneath the FLC of all BMs due to less forming ability of the welded blank.
- The dissimilar welded blank exhibits a non-symmetric strain distribution profile due to larger stretching of high ductile 316L stainless steel BM side. Whereas, both the 316L stainless steel and Inconel 625 base materials exhibit symmetric strain distribution on both sides of the pole.

7.2 Future scope

Based on the current work, the following areas are suggested for future scope.

- It has been observed that due to welding a large metallurgical variation takes place in the FZ which may affect the corrosion behaviour of the joint. Thus, a further investigation is needed on the corrosion behaviour of the joint.
- In dissimilar welding different intermetallic are formed, which directly affects the mechanical behaviour of the joint. With the application of third material as

interlayer, this problem can be minimised. Hence, there is a great opportunity in this direction.

- It was found that the formability of the WBs are reduced by the friction between the metallic punch and the blank. The formability of the welded blanks can be improved by hydraulic or pneumatic system instead of the metallic punch. Thus, further investigation can be performed on this area.
- Deformed Inconel 625 joint can be used in cryogenic applications due to its good mechanical properties. Therefore, further investigation can be conducted in cryogenic environment.

References

Ajabshiri, M., Shamanian, M., Ashrafi, A., & Karimi, M. A. (2022). The Effect of Bonding Time on Dissimilar Joint Properties Between Inconel 625 and AISI 316L Using Transient Liquid Phase Bonding Method with Cu Interlayer. Journal of Materials Engineering and Performance, 31(4), 3311–3325. https://doi.org/10.1007/s11665-021-06411-x

Alali, M., Todd, I., & Wynne, B. P. (2017). Through-thickness microstructure and mechanical properties of electron beam welded 20 mm thick AISI 316L austenitic stainless steel. Materials and Design, 130(May), 488–500. https://doi.org/10.1016/j.matdes.2017.05.080

ALI, M., ALMALEH, A., & RASSIS, A. (2018). Studying Factors Affecting Fusion Pool Geometry of Micro Plasma Arc which Remelts Austenitic Stainless Steel Sheets (AISI 316L) by Using Response Surface Method. Journal of the Society of Materials Science, Japan, 67(6), 646–652. https://doi.org/10.2472/jsms.67.646

ASTM Committee on Mechanical Testing. (2013). Standard Test Methods for Tension Testing of Metallic Materials. ASTM International, ASTM Stds.(Designation: E8/E8M-13a), 1–28. https://doi.org/10.1520/E0008

Attique, U., Butt, S. I., Imran Jaffery, S. H., Zhang, F., & Hussain, G. (2024). Formability characterization of steel tailor welded blanks formed through single point incremental forming. Journal of Materials Research and Technology, 28(July 2023), 1941–1956. https://doi.org/10.1016/j.jmrt.2023.12.010

Badiger, R. I., Hebbale, A. M., Manjaiah, M., & Naik, G. M. (2021). A Comparative Studyon Characteristics of Inconel-625 Joints Developed through Microwave Hybrid Heating and Tungsten Inert Gas Welding. Transactions of the Indian Institute of Metals, 74(2), 531–540. https://doi.org/10.1007/s12666-021-02188-8

Badiger, R. I., Narendranath, S., Srinath, M. S., & Hebbale, A. M. (2019). Effect of Power Input on Metallurgical and Mechanical Characteristics of Inconel-625 Welded Joints Processed Through Microwave Hybrid Heating. Transactions of the Indian Institute of Metals, 72(3), 811–824. https://doi.org/10.1007/s12666-018-1537-z

Bandyopadhyay, K., Lee, M. G., Panda, S. K., Saha, P., & Lee, J. (2017). Formability assessment and failure prediction of laser welded dual phase steel blanks using anisotropic plastic properties. International Journal of Mechanical Sciences, 126(March), 203–221. https://doi.org/10.1016/j.ijmecsci.2017.03.022

Baruah, M., & Bag, S. (2016). Influence of heat input in microwelding of titanium alloy by micro plasma arc. Journal of Materials Processing Technology, 231, 100–112. https://doi.org/10.1016/j.jmatprotec.2015.12.014

Baruah, M., & Bag, S. (2017). Characteristic difference of thermo-mechanical behavior in plasma microwelding of steels. Welding in the World, 61(4), 857–871. https://doi.org/10.1007/s40194-017-0472-7

Basak, S., Katiyar, B. S., Orozco-Gonzalez, P., Baltazar-Hernandez, V. H., Arora, K. S., & Panda, S. K. (2019). Microstructure, forming limit diagram, and strain distribution of pre-strained DP-IF steel tailor–welded blank for auto body application. International Journal of Advanced Manufacturing Technology, 104(5–8), 1749–1767. https://doi.org/10.1007/s00170-019-03938-1

Batool, S., Khan, M., Jaffery, S. H. I., Khan, A., Mubashar, A., Ali, L., Khan, N., & Anwar, M. N. (2016). Analysis of weld characteristics of micro-plasma arc welding and tungsten inert gas welding of thin stainless steel (304L) sheet. Proceedings of the Institution of Mechanical Engineers, Part L: Journal of Materials: Design and Applications, 230(6), 1005–1017. https://doi.org/10.1177/1464420715592438

Bharathi, R. S., Shanmugam, N. S., Kannan, R. M., & Vendan, S. A. (2018). Studies on the Parametric Effects of Plasma Arc Welding of 2205 Duplex Stainless Steel. High Temperature Materials and Processes, 37(3), 219–232. https://doi.org/10.1515/htmp-2016-0087

Burger, S., Zinke, M., & Jüttner, S. (2021). Hot cracking tendency of flux-cored arc welding with flux-cored wires of types Ni 6625. Welding in the World, 65(3), 381–392. https://doi.org/10.1007/s40194-020-01035-6

Caiazzo, F., Alfieri, V., Cardaropoli, F., & Sergi, V. (2017). Investigation on edge joints of Inconel 625 sheets processed with laser welding. Optics and Laser Technology, 93, 180–186. https://doi.org/10.1016/j.optlastec.2017.03.011

Cao, X., Wallace, W., Poon, C., & Immarigeon, J. P. (2003). Research and progress in laser welding of wrought aluminum alloys. I. Laser welding processes. Materials and Manufacturing Processes, 18(1), 1–22. https://doi.org/10.1081/AMP-120017586

Chaudhary, J., Jain, N. K., Pathak, S., & Koria, S. C. (2019). Investigations on thin SS sheets joining by pulsed micro-plasma transferred arc process. Journal of Micromanufacturing, 251659841882047. https://doi.org/10.1177/2516598418820470

Chen, H., Li, W., Huang, Y. Y., Xie, Z., Zhu, X., Liu, B., & Wang, B. (2022). Molten pool effect on mechanical properties in a selective laser melting 316 L stainless steel at high-velocity deformation. Materials Characterization, 194(July), 112409. https://doi.org/10.1016/j.matchar.2022.112409

Chen, L., Sun, Y., Li, L., & Ren, X. (2020). Improvement of high temperature oxidation resistance of additively manufactured TiC/Inconel 625 nanocomposites by laser shock peening treatment. Additive Manufacturing, 34(January), 101276. https://doi.org/10.1016/j.addma.2020.101276

Dadfar, M. R., Fathi, M. H., Karimzadeh, F., Dadfar, M. R., & Saatchi, A. (2007). Effect of TIG welding on corrosion behavior of 316L stainless steel. Materials Letters, 61(11–12), 2343–2346. https://doi.org/10.1016/j.matlet.2006.09.008

Dai, H., Shi, S., Guo, C., & Chen, X. (2022). Stress corrosion cracking behavior of 316 L SS in HF vapor environment based on corrosion degradation as a precursor. Corrosion Science, 208(August), 110615. https://doi.org/10.1016/j.corsci.2022.110615

Dinda, S. K., Basiruddin Sk, M., Roy, G. G., & Srirangam, P. (2016). Microstructure and mechanical properties of electron beam welded dissimilar steel to Fe–Al alloy joints. Materials Science and Engineering: A, 677, 182–192. https://doi.org/10.1016/j.msea.2016.09.050

Dokme, F., Kulekci, M. K., & Esme, U. (2018). Microstructural and mechanical characterization of dissimilar metal welding of inconel 625 and aisi 316l. Metals, 8(10). https://doi.org/10.3390/met8100797

Dreshfield, R. L., Moore, T. J., & Bartolotta, P. A. (1992). Post-test Examination of a Pool Boiler Receiver Conservation and Renewable Energy. NASA, USA.

Dwibedi, S., Jain, N. K., & Pathak, S. (2018). Investigations on joining of stainless steel tailored blanks by μ-PTA process. Materials and Manufacturing Processes, 33(16), 1851–1863. https://doi.org/10.1080/10426914.2018.1476766

Feng, Y., Luo, Z., Liu, Z., Li, Y., Luo, Y., & Huang, Y. (2015). Keyhole gas tungsten arc welding of AISI 316L stainless steel. Materials and Design, 85, 24–31. https://doi.org/10.1016/j.matdes.2015.07.011

Floreen, S., Fuchs, G. E., & Yang, W. J. (1994). The Metallurgy of Alloy 625. 13–37.

Ganka Zlateva and Zlatanka Martinova. (2008). Microstructure of metals and alloys: an atlas of transmission electron microscopy images. CRC press.

Gashti, S. O., Fattah-Alhosseini, A., Mazaheri, Y., & Keshavarz, M. K. (2016). Effects of grain size and dislocation density on strain hardening behavior of ultrafine grained AA1050 processed by accumulative roll bonding. Journal of Alloys and Compounds, 658, 854–861. https://doi.org/10.1016/j.jallcom.2015.11.032

Gooch, T. G., & Honeycombe, J. (1980). Welding Variables and Microfissuring in Austenitic Stainless Steel Weld Metal. Welding Journal (Miami, Fla), 59(8), 233–241.

Goodwin, G. M. (1968). Application of Strain Analysis to Sheet Metal Forming Problems in the Press Shop. Sae Transactions, 380–387. https://doi.org/10.4271/680093

Guo, L. Q., Lin, M. C., Qiao, L. J., & Volinsky, A. A. (2013). Ferrite and austenite phase identification in duplex stainless steel using SPM techniques. Applied Surface Science, 287, 499–501. https://doi.org/10.1016/j.apsusc.2013.09.041

Guo, L., Xiao, F., Wang, F., He, Y., Wei, W., & Zhang, Y. (2021). Microstructure and Corrosion Resistance of Inconel 625 Overlay Welded by Pulsed TIG Process. International Journal of Electrochemical Science, 16(4), 1–12. https://doi.org/10.20964/2021.04.11

Guo, Q., Li, D., Guo, S., Peng, H., & Hu, J. (2011). The effect of deformation temperature on the microstructure evolution of Inconel 625 superalloy. Journal of Nuclear Materials, 414(3), 440–450. https://doi.org/10.1016/j.jnucmat.2011.05.029

Guo, S., Xu, J., Gu, J., Peng, Y., Zhou, Q., & Wang, K. (2023). Effect of cellular structure on the mechanical properties of 316L stainless steel fabricated by EBF3. Journal of Materials Research and Technology, 25, 5469–5482. https://doi.org/10.1016/j.jmrt.2023.07.024

Guzman-Aguilera, J. J., Martinez-Gonzalez, C. J., Baltazar-Hernandez, V. H., Basak, S., Panda, S. K., Razmpoosh, M. H., Gerlich, A., & Zhou, Y. (2018). Influence of SC-HAZ microstructure on the mechanical behavior of Si-TRIP steel welds. Materials Science and Engineering A, 718(January), 216–227. https://doi.org/10.1016/j.msea.2018.01.108

Hamada, A., Ali, M., Ghosh, S., Jaskari, M., Keskitalo, M., & Järvenpää, A. (2022). Mechanical performance and formability of laser-welded dissimilar butt joints between medium-Mn stainless steel and high-strength carbon steel. Materials Science and Engineering: A, 831(July 2021), 142200. https://doi.org/10.1016/j.msea.2021.142200

Hardy, M. C., Detrois, M., McDevitt, E. T., Argyrakis, C., Saraf, V., Jablonski, P. D., Hawk, J. A., Buckingham, R. C., Kitaguchi, H. S., & Tin, S. (2020). Solving Recent Challenges for Wrought Ni-Base Superalloys. Metallurgical and Materials Transactions A: Physical Metallurgy and Materials Science, 51(6), 2626–2650. https://doi.org/10.1007/s11661-020-05773-6

Heiple, C. R., & Roper, J. R. (1981). Effect of Selenium on GTAW Fusion Zone Geometry. Welding Journal (Miami, Fla), 60(8), 143–145.

Hu, Yunlong and Lin, Xin and Li, Yunlong and Ou, Yongchao and Gao, Xuehao and Zhang, Qiang and Li, Wei and Huang, W. (2021). Microstructural evolution and anisotropic mechanical properties of Inconel 625 superalloy fabricated by directed energy deposition. Journal of Alloys and Compounds, 870(SPEC. ISS.), 159426. https://doi.org/https://doi.org/10.1016/j.jallcom.2021.159426

Hu, Y. L., Li, Y. L., Zhang, S. Y., Lin, X., Wang, Z. H., & Huang, W. D. (2020). Effect of solution temperature on static recrystallization and ductility of Inconel 625 superalloy fabricated by directed energy deposition. Materials Science and Engineering A, 772(November 2019). https://doi.org/10.1016/j.msea.2019.138711

Huang, H. Y. (2010). Research on the activating flux gas tungsten Arc welding and plasma Arc welding for stainless steel. Metals and Materials International, 16(5), 819–825. https://doi.org/10.1007/s12540-010-1020-9

J.A. Bittencourt. (2004). Fundamentals of plasma physics. In Springer Science & Business Media. http://www.nber.org/papers/w16019

Javidrad, F., Farghadani, H., & Hedari, M. (2014). The MPAW of Ti-3Al-2.5V thin sheets and its effects on mechanical and microstructural properties. Journal of Materials Engineering and Performance, 23(2), 666–672. https://doi.org/10.1007/s11665-013-0785-7

Jelokhani-Niaraki, M. R., B. Mostafa Arab, N., Naffakh-Moosavy, H., & Ghoreishi, M. (2016). The systematic parameter optimization in the Nd:YAG laser beam welding of Inconel 625. International Journal of Advanced Manufacturing Technology, 84(9–12), 2537–2546. https://doi.org/10.1007/s00170-015-7833-4

John C. Lippold, D. J. K. (2005). Welding metallurgy and weldability of stainless steels (WILEY). John wiley and sons.

Kale, A. B., Alluri, P., Singh, A. K., & Choi, S. H. (2021). The deformation and fracture behavior of 316L SS fabricated by SLM under mini V-bending test. International Journal of Mechanical Sciences, 196(January), 106292. https://doi.org/10.1016/j.ijmecsci.2021.106292

Kannan, A. R., Sankarapandian, S., Pramod, R., & Shanmugam, N. S. (2021). Experimental and numerical studies on the influence of formability of AISI 316L tailor-welded blanks at different weld line orientations. Journal of the Brazilian Society of Mechanical Sciences and Engineering, 43(3), 1–26. https://doi.org/10.1007/s40430-021-02896-8

Karami, V., Dariani, B. M., & Hashemi, R. (2021). Investigation of forming limit curves and mechanical properties of 316 stainless steel/St37 steel tailor-welded blanks produced by tungsten inert gas and friction stir welding method. CIRP Journal of Manufacturing Science and Technology, 32, 437–446. https://doi.org/10.1016/j.cirpj.2021.02.002

Kashani, H. T., Kah, P., & Martikainen, J. (2015). Laser Overlap Welding of Zinc-coated Steel on Aluminum Alloy. Physics Procedia, 78(August), 265–271. https://doi.org/10.1016/j.phpro.2015.11.037

Katiyar, B. S., Panda, S. K., & Saha, P. (2021). Quasi-static crushing behavior of stretch formed domes of laser welded tailored blanks. Thin-Walled Structures, 159(July 2020), 107288. https://doi.org/10.1016/j.tws.2020.107288

Keeler, S. P. (1961). Plastic instability and fracture in sheets. ASM Trans, 56, 25–48. http://hdl.handle.net/1721.1/120282

Kourdani, A., & Derakhshandeh-Haghighi, R. (2018). Evaluating the Properties of Dissimilar Metal Welding Between Inconel 625 and 316L Stainless Steel by Applying Different Welding Methods and Consumables. Metallurgical and Materials Transactions A: Physical Metallurgy and Materials Science, 49(4), 1231–1243. https://doi.org/10.1007/s11661-018-4469-7

Kulkarni, A., Dwivedi, D. K., & Vasudevan, M. (2020). Microstructure and mechanical properties of A-TIG welded AISI 316L SS-Alloy 800 dissimilar metal joint. Materials Science and Engineering A, 790(May), 139685. https://doi.org/10.1016/j.msea.2020.139685

Kumar, A., Gautam, V., & Kumar, D. R. (2018). Maximum Bulge Height and Weld Line Displacement in Hydroforming of Tailor Welded Blanks. Journal of Manufacturing Science and Engineering, Transactions of the ASME, 140(3), 1–14. https://doi.org/10.1115/1.4038513

Kumar, B., Bag, S., Paul, C. P., Das, C. R., Ravikumar, R., & Bindra, K. S. (2020). Influence of the mode of laser welding parameters on microstructural morphology in thin sheet Ti6Al4V alloy. Optics and Laser Technology, 131(May), 106456. https://doi.org/10.1016/j.optlastec.2020.106456

Kumar, K. G., Ramkumar, K. D., & Arivazhagan, N. (2015). Characterization of metallurgical and mechanical properties on the multi-pass welding of Inconel 625 and AISI 316L. Journal of Mechanical Science and Technology, 29(3), 1039–1047. https://doi.org/10.1007/s12206-014-1112-4

Lampman, S. (Ed.). (1997). Weld Integrity and Performance. ASM International.

Landowski, M., Świerczyńska, A., Rogalski, G., & Fydrych, D. (2020). Autogenous fiber laser welding of 316L austenitic and 2304 lean duplex stainless steels. Materials, 13(13), 1–16. https://doi.org/10.3390/ma13132930

Lee, W., Chung, K. H., Kim, D., Kim, J., Kim, C., Okamoto, K., Wagoner, R. H., & Chung, K. (2009). Experimental and numerical study on formability of friction stir welded TWB sheets based on hemispherical dome stretch tests. International Journal of Plasticity, 25(9), 1626–1654. https://doi.org/10.1016/j.ijplas.2008.08.005

Li, C., White, R., Fang, X. Y., Weaver, M., & Guo, Y. B. (2017). Microstructure evolution characteristics of Inconel 625 alloy from selective laser melting to heat treatment. Materials Science and Engineering: A, 705(June), 20–31. https://doi.org/10.1016/j.msea.2017.08.058

Li, D., Guo, Q., Guo, S., Peng, H., & Wu, Z. (2011). The microstructure evolution and nucleation mechanisms of dynamic recrystallization in hot-deformed Inconel 625 superalloy. Materials and Design, 32(2), 696–705. https://doi.org/10.1016/j.matdes.2010.07.040

Li, J., Nayak, S. S., Biro, E., Panda, S. K., Goodwin, F., & Zhou, Y. (2013). Effects of weld line position and geometry on the formability of laser welded high strength low alloy and dual-phase steel blanks. Materials and Design, 52, 757–766. https://doi.org/10.1016/j.matdes.2013.06.021

Lin Prakash, P. S., Biswal, S. K., Roy, G. G., Jha, M. N., Mascarenhas, M., & Panda, S. K. (2018). Effect of Orientation of Weld Line on Formability of Electron Beam-Welded Dissimilar Thickness Titanium Sheets. Journal of Materials Engineering and Performance, 27(11), 5913–5925. https://doi.org/10.1007/s11665-018-3689-8

Lippold, John C and Kiser, Samuel D and DuPont, J. N. (2011). Welding metallurgy and weldability of nickel-base alloys. John Wiley & Sons.

Liu, G., Ren, N., Wang, X., Zhu, W., Hu, L., Meng, W., Yin, X., & Ma, Q. (2023). Effects of Deposition Strategies on Microstructure and Mechanical Properties of 316L Stainless Steel and Inconel 625 Alloy Dissimilar Structure Fabricated by Cold Metal Transfer Arc Additive Manufacturing. Journal of Materials Engineering and Performance, Ref 7. https://doi.org/10.1007/s11665-023-08615-9

Liu, X., Li, Y., Song, Y., Yang, S., Yao, L., & Li, Y. (2023). Microstructure Evolution During Annealing of Inconel 625 and the Effect of Partially Recrystallized Structure on Mechanical Properties. Transactions of the Indian Institute of Metals, 76(8), 2043–2053. https://doi.org/10.1007/s12666-022-02865-2

Liu, Z. M. (2015). Keyhole Behaviors Influence Weld Defects in Plasma Arc Welding Process. Welding Journal, 94(9), 281–290.

Liu, Z. M., Wu, C. S., & Chen, M. A. (2014). Experimental sensing of the keyhole exit deviation from the torch axis in plasma arc welding. International Journal of Advanced Manufacturing Technology, 71(5–8), 1209–1219. https://doi.org/10.1007/s00170-013-5568-7

Lucas, W. (1990). Tig and Plasma Welding. Woodhead Publishing Limited.

Marchese, G., Lorusso, M., Parizia, S., Bassini, E., Lee, J. W., Calignano, F., Manfredi, D., Terner, M., Hong, H. U., Ugues, D., Lombardi, M., & Biamino, S. (2018). Influence of heat treatments on microstructure evolution and mechanical properties of Inconel 625 processed by laser powder bed fusion. Materials Science and Engineering: A, 729(July 2017), 64–75. https://doi.org/10.1016/j.msea.2018.05.044

Martikainen, J. K., & Moisio, T. J. I. (1993). Investigation of the Effect of Welding Parameters on Weld Quality of Plasma-Arc Keyhole Welding of Structural-Steels. Welding Journal, 72(7), S329–S340.

Mataya, M. C., Nilsson, E. R., Brown, E. L., & Krauss, G. (2003). Hot working and recrystallization of as-cast 317L. Metallurgical and Materials Transactions A: Physical Metallurgy and Materials Science, 34(12), 3021–3041. https://doi.org/10.1007/s11661-003-0201-2

Mishra, R. S., & Ma, Z. Y. (2005). Friction stir welding and processing. Materials Science and Engineering R: Reports, 50(1–2), 1–78. https://doi.org/10.1016/j.mser.2005.07.001

Moayedi, H., Darabi, R., Ghabussi, A., Habibi, M., & Foong, L. K. (2020). Weld orientation effects on the formability of tailor welded thin steel sheets. Thin-Walled Structures, 149(February), 106669. https://doi.org/10.1016/j.tws.2020.106669

Mohammad Soltani, H., & Tayebi, M. (2018). Comparative study of AISI 304L to AISI 316L stainless steels joints by TIG and Nd:YAG laser welding. Journal of Alloys and Compounds, 767, 112–121. https://doi.org/10.1016/j.jallcom.2018.06.302

Mostafaei, A., Behnamian, Y., Krimer, Y. L., Stevens, E. L., Luo, J. L., & Chmielus, M. (2016). Effect of solutionizing and aging on the microstructure and mechanical properties of powder bed binder jet printed nickel-based superalloy 625. Materials and Design, 111, 482–491. https://doi.org/10.1016/j.matdes.2016.08.083

Naffakh, H., Shamanian, M., & Ashrafizadeh, F. (2009). Dissimilar welding of AISI 310 austenitic stainless steel to nickel-based alloy Inconel 657. Journal of Materials Processing Technology, 209(7), 3628–3639. https://doi.org/10.1016/j.jmatprotec.2008.08.019

Narayanan, R. G., & Narasimhan, K. (2008). Influence of the weld conditions on the forming-limit strains of tailor-welded blanks. Journal of Strain Analysis for Engineering Design, 43(4), 217–227. https://doi.org/10.1243/03093247JSA344

Ogborn, J. S., Olson, D. L., & Cieslak, M. J. (1995). Influence of solidification on the microstructural evolution of. Materials Science and Engineering A, 203, 134–139.

Park, M., & Hirata, Y. (2017). Research on generation of micro-plasma arc and its power intensity. Welding International, 31(4), 284–290. https://doi.org/10.1080/09507116.2016.1223214

Pramod, R., Mohan Kumar, S., Shanmugam, N. S., & Vendan, S. A. (2020). Formability studies on plasma arc welded duplex stainless steel 2205 sheet. Materialwissenschaft Und Werkstofftechnik, 51(2), 163–173. https://doi.org/10.1002/mawe.201900001

Prasad, K. S., Rao, C. S., & Rao, D. N. (2011). Prediction of Weld Pool Geometry in Pulsed Current Micro Plasma Arc Welding of SS304L Stainless Steel Sheets. Applied Sciences, 2(3), 325–336.

Prasad, K. S., Rao, C. S., & Rao, D. N. (2012a). Effect of pulsed current micro plasma arc welding process parameters on fusion zone grain size and ultimate tensile strength of Inconel 625 sheets. Acta Metallurgica Sinica (English Letters), 25(3), 179–189. https://doi.org/10.11890/1006-7191-123-179

Prasad, K. S., Rao, C. S., & Rao, D. N. (2012b). Optimizing fusion zone grain size and hardness of pulsed current micro plasma arc welded Inconel625 sheets using Hooke and Jeeves Algorithm. Multidiscipline Modeling in Materials and Structures, 8(3), 338–354. https://doi.org/10.1108/15736101211269140

Prasad, S., Pal, S., & Robi, P. S. (2020). Analysis of weld characteristics of micro plasma arc welded thin stainless steel 306 L sheet. Journal of Manufacturing Processes, 57(January), 957–977. https://doi.org/10.1016/j.jmapro.2020.07.062

Prasada, K., Rao, C., & Rao, D. (2012). Optimizing pulsed current micro plasma arc welding parameters to maximize ultimate tensile strength of Inconel625 Nickel alloy using response surface method. International Journal of Engineering, Science and Technology, 3(6), 226–236. https://doi.org/10.4314/ijest.v3i6.18

Ragavendran, M., & Vasudevan, M. (2021). Effect of Laser and Hybrid Laser Welding Processes on the Residual Stresses and Distortion in AISI Type 316L(N) Stainless Steel Weld Joints. Metallurgical and Materials Transactions B: Process Metallurgy and Materials Processing Science, 52(4), 2582–2603. https://doi.org/10.1007/s11663-021-02202-w

Rahimi, A., Shamanian, M., Rahimi, A., & Kangazian, J. (2018). A Comparative Study on Direct and Pulsed Current Micro-plasma Arc Welding of Alloy Ti–6Al–4V. Transactions of the Indian Institute of Metals, 71(12), 3103–3110. https://doi.org/10.1007/s12666-018-1501-y

Raj, S., & Biswas, P. (2023). Experimental investigation of the effect of induction preheating on the microstructure evolution and corrosion behaviour of dissimilar FSW (IN718 and SS316L) joints. Journal of Manufacturing Processes, 95(February), 143–159. https://doi.org/10.1016/j.jmapro.2023.04.021

Ramkumar, K. D., Mulimani, S. S., Ankit, K., Kothari, A., & Ganguly, S. (2021). Effect of grain boundary precipitation on the mechanical integrity of EBW joints of Inconel 625. Materials Science and Engineering: A, 808(December 2020), 140926. https://doi.org/10.1016/j.msea.2021.140926

Ramkumar, T., Selvakumar, M., Narayanasamy, P., Begam, A. A., Mathavan, P., & Raj, A. A. (2017). Studies on the structural property, mechanical relationships and corrosion behaviour of Inconel 718 and SS 316L dissimilar joints by TIG welding without using activated flux. Journal of Manufacturing Processes, 30, 290–298. https://doi.org/10.1016/j.jmapro.2017.09.028

Rao, C. S., Prasad, K. S., & Rao, D. N. (2015). Study on Effect of Welding Speed on Micro Structure and Mechanical Properties of Pulsed Current Micro Plasma Arc Welded Inconel 625 Sheets. Journal of Minerals and Materials Characterization and Engineering, 11(10), 1027–1033. https://doi.org/10.4236/jmmce.2012.1110106

Reza Tabrizi, T., Sabzi, M., Mousavi Anijdan, S. H., Eivani, A. R., Park, N., & Jafarian, H. R. (2021). Comparing the effect of continuous and pulsed current in the GTAW process of AISI 316L stainless steel welded joint: microstructural evolution, phase equilibrium, mechanical properties and fracture mode. Journal of Materials Research and Technology, 15, 199–212. https://doi.org/10.1016/j.jmrt.2021.07.154

Sabzi, M., Mousavi Anijdan, S. H., Chalandar, A. R. B., Park, N., Jafarian, H. R., & Eivani, A. R. (2022). An experimental investigation on the effect of gas tungsten arc welding current modes upon the microstructure, mechanical, and fractography properties of welded joints of two grades of AISI 316L and AISI310S alloy metal sheets. Materials Science and Engineering A, 840(February), 142877. https://doi.org/10.1016/j.msea.2022.142877

Sabzi, M., Mousavi Anijdan, S. H., Eivani, A. R., Park, N., & Jafarian, H. R. (2021). The effect of pulse current changes in PCGTAW on microstructural evolution, drastic improvement in mechanical properties, and fracture mode of dissimilar welded joint of AISI 316L-AISI 310S stainless steels. Materials Science and Engineering A, 823(July), 141700. https://doi.org/10.1016/j.msea.2021.141700

Sabzi, Masoud, & Dezfuli, S. M. (2018a). Drastic improvement in mechanical properties and weldability of 316L stainless steel weld joints by using electromagnetic vibration during GTAW process. Journal of Manufacturing Processes, 33(February), 74–85. https://doi.org/10.1016/j.jmapro.2018.05.002

Sabzi, Masoud, & Dezfuli, S. M. (2018b). Post weld heat treatment of hypereutectoid hadfield steel: Characterization and control of microstructure, phase equilibrium, mechanical properties and fracture mode of welding joint. Journal of Manufacturing Processes, 34(June), 313–328. https://doi.org/10.1016/j.jmapro.2018.06.009

Saha, D., & Pal, S. (2021). Study on the microstructural variation and fatigue performance of microplasma arc welded thin 316L sheet. Proceedings of the Institution of Mechanical Engineers, Part L: Journal of Materials: Design and Applications. https://doi.org/10.1177/14644207211062067

Sahu, A. K., & Bag, S. (2020). Probe Pulse Conditions and Solidification Parameters for the Dissimilar Welding of Inconel 718 and AISI 316L Stainless Steel. Metallurgical and Materials Transactions A: Physical Metallurgy and Materials Science, 51(5), 2192–2208. https://doi.org/10.1007/s11661-020-05705-4

Sahu, A. K., & Bag, S. (2021). Design of a double aging treatment for the improvement of mechanical and microstructural properties of pulse micro-plasma arc welded alloy 718. Journal of Materials Science, 56(23), 13400–13415. https://doi.org/10.1007/s10853-021-06121-8

Sakthivel, T., Vasudevan, M., Laha, K., Parameswaran, P., Chandravathi, K. S., Mathew, M. D., & Bhaduri, A. K. (2011). Comparison of creep rupture behaviour of type 316L(N) austenitic stainless steel joints welded by TIG and activated TIG welding processes. Materials Science and Engineering A, 528(22–23), 6971–6980. https://doi.org/10.1016/j.msea.2011.05.052

Sánchez-Tovar, R., Montañés, M. T., & García-Antón, J. (2011). Effect of the micro-plasma arc welding technique on the microstructure and pitting corrosion of AISI 316L stainless steels in heavy LiBr brines. Corrosion Science, 53(8), 2598–2610. https://doi.org/10.1016/j.corsci.2011.04.019

Sánchez-Tovar, R., Montañés, M. T., & García-Antón, J. (2013). Effects of microplasma arc AISI 316L welds on the corrosion behaviour of pipelines in LiBr cooling systems. Corrosion Science, 73, 365–374. https://doi.org/10.1016/j.corsci.2013.04.025

Sasikumar, R., Kannan, A. R., Kumar, S. M., Pramod, R., Kumar, N. P., Shanmugam, N. S., Palguna, Y., & Sivankalai, S. (2022). Wire arc additive manufacturing of functionally graded material with SS 316L and IN625: Microstructural and mechanical perspectives. CIRP Journal of Manufacturing Science and Technology, 38, 230–242. https://doi.org/10.1016/j.cirpj.2022.05.005

Sayyar, N., Shamanian, M., Niroumand, B., Kangazian, J., & Szpunar, J. A. (2020). EBSD observations of microstructural features and mechanical assessment of INCOLOY 825 alloy/AISI 321 stainless steel dissimilar welds. Journal of Manufacturing Processes, 60(July), 86–95. https://doi.org/10.1016/j.jmapro.2020.10.042

Shakil, M., Ahmad, M., Tariq, N. H., Hasan, B. A., Akhter, J. I., Ahmed, E., Mehmood, M., Choudhry, M. A., & Iqbal, M. (2014). Microstructure and hardness studies of electron beam welded Inconel 625 and stainless steel 304L. Vacuum, 110, 121–126. https://doi.org/10.1016/j.vacuum.2014.08.016

Shankar, V., Bhanu Sankara Rao, K., & Mannan, S. L. (2001). Microstructure and mechanical properties of Inconel 625 superalloy. Journal of Nuclear Materials, 288(2–3), 222–232. https://doi.org/10.1016/S0022-3115(00)00723-6

Shen, F., Wang, H., Liu, Z., Liu, W., Könemann, M., Yuan, G., Wang, G., Münstermann, S., & Lian, J. (2022). Local formability of medium-Mn steel. Journal of Materials Processing Technology, 299(August 2021). https://doi.org/10.1016/j.jmatprotec.2021.117368

Shojaei Zoeram, A., Rahmani, A., & Akbari Mousavi, S. A. A. (2017). Microstructure and properties analysis of laser-welded Ni–Ti and 316l sheets using copper interlayer. Journal of Manufacturing Processes, 26, 355–363. https://doi.org/10.1016/j.jmapro.2017.02.005

Sindo Kou. (2003). Welding Metallurgy (Second). John Wiley & Sons, Inc. All.

Sivakumar, J., Vasudevan, M., & Korra, N. N. (2021). Effect of activated flux tungsten inert gas (A-TIG) welding on the mechanical properties and the metallurgical and corrosion assessment of Inconel 625. Welding in the World, 65(6), 1061–1077. https://doi.org/10.1007/s40194-020-01061-4

Soares, A. G., Martins, R. F., Mateus, A. R., & da Silva, P. P. (2019). Design enhancements to a gas turbine's exhaust system used for naval propulsion. Engineering Failure Analysis, 102(April), 20–34. https://doi.org/10.1016/j.engfailanal.2019.04.020

Sourmail, T. (2001). Precipitation in creep resistant austenitic stainless steels. Materials Science and Technology, 17(1), 1–14. https://doi.org/10.1179/026708301101508972

Sriba, A., Vogt, J. B., & Amara, S. E. (2018). Microstructure, Micro-hardness and Impact Toughness of Welded Austenitic Stainless Steel 316L. Transactions of the Indian Institute of Metals, 71(9), 2303–2314. https://doi.org/10.1007/s12666-018-1362-4

Su, Y., Dai, Z., Yang, T., Wang, Y., Liang, X., & Wu, X. (2021). Study on hot deformation behavior and strengthening mechanism of Inconel 625 deposited metal at high temperature. Journal of Materials Science, 56(29), 16745–16761. https://doi.org/10.1007/s10853-021-06357-4

Subramanian, C., Roy, H., Kumar, A., Mondal, A., Ray, S., De, S. K., Ghosh, D., & Saha, A. (2021). Failure cause analysis of an expansion bellow of integrated turbine unit. International Journal of Pressure Vessels and Piping, 191(February), 104360. https://doi.org/10.1016/j.ijpvp.2021.104360

Sukumaran, A., Gupta, R. K., & Anil Kumar, V. (2017). Effect of Heat Treatment Parameters on the Microstructure and Properties of Inconel-625 Superalloy. Journal of Materials Engineering and Performance, 26(7), 3048–3057. https://doi.org/10.1007/s11665-017-2774-8

Tlili, I., Baleanu, D., Mohammad Sajadi, S., Ghaemi, F., & Fagiry, M. A. (2022). Numerical and experimental analysis of temperature distribution and melt flow in fiber laser welding of Inconel 625. International Journal of Advanced Manufacturing Technology, 121(1–2), 765–784. https://doi.org/10.1007/s00170-022-09329-3

Tomashchuk, I., Sallamand, P., Andrzejewski, H., Grevey, D., I.TomashchukP.SallamandH.AndrzejewskiD.Greve, Tomashchuk, I., Sallamand, P., Andrzejewski, H., & Grevey, D. (2011). The formation of intermetallics in dissimilar Ti6Al4V/copper/AISI 316 L electron beam and Nd: YAG laser joints. Intermetallics, 19(10), 1466–1473. https://doi.org/10.1016/j.intermet.2011.05.016

Tseng, K. H., Hsieh, S. T., & Tseng, C. C. (2003). Effect of process parameters of micro-plasma arc welding on morphology and quality in stainless steel edge joint welds. Science and Technology of Welding and Joining, 8(6), 423–430. https://doi.org/10.1179/136217103225009107

Tseng, K., & Hsu, C. (2011). Performance of activated TIG process in austenitic stainless steel welds. Journal of Materials Processing Tech., 211(3), 503–512. https://doi.org/10.1016/j.jmatprotec.2010.11.003

Wang, F. X., He, J. P., Fang, J., Xiang, F., & Ren, L. (2012). Study of Titanium foil welding using micro-plasma arc welding. Advanced Materials Research, 538–541, 1469–1472. https://doi.org/10.4028/www.scientific.net/AMR.538-541.1469

Wang, F., Zhuge, F., Zhang, H., & Ding, B. (2003). Effect of high content nano-thoria addition on the properties of tungsten electrode. 38, 629–636. https://doi.org/10.1016/S0025-5408(03)00005-9

Wang, K., Liu, G., Zhao, J., Wang, J., & Yuan, S. (2016). Formability and microstructure evolution for hot gas forming of laser-welded TA15 titanium alloy tubes. Materials and Design, 91, 269–277. https://doi.org/10.1016/j.matdes.2015.11.100

Wang, X., Liu, Z., Li, J., Chen, L., & Li, B. (2022). Effect of heat treatment on microstructure, corrosion resistance, and interfacial characteristics of Inconel 625 laser cladding layer. Optik, 270(August), 169930. https://doi.org/10.1016/j.ijleo.2022.169930

Wang, Z., Zhang, Z., Lang, Q., Song, G., & Liu, L. (2023). Microstructure evolution and deformation behavior of TIG welded 7075-T6 aluminum alloy followed by partial hot rolling. Journal of Manufacturing Processes, 94(April), 524–538. https://doi.org/10.1016/j.jmapro.2023.04.006

Wei, C., Zhang, J., Yang, S., Sun, L., Tao, W., Wu, F., & Xia, W. (2015). Improving formability of laser welded automotive dual phase steels with local cooling. Science and Technology of Welding and Joining, 20(2), 145–154. https://doi.org/10.1179/1362171814Y.0000000263

Wu, Y., Guo, Y., Zhang, W., & Li, L. (2022). Microstructure evolution and dynamic mechanical behavior of laser welded dissimilar joint between QP1180 and TRIP780. Journal of Materials Research and Technology, 16, 977–987. https://doi.org/10.1016/j.jmrt.2021.12.076

Xia, MS and Kuntz, ML and Tian, ZL and Zhou, Y. (2008). Failure study on laser welds of dual phase steel in formability testing. Science and Technology of Welding and Joining, 13(4), 378–387. https://doi.org/10.1179/174329308X299977

Xia, M., Sreenivasan, N., Lawson, S., Zhou, Y., & Tian, Z. (2007). A comparative study of formability of diode laser welds in DP980 and HSLA steels. Journal of Engineering Materials and Technology, 129(3), 446–452. https://doi.org/10.1115/1.2744417

Xing, X., Di, X., & Wang, B. (2014). The effect of post-weld heat treatment temperature on the microstructure of Inconel 625 deposited metal. Journal of Alloys and Compounds, 593, 110–116. https://doi.org/10.1016/j.jallcom.2013.12.224

Xu, F., Lv, Y., Liu, Y., Shu, F., He, P., & Xu, B. (2013). Microstructural Evolution and Mechanical Properties of Inconel 625 Alloy during Pulsed Plasma Arc Deposition Process. Journal of Materials Science and Technology, 29(5), 480–488. https://doi.org/10.1016/j.jmst.2013.02.010

Xu, L. Y., Jing, H. Y., & Han, Y. D. (2018). Effect of welding on the corrosion behavior of X65/Inconel 625 in simulated solution. Welding in the World, 62(2), 363–375. https://doi.org/10.1007/s40194-018-0549-y

Yang, F., Dong, L., Hu, X., Zhou, X., Xie, Z., & Fang, F. (2020). Effect of solution treatment temperature upon the microstructure and mechanical properties of hot rolled Inconel 625 alloy. Journal of Materials Science, 55(13), 5613–5626. https://doi.org/10.1007/s10853-020-04375-2

Yao, Y., Chen, A., Wang, F., Jiang, H., Li, G., & Cui, J. (2023). Mechanical properties and joining mechanisms of magnetic pulse welding joints of additively manufactured 316L and conventional AA5052 aluminum alloy. Journal of Materials Research and Technology, 26, 6146–6161. https://doi.org/10.1016/j.jmrt.2023.09.008

Yu, X., Xue, J., Shen, Q., Zheng, Z., Ou, N., & Wu, W. (2023). Dual-Wire Plasma Arc Additively Manufactured SS 316L-Inconel 625 Functionally Graded Material: Microstructure Evolution and Mechanical Properties. Journal of Materials Engineering and Performance, 32(3), 1412–1422. https://doi.org/10.1007/s11665-022-07158-9

Zhang, W. (2005). Design of a vision sensor for monitoring microplasma arc welding of metal bellows. Advanced Sensor Systems and Applications II, 5634(February 2005), 782. https://doi.org/10.1117/12.570653

Zhang, Z., Chu, S., Xiong, J., Jiang, C., & Li, X. (2022). The effect of solid solution temperature on the precipitation phase and properties of plasma arc welded joints of Inconel625 high temperature alloy. Materials Research Express, 9(12). https://doi.org/10.1088/2053-1591/aca244

Publication from the thesis work

Patent

1. S. K. Biswal, **V. Haldar**, & S. Pal, "Portable forming setup", (Design Application No. 350154-001). Controller General of Patents, Designs and Trademarks, Government of India. (*Design patent*).

International journals

1. **Haldar V**, Biswal SK, Pal, S (2022) Formability study of micro-plasma arc-welded AISI 316L stainless steel thin sheet joint. J Brazilian Soc Mech Sci Eng. 44:1–16. https://doi.org/10.1007/s40430-022-03871-7
2. **Haldar V**, Pal, S (2023) Influence of Fusion Zone Metallurgy on the Mechanical Behavior of Ni-Based Superalloy and Austenitic Stainless Steel Dissimilar Joint. J Mater Eng. Perform. 33:5735–5753. https://doi.org/10.1007/s11665-023-08335-0
3. **Haldar**, **V**., & Pal, S (2024) A metallurgical study of micro plasma arc welded joint of austenitic stainless-steel blank Archives of Metallurgy and Materials. 69: 1071-1078. 0.24425/amm.2024.150927
4. **Haldar**, **V**., & Pal, S Characterization of Mechanical Behavior in Solution-Treated Micro Plasma Arc Welded Blanks of Inconel 625. Metals and Materials International. 10.1007/s12540-024-01850-2

Book chapter

1. **Haldar**, **V**., & Pal, S. (2022). Effect of the Rolling Direction on the Mechanical and Microstructural Properties of AISI 316L Stainless Steel Welded Joint. In Recent Advances in Manufacturing Processes and Systems: Select Proceedings of RAM 2021 (pp. 381-389). Singapore: Springer Nature Singapore. https://doi.org/10.1007/978-981-16-7787-8_29

Conferences

1. **Haldar**, **V**., & Pal, S. Recent Advances in Manufacturing Processes and Systems (RAM 2021), organized by Department of Mechanical Engineering, S.V. National Institute of Technology, Gujrat held in between 10-12th June.
2. **Haldar**, **V**., & Pal, S. International Conference on Advances in Mechanical Engineering & Material Sciences, organized by the School of Mechanical Engineering, VIT-AP University, Amaravati held between 20th -22nd April 2023.